Sorbjan, Z. (2004) *The Large-Eddy Simulations of the Atmospheric Boundary Layer*. Chapter 5B of *AIR QUALITY MODELING - Theories, Methodologies, Computational Techniques, and Available Databases and Software. Vol. II – Advanced Topics*. (P. Zannetti, Editor). Published by The EnviroComp Institute (www.envirocomp.org) and the Air & Waste Management Association (www.awma.org).

Chapter 5B

Large-Eddy Simulations of the Atmospheric Boundary Layer

Zbigniew Sorbjan

Department of Physics, Marquette University, Milwaukee, WI 53201, USA,
Institute of Meteorology and Water Management, 01-673 Warsaw, Poland,
sorbjanz@mu.edu

Abstract: In this Chapter, the large-eddy simulation technique is described. The presented material consists of two parts. In the first one, technical issues, including filtering, subgrid modeling, and numerical integration are discussed. In the second part, simulations of typical prototypes of the atmospheric boundary layer are presented, including convective, neutral, stable, and cloud-topped cases.

Key Words: atmospheric boundary layer, cloud-free boundary layer, cloud-topped boundary layer, turbulence, mixing, convection, mixed layers, large-eddy simulations.

1 Introduction

The atmospheric boundary layer (ABL) is an inherently complex and heterogeneous system, which is under permanent transition, enforced by a variety of internal and external factors. Some of its fascinating signatures are revealed on satellite images, due to intricate cloud patterns, organized in a coherent fashion (Figure 1).

An understanding of the ABL, its structure and dynamics, is essential for weather prediction and environmental studies. During the last four decades, the fundamental knowledge of boundary layer turbulence has been achieved as a result of extensive experimental effort [e.g., Augstein et al. (1973), Holland and Rasmusson (1973), Brost and Wyngaard (1984 a,b), Brümmer et al. (1985),

Albrecht et al. (1988), Webster and Lucas (1992), Albrecht et al. (1995), LeMone and Grossman (1999), Curry at al. (2000), Kristovich et al. (2000), White et al. (2000), LeMone, et al. (2002), Paulos, et al. (2002)]. The experimental work has been supplemented by numerical research, especially "large-eddy simulations" (LES).

In large-eddy simulations most of the turbulence (i.e., large eddies) is directly resolved from the Navier-Stokes equations, and only the small-scale (subgrid) turbulence is modeled (e.g., Lilly, 1967, Nieuwstadt 1990; Mason 1994). Note that we differentiate between two commonly used terms: "modeling" and "simulating". "Modeling" is understood here as approximating, while "simulating" is considered as more realistic and reliable representation of nature, faithful to the essential physics of the flow.

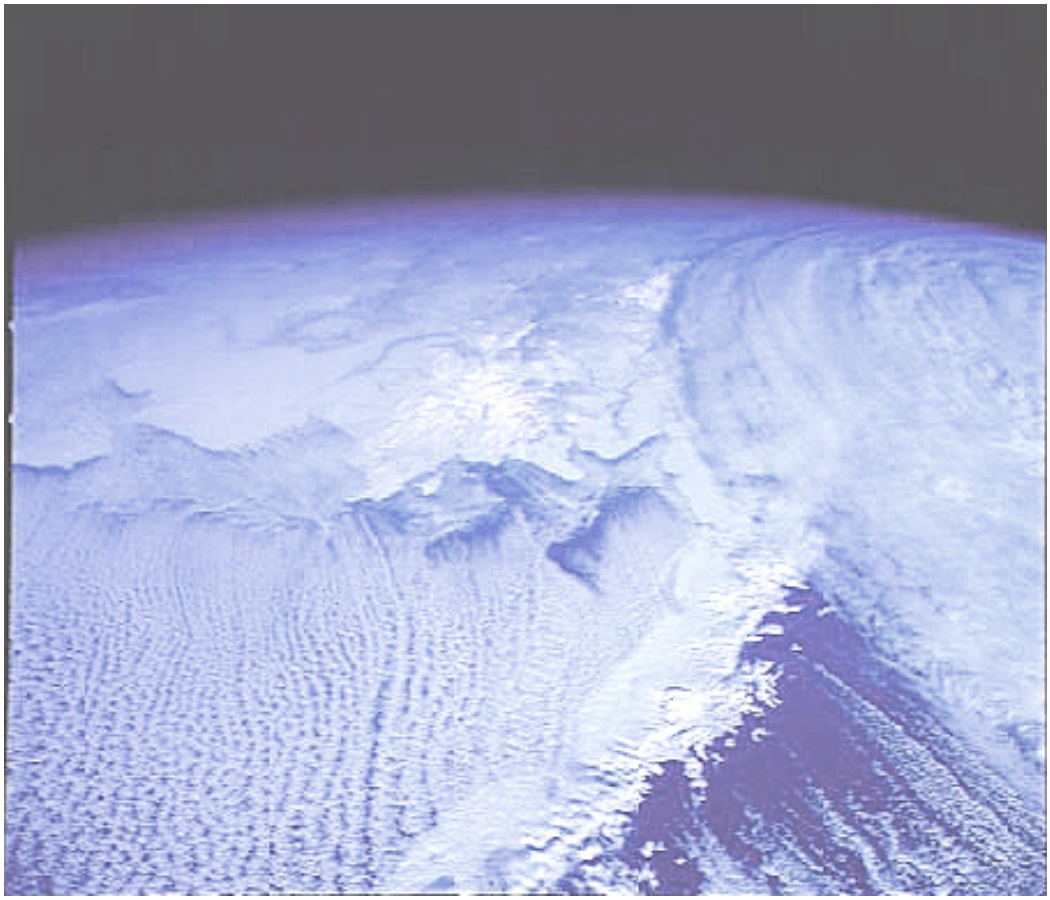

Figure 1. Rolls and cells marked by cumuli clouds during an outbreak of cooler air over a warmer ocean (NASA).

The LES technique was developed by Deardorff (1970, 1972; 1973; 1974 a, b). The early LES focused on the cloud-free, convective boundary layers [e.g., Schemm and Lipps (1976), Moeng (1984, 1986), Schmidt and Schumann (1989), Mason (1989)]. Effects of shear were considered later by e.g., Mason (1992a),

Moeng and Sullivan (1994), Glendening (1996), Kim, et al. (2003), Sorbjan (2004 a, c).

The important role of clouds in the dynamics of the atmospheric boundary layer has generated interest in large-eddy simulations of cloud-topped mixed layers. Especially, the boundary layer containing stratus and stratocumulus clouds has obtained extensive consideration of e.g. Deardorff (1976, 1980), Sommeria (1976), Moeng (1986), Schumann and Moeng (1991), Moeng and Schumann (1991), Kogan et al. (1995), Moeng et al. (1996), Lewellen and Lewellen (1996), Shen and Moeng (1993), Khairoutdinov and Kogan (1999), Jian and Cotton (2000), Stevens et al. (1998, 1999, 2001), Siebesma et al. (2003), Neggers et al. (2002).

Large-eddy simulations of the ABL with cumulus clouds have also been performed. The pioneering study was done by Sommeria (1976). It was continued by Cuijpers and Duynkerke (1993), Siebesma et al, (2002), and Brown et al (2002).

Thereafter, there were also attempts to employ the LES to simulate the stably stratified flows in the ABL. The effort obtained much less attention due to the difficulties in resolving small-scale turbulence. The pioneering simulation of the stably stratified boundary layer was performed by Mason and Derbyshire (1990). The simulation was later repeated with various subgrid models by Brown et al. (1994), Andren (1996), Kosovic and Curry (1999), Cedeval and Street (1999), Saiki et al (1999), Beare et al. (2004), Beare and MacVean (2004).

Other ABL simulations included diurnal transitions. The first LES study of the decaying atmospheric convective mixed layer was performed by Nieuwstadt and Brost (1986). The authors analyzed a case of the shearless, clear mixed layer, in which turbulence decayed as a result of a sudden shut-off of the upward surface heat flux. The study of Nieuwstadt and Brost was followed by Sorbjan (1997) who considered a gradual change of the heat flux with time, in response to the decreasing sun’s elevation. Acevedo and Fitzjarrald (1999, 2001) undertook a LES study in order to understand the effects of moistening close to the earth's surface during the early evening transition.

A few LES studies were conducted on advective transitions. Chlond and Müller (1997) considered horizontal roll vortices in the ABL by using a "very large eddy" approach applied to a LES-type model with periodic boundary conditions. Within their Lagrangian approach, a LES model "traveled" with the geostrophic wind speed along the wind direction. Another approach was applied by Mayor et al. (2002) who performed a LES study of a cold-air outbreak over Lake Michigan. Schröter and Raasch (2002) performed a high-resolution study of cell broadening during cold air outbreaks.

Diffusion in the clear-sky convective boundary layer was significantly advanced by the numerical simulations and laboratory experiments of Willis and Deardorff (1976, 1978, 1981). Their investigations demonstrated that for elevated sources, the average plume centerline, defined as the mean maximum concentration, descended within a short distance from the source, until it reached the ground. In contrast, the average centerline from near surface releases ascended after a short downwind distance. LES of diffusion in the stratocumulus-topped ABL was performed by Sorbjan and Uliasz (1999).

The purpose of this Chapter is to review the theoretical basis of large-eddy simulations, and to present the most typical results. The discussed topics are addressed to air-pollution engineers, who intend to improve their understanding of complex processes controlling diffusion within the atmospheric boundary layer. The Chapter is organized as follows. The LES approach is described in Section 2. A short overview of the governing equations is presented in Section 2.1, followed by brief information on filtering, subgrid modeling, and numerical integration in Sections 2.2 and 2.3. Large-eddy simulations of typical boundary layers regimes are presented in Section 3. The considered cases include the convective, neutral, stable, and cloudy conditions.

2 Theoretical Background

2.1 Basic Equations

The most general set of equations which governs the motion of a compressible, viscous fluid consists of:

- the momentum equations: $$\frac{du_i}{dt} = -\frac{1}{\rho_o}\frac{\partial p}{\partial x_i} - 2\,\varepsilon_{ijk}\,\Omega_j u_k - g\,\delta_{i3} - \frac{\partial \sigma_{ij}}{\partial x_j} \quad (1)$$

- the continuity equation: $$\frac{d\rho}{dt} = -\rho\,\frac{\partial u_j}{\partial x_j} \quad (2)$$

- the first law of thermodynamics: $$C_p\,\frac{dT}{dt} - \frac{1}{\rho}\,\frac{dp}{dt} = S \quad (3)$$

- and the ideal gas law: $$p = \rho\, R_d\, T \quad (4)$$

where $i, j, k = 1, 2, 3$ (note that repeated indices indicate summation), p, ρ, and T are the static pressure, air density, and the absolute temperature respectively, u_j is the j-component of the velocity, R_d is the gas constant, C_p is the specific heat at constant pressure, g is the gravity acceleration. Moreover, $d/dt = \partial/\partial t + u_j\,\partial/\partial x_j$ *is* the total derivative, σ_{ij} is the anisotropic part of the viscous stress tensor, $\sigma_{ij} = 2\nu$

$S_{ij} + \beta S_{kk} \delta_{ij}$, where ν is the molecular viscosity, δ_{ij} is the Kronecker delta, $S_{ij} = \frac{1}{2}(\partial u_i / \partial x_j + \partial u_j / \partial x_i)$ is the rate of strain. Since $\sigma_{kk} = 0$, the coefficient β has to be defined as $\beta = -2/3\ \nu$. S is the heating/cooling flux, involving radiation, phase changes, and diffusion. The diffusion part of S has the form $\partial F_i / \partial x_i$, where the molecular heat flux is described as $F_i = -D\ \partial T / \partial x_i$, and D is the molecular diffusivity. The term $2\varepsilon_{ijk}\ \Omega_j\ u_k$ is the Coriolis acceleration, Ω_j is the j-component of the earth's angular velocity, ε_{ijk} is the component of the unit tensor, equal to 1 for even permutations of the indices *(i, j, k)*, -1 for odd permutations, and 0 otherwise. Note that in the coordinate system, in which the x-axis is pointing east, the y-axis is pointing north, and the z-axis is pointing vertically, the components of the earth's angular velocity Ω are defined as $\Omega_1 = 0,\ \Omega_2 = \Omega \cos \phi,\ \Omega_3 = \Omega \sin \phi$, where ϕ is the latitude.

The above equations have been developed from the 17th to the 19th centuries by a number of scolars. Among them was: Isaac Newton (1687), who discovered the laws of dynamics, Robert Boyle (1662), Jacques Charles (1787), Joseph Gay-Lussac (1802), Amerigo Avogadro (1813), who contrived the ideal gas equation, Leonhard Euler (1755), who invented the non-viscous flow equations and the continuity equation, Claude-Louis Navier (1827) and Georg Stokes (1845), who developed the viscous flow equations, and Rudolf Clausius (1851), who formulated the first law of thermodynamics.

The set (1)-(4) is often simplified due to the fact that the atmospheric boundary layer is relatively shallow with respect to the depth of the entire atmosphere. Consequently, the density variation with height can be neglected. Following the usual practice in this case, we will consider the atmosphere to be in a state slightly removed from an adiabatic atmosphere at rest. We consider an expansion of the governing parameters into basic state values (denoted by the index "o") and perturbations (denoted by the index "):

$$
\begin{aligned}
p &= p_o + p'' \\
T &= T_o + T'' \\
\rho &= \rho_o + \rho'' \\
u_j &= u_{jo} + u_j'' \qquad (i = 1, 2, 3)
\end{aligned}
\tag{5}
$$

where:

the basic state pressure: $p_o = \rho_o R_d T_o$

the basic state temperature: $dT_o / dz = -\Gamma_a = -10$ K/km

the basic state density:

$$\frac{1}{\rho_o}\frac{\partial p_o}{\partial x_i} = -2\,\varepsilon_{ijk}\,\Omega_j\,G_k \quad (i = 1, 2)$$

$$\frac{1}{\rho_o}\frac{\partial p_o}{\partial x_3} = -g \tag{6}$$

the basic velocity:

$$u_{jo} = 0$$

and G_k are the components of the geostrophic wind. The geostrophic wind is allowed to be a function of height (baroclinicity): $G_k = G_{ko} + T_k z$, where T_k is the thermal wind, and $G_{ko} = G_k\,(z = 0)$.

For the gas law (4) we will obtain:

$$p'' = p - p_o = R_d\,(\rho\,T - \rho_o\,T_o) = R_d\,(\rho_o\,T'' + \rho''\,T_o + \rho''\,T'') \tag{7}$$

Note that (7) can be rewritten as:

$$p''/p_o = T''/T_o + \rho''/\rho_o + \rho''\,T_o''/(\rho_o\,T_o) \tag{8}$$

which can be simplified as:

$$p''/p_o = T''/T_o + \rho''/\rho_o \tag{9}$$

Note that the order of p'' in (9) can be evaluated as $\rho_o u_j''^2$ (which is equivalent of assuming in the momentum equation that the flow is caused by a pressure gradient: $\partial u_j''^2/\partial x_j = 1/\rho_o\,\partial p''/\partial x_j$). Consequently:

$$p''/p_o \sim O\,(u_j''^2/R_d\,T_o) \sim O\,(\gamma\,M^2) \tag{10}$$

where $M = u_j''/c_s$ is the Mach number, $c_s = (\gamma\,R_d T_o)^{0.5}$ is the adiabatic speed of sound in ideal gas, $\gamma = C_p/C_v$ is equal to 1.4 for dry air, and C_p, C_v are the specific heat coefficients at constant pressure and volume. Assuming that $M << 1$, we can neglect the effects of motion-induced pressure changes in (9), which yields:

$$T''/T_o + \rho''/\rho_o = 0 \tag{11}$$

From the definition of the potential temperature $\Theta = T\,(1000/p)^{R_d/C_p}$, it follows that

$$\frac{d\Theta}{\Theta} = -\frac{dT}{T} - \frac{R_d}{C_p}\frac{dp}{p} \tag{12}$$

and also

$$\frac{\Theta''}{\Theta_o} = \frac{T''}{T_o} - \frac{R_d}{C_p}\frac{p''}{p_o} \tag{13}$$

Using (11) and (13), we arrive at:

$$\frac{\Theta''}{\Theta_o} = -\frac{\rho''}{\rho_o} \tag{14}$$

Based on (12) Equation (3) can be written in terms of the potential temperature

$$\frac{T}{\Theta}\frac{d\Theta}{dt} = S \tag{15}$$

Near the earth's surface *(T/*$\Theta \sim 1$), so

$$\frac{d\Theta}{dt} = S \tag{16}$$

From Equations (2) and (3), we will get in the adiabatic case (*S = 0*):

$$\frac{\partial u_j}{\partial x_j} = \frac{1}{\rho}\frac{d\rho}{dt} =$$

$$= \frac{1}{p}\frac{dp}{dt} - \frac{1}{T}\frac{dT}{dt} = \frac{C_v}{C_p}\frac{d\ln p}{dt} \tag{17}$$

Based on (6):

$$\frac{\partial \ln p}{\partial t} \sim u_o''\frac{\partial \ln p}{\partial x} \sim \frac{u_o''}{\rho R_d T_o}\frac{\rho u_o''^2}{L_o} \sim \frac{u_o''^3}{R_d T_o L_o}$$

$$\frac{\partial \ln p}{\partial x_3} \sim \frac{g}{R_d T_o} = \frac{1}{H} \tag{18}$$

where $H = R_d T_o/g \sim 10$ km, is the height of the isothermal atmosphere, L_o is the horizontal length scale, u_o'' is the scale of the horizontal velocity perturbations.

Based on (17) – (18) we will obtain

$$\frac{\partial u_j}{\partial x_j} \sim \frac{u_o''^3}{c_s^3 L_o} + \frac{C_v}{C_p}\frac{w_o''}{H} \tag{19}$$

where w''_o is the scale of the vertical velocity perturbations. Assuming that all terms of the velocity divergence have a similar magnitude: $u''_o/L_o \sim w''_o/D$, where D is the scale of convective motion, and $u''^2_o/c_s^2 << 1$, $D/H << 1$, yields:

$$\frac{\partial u_j}{\partial x_j} = \frac{u_o''}{L_o}\left[\frac{u_o''^2}{c_s^2} + \frac{C_v}{C_p}\frac{D}{H}\right] \sim 0 \tag{20}$$

The result is called the "incompressible approximation".

In the momentum equations, the pressure and gravity terms can be expressed as:

$$-\frac{1}{\rho}\frac{\partial p}{\partial x_i} - g\,\delta_{ij} = -\frac{1}{\rho_o + \rho''}\frac{\partial (p_o + p'')}{\partial x_i} - g\,\delta_{ij} \tag{21}$$

Since

$$\frac{1}{\rho_o + \rho''} = \frac{1}{\rho_o}\frac{1}{[1 + \frac{\rho''}{\rho_o}]} = \frac{1}{\rho_o}[1 - \frac{\rho''}{\rho_o} + ...] \approx \frac{1}{\rho_o}[1 - \frac{\rho''}{\rho_o}] \tag{22}$$

then, based on (6) we have

$$\frac{1}{\rho}\frac{\partial p}{\partial x_i} = -2\,\varepsilon_{ijk}\,\Omega_j\,G_k + \frac{1}{\rho}\frac{\partial p''}{\partial x_i} \qquad (\text{for } i = 1, 2) \tag{23}$$

$$\frac{1}{\rho}\frac{\partial p}{\partial x_3} - g = \tag{24}$$

$$= \frac{1}{\rho_o}[1 - \frac{\rho''}{\rho_o}][\frac{\partial p_o}{\partial x_3} + \frac{\partial p''}{\partial x_3}] - g = \frac{1}{\rho_o}\frac{\partial p''}{\partial x_3} - \frac{\rho''}{\rho_o^2}\frac{\partial p_o}{\partial x_3} =$$

$$= \frac{1}{\rho_o}\frac{\partial p''}{\partial x_3} - \frac{[\Theta - \Theta_o]}{\Theta_o}g$$

where Θ_o is the reference temperature. The result is called the "Boussinesq approximation". It neglects density variations in fluid except when they are coupled with the gravity acceleration.

Applying all of the above-described simplification, we will rewrite (1)-(4) in the following form:

$$\frac{du_i}{dt} = -\frac{1}{\rho_o}\frac{\partial p''}{\partial x_i} - 2\,\varepsilon_{ijk}\,\Omega_j(u_k - G_k) + \frac{g}{\Theta_o}(\Theta - \Theta_o)\,\delta_{i3} - \frac{\partial \sigma_{ij}}{\partial x_j}$$

$$\frac{\partial u_j}{\partial x_j} = 0 \qquad (25)$$

$$\frac{d\Theta}{dt} = S$$

The above system constitutes five equations with five unknowns: u_1, u_2, u_3, Θ and p''. The system can only be solved numerically (e.g., by a finite difference method). The resulting approach is called the "direct numerical simulation" (DNS). Its applications are limited to relatively small domain problems, as will be explained below.

2.2 Filtering

Basic flows in the atmospheric boundary layer take on the form of large eddies. Their is size is proportional to the flow geometry, and characterized by scale L (e.g., the height of the ABL). Large eddies fall apart into smaller and smaller ones, due to flow instabilities. This cascade continues until the smallest flow scales are reached. There, the motion is damped out by viscosity and dissipated into heat.

The smallest scale of motion is described by "the Kolmogorov microscale" η. The dimensional analysis predicts that $\eta = \nu^{3/4}/\varepsilon^{1/4}$, where ε is the dissipation rate, and ν the kinematic viscosity. For $\nu = 10^{-5}$ m^2/s, $\varepsilon = 10^{-3}$ m^2/s^3, we obtain that $\eta = 10^{-3}$ m = 1 mm. The ratio of both scales η and L is $L/\eta = Re^{3/4}$, where $Re = UL/\nu$ is the Reynolds number, and U is a characteristic velocity scale.

The number of grid points needed to numerically resolve all turbulent motions in 3-dimensional space should be at least

$$N \sim (L/\eta)^3 = Re^{9/4} \qquad (26)$$

For $U = 10$ m/s, $L = 1000$ m, $\nu = 10^{-5}$ m^2/s, $Re = 10^9$. Consequently, the required number of grid points in the atmospheric boundary layer is $N \sim 10^{20}$. This number is beyond the capacity of modern computers. Thus, DNS is restricted to flows that are characterized by more modest Reynolds numbers, of the order of 10^2-10^3 (which is not very useful in solving the ABL problems).

To resolve this numerical resolution difficulty, the approach called “large-eddy simulation” (LES) was invented. The philosophy behind this technique is that the largest eddies define the flow, and are primarily responsible for all transport processes, such as the exchange of momentum, heat, or contaminants. Large eddies contain most of the energy, do most of the transporting of conserved properties, and vary from flow to flow. The smaller eddies are believed to be more universal (self-similar), less dependent on boundary conditions, and consequently easier to model. Therefore, LES is designed to directly resolve (simulate) the larger scales of motion, while approximating (modeling) the smaller ones.

It is important to precisely define the quantities to be computed by LES. This is done by filtering or removing of smallest-scale components from the governing equations (Leonard, 1974). The filtered velocity is defined by:

$$\overline{u}_i(x) = \int_{-\infty}^{\infty} G(x, X)\, u_i(X)\, dX \tag{27}$$

where one-dimensional notation is used for convenience (the generalization to three dimensions is straight-forward), *G(x, X)* is the filter kernel with a compact support (i.e., G is large only when *x* and *X* are not far apart).

Filter functions, which have been applied in LES, include "box", Gaussian, and "cut-off" kernels. The box kernels imply simply an average over a rectangular region. It is a natural choice when finite difference, or finite volume methods are used to solve the filtered equations:

$$\overline{u}_i(x) = \frac{1}{2\Delta} \int_{x-\Delta}^{x+\Delta} u_i(X)\, dX \tag{28}$$

Two versions of this filter have been used. In the moving box filter, the average is taken over a region of space surrounding any chosen point. According to this definition, $\overline{u}_i$ is a continuous function of *x*. A filter, which is an average over a grid volume of a finite difference or finite volume mesh, is tied more closely to the numerical method. According to this definition, $\overline{u}_i$ is a piecewise constant function of x.

Gaussian kernels have the advantage of being smooth and infinitely differentiable in both physical and Fourier space. Cut-off kernels are defined in Fourier space. They eliminate all of the Fourier coefficients, which belong to wave numbers above a particular cutoff. It is natural to use them in conjunction with spectral methods.

When the Navier-Stokes equations are filtered, the following set of equations is obtained:

$$\frac{\partial \bar{u}_i}{\partial t} + \frac{d\overline{u_i u_j}}{dx_j} = -\frac{1}{\rho_o}\frac{\partial \overline{p''}}{\partial x_i} - 2\,\varepsilon_{ijk}\;\Omega_j(\bar{u}_k - G_k) + \frac{g}{\Theta_o}(\overline{\Theta} - \Theta_o)\,\delta_{i3} - \frac{\partial \overline{\sigma_{ij}}}{\partial x_j}$$

$$\frac{\partial \bar{u}_j}{\partial x_j} = 0 \tag{29}$$

$$\frac{\partial \overline{\Theta}}{\partial t} + \frac{\partial \overline{u_j \Theta}}{\partial x_j} = \overline{S}$$

Assuming that:

$$\begin{aligned} \tau_{ij} &= \overline{u_i u_j} - \bar{u}_i \bar{u}_j \\ \mathrm{H_j} &= \overline{u_j \Theta} - \bar{u}_j\;\overline{\Theta} \end{aligned} \tag{30}$$

we will obtain:

$$\frac{\partial \bar{u}_i}{\partial t} + \frac{d\bar{u}_i \bar{u}_j}{dx_j} = -\frac{1}{\rho_o}\frac{\partial \overline{p''}}{\partial x_i} - 2\,\varepsilon_{ijk}\;\Omega_j(\bar{u}_k - G_k) - \frac{g}{\Theta_o}(\overline{\Theta} - \Theta_o)\,\delta_{i3} - \frac{\partial \tau_{ij}}{\partial x_j}$$

$$\frac{\partial \bar{u}_j}{\partial x_j} = 0 \tag{31}$$

$$\frac{\partial \overline{\Theta}}{\partial t} + \frac{\partial \bar{u}_j \overline{\Theta}}{\partial x_j} = -\frac{\partial H_j}{\partial x_j} + \overline{S}$$

Above, it was also assumed that the turbulent terms exceeded the molecular ones: $\partial \tau_{ij} / \partial x_i >> \partial \overline{\sigma}_{ij} / \partial x_i$, and $\partial H_i / \partial x_i >> \partial \overline{\vartheta}_i / \partial x_i$.

Note that the same form of equations as (31) would be obtained if the ensemble averaging were employed, instead of the filtering. One important difference between filtering and ensemble averaging is that the ensemble-averaging operator applied twice yields the originally averaged field, $\overline{\bar{u}_i} = \bar{u}_i$. Generally, this expression is not true for filtering operators. The exception is the cutoff filter, for which such equality does hold.

Employing the ensemble averaging, and then decomposing fields into averaged values and fluctuations, e.g., $u_i = \overline{u_i} + u'_i$ and $\Theta = \overline{\Theta} + \theta'$, yields:

$$\tau_{ij} = \overline{u_i u_j} - \overline{u}_i \overline{u}_j = \\ = \overline{(\overline{u}_i + u'_i)(\overline{u}_j + u'_j)} - \overline{(\overline{u}_i + u'_i)}\,\overline{(\overline{u}_j + u'_j)} = \overline{u'_i u'_j}$$

$$H_i = \overline{u_i \Theta} - \overline{u}_i \overline{\Theta} = \\ = \overline{(\overline{u}_i + u'_i)(\overline{\Theta}_j + \theta')} - \overline{(\overline{u}_i + u'_i)}\,\overline{(\overline{\Theta} + \theta')} = \overline{u'_i \theta'} \tag{32}$$

In the context of the large eddy simulation, τ_{ij} is called the "subgrid scale Reynolds stress", and H_j is called the "subgrid scale heat flux". Note that τ_{ij} and H_j are undefined, and need to be modeled. Subgrid scale (SGS) modeling is the most distinctive feature of the large eddy simulation, and is the subject of the next section.

2.3 Subgrid-Scale Modeling

The term "subgrid" refers to the filters closely connected to a grid, which is used to discretisize the basic flow equations. This approach was used in the earliest large eddy simulations. Generally, the connection between the utilized filter and grid is not needed (i.e., the nomenclature is more restrictive than necessary).

As mentioned before, the smallest scale motions are involved in the viscous dissipation of kinetic energy. In a large-eddy simulation this role must be taken over by the subgrid scales. The parameterization of the subgrid terms must comply with this requirement. The simplest choice for such parameterization is (note the similarity to the molecular fluxes):

$$\tau_{ij} = -2k_m (\overline{S}_{ij} - \frac{1}{3}\overline{S}_{kk}\,\delta_{ij}) + \frac{2}{3} E\,\delta_{ij}$$

$$H_j = -k_h \frac{\partial \overline{\Theta}}{\partial x_j} \tag{33}$$

where k_m and k_h are the eddy viscosity and diffusivity, $E = \frac{1}{2}\overline{u_k u_k}$ is the subgrid turbulent kinetic energy, $\overline{S}_{ij}$ is the averaged rate of strain, $\overline{S}_{ij} = \frac{1}{2}(\partial \overline{u}_i / \partial x_j + \partial \overline{u}_j / \partial x_i)$. Equation (33a) is valid in both incompressible ($\overline{S}_{kk} = 0$) and compressible cases.

The system (31) is usually rewritten in the form:

$$\frac{\partial \bar{u}_i}{\partial t} + \frac{d\bar{u}_i \bar{u}_j}{dx_j} = -\frac{\partial \pi}{\partial x_i} - 2\,\varepsilon_{ijk}\,\Omega_j\,(\bar{u}_k - G_k) + \frac{g}{\Theta_o}(\bar{\Theta} - \Theta_o)\,\delta_{i3} - \frac{\partial T_{ij}}{\partial x_j}$$

$$\frac{\partial \bar{u}_j}{\partial x_j} = 0 \qquad (34)$$

$$\frac{\partial \bar{\Theta}}{\partial t} + \frac{\partial \bar{u}_j \bar{\Theta}}{\partial x_j} = -\frac{\partial H_j}{\partial x_j} + \bar{S}$$

where

$$\pi = \frac{\overline{p''}}{\rho_o} + \frac{2}{3}E$$

$$T_{ij} = -2k_m\,(\bar{S}_{ij} - \frac{1}{3}\bar{S}_{kk}\,\delta_{ij}) \qquad (35)$$

$$H_j = -k_h \frac{\partial \bar{\Theta}}{\partial x_j}$$

Note that the turbulent kinetic energy E is included in the pressure term π.

In the above system, the coefficients k_m and k_h remain undefined. In order to evaluate them, we will consider closure models, based on the subgrid turbulent kinetic energy (TKE). The TKE equation can be obtained (from eq. 34a) in the following form (e.g., Sorbjan, 1989):

$$\frac{\partial E}{\partial t} + \frac{\partial \bar{u}_j E}{\partial x_j} = -T_{ij}\,\bar{S}_{ij} + \beta\,H_3 - \frac{\partial \Pi_j}{\partial x_j} - \varepsilon \qquad (36)$$

where $\Pi_j = \overline{u_j(u_k u_k/2 + p)} - \bar{u}_j\,\overline{(u_k u_k/2 + p)}$, $H_3 = \overline{u_3\Theta} - \overline{u_3}\,\overline{\Theta}$, and $\beta = g/T_o$ is the buoyancy parameter. The first two terms on the right-hand side of (36) are: the production term due to shear, and the local buoyancy, respectively. The third term is turbulent transport, and the last term is viscous dissipation ε.

Let us consider the first subgrid model based on (36). As stated before, the dissipation rate is given by definition of the Kolmogorov microscale η:

$$\varepsilon = \frac{\nu^3}{\eta^4} \tag{37}$$

where ν is the kinematic viscosity. By analogy, we shall assume that the net rate of energy transfer out of the filtered flow field (large eddies) is given by

$$\varepsilon_f = \frac{k_m^3}{\Delta_f^4} \tag{38}$$

where Δ_f is the filter width, which also is the length scale of the smallest eddies of the filtered flow field. Assuming in (38) that the dissipation is balanced by the shear production, and $\varepsilon_f = -T_{ij}\ \overline{S}_{ij}$, and $T_{ij} = -2k_m \overline{S}_{ij}$, we have:

$$\varepsilon_f = k_m^3 \Delta_f^{-4} = 2\ k_m \overline{S}_{ij}\ \overline{S}_{ij} \tag{39}$$

The resulting Smagorinsky's model (1963) is of the form:

$$k_m = (C_s \Delta)^2\ (2\ \overline{S}_{ij}\ \overline{S}_{ij})^{1/2} \tag{40}$$

where C_s is the constant of proportionality between Δ_f and the grid size Δ, $\Delta_f = C_s\Delta$, and $\Delta = (\Delta x\ \Delta y\ \Delta z)^{1/3}$.

For Smagorinsky's model, the net rate of the transfer of energy out of the filtered flow ε_f is clearly positive. It has been generally agreed upon that on the average the energy is transferred from large scales to small scales ("forward scatter"). The reverse energy flow ("backscatter") from the small scales to the large ones, associated with random fluctuations of the subgrid-scale stresses, can also occur intermittently. In Smagorinsky-type models, ε is always positive. Therefore these models are absolutely dissipative, i.e., they cannot predict backscatter.

A more complex closure model is based on the assumption that the eddy viscosity and diffusivity coefficients k_m, k_h are functions of the subgrid turbulent kinetic energy E and the length scale Δ:

$$\begin{aligned} k_m &= C_m \Delta \sqrt{E} \\ k_k &= k_m / Pr \end{aligned} \tag{41}$$

where C_m is a universal constant, Pr is the Prandtl number, and E is calculated from the TKE equation (36), in which the dissipation rate and the turbulent transport term can be parameterized as (Deardorff, 1980):

$$\varepsilon = C_\varepsilon \frac{E^{3/2}}{\lambda}$$

$$\Pi_i = -2k_m \frac{\partial E}{\partial x_i} \tag{42}$$

where λ is the mixing length. The functions Pr, λ, as well as parameters C_m, C_ε need to be specified to close the subgrid model.

Both approaches described above (eqs. 40 and 41) have several problems. They do not predict the correct asymptotic behavior near a solid boundary, and do not allow for the SGS energy backscatter to the resolved scales. To overcome these hurdles, other models can be proposed, e.g., non-linear models (e.g., Kosovic, B and J. Curry, 1999), similarity models (e.g., Bardina et al., 1980), dynamic models (e.g., Germano et al, 1992, Lilly, 1992), and mixed models.

2.4 Thermodynamic Formulation

In case, when water vapor is present in the atmosphere, the potential temperature Θ in (34) is replaced by the virtual potential temperature Θ_v, defined as:

$$\Theta_v = \Theta (1 + 0.61\, q_v) \tag{43}$$

where q_v is the water vapor content (i.e., the specific humidity equal to the mass of water vapor in a volume of air, or the mixing ratio, which is the mass of water vapor in a unit mass of air). Note that Θ_v can be interpreted as the temperature of the dry air, which has the same density as the moist air under consideration.

When the phase changes occur, water vapor, as well as liquid water, is present in the air. As a result the virtual potential temperature has the form:

$$\Theta_v = \theta (1 + 0.61\, q_v - q_L) \tag{44}$$

where q_L is the liquid water specific humidity (mass of water in a volume of air). Presence of moisture enhances the buoyancy, while liquid water increases the density of a parcel.

To diagnose the potential temperature Θ from Θ_v in (44), two additional equations are required for q_v and q_L:

$$\frac{\partial \bar{q}_v}{\partial t} + \frac{\partial \bar{u}_j\, \bar{q}_v}{\partial x_j} = -\frac{\partial Q_{vj}}{\partial x_j} - e \tag{45}$$

$$\frac{\partial \bar{q}_L}{\partial t} + \frac{\partial \bar{u}_j \bar{q}_L}{\partial x_j} = -\frac{\partial Q_{Lj}}{\partial x_j} + e$$

where Q_{vj}, Q_{Lj} are the turbulent fluxes, e is the evaporation/condensation rate (we assume that no form of precipitation is present). The evaporation/condensation rates in (45) can be eliminated by adding both equations, which yields:

$$\frac{\partial \bar{q}_T}{\partial t} + \frac{\partial \bar{u}_j \bar{q}_T}{\partial x_j} = -\frac{\partial Q_{Tj}}{\partial x_j} \tag{46}$$

where $q_T = q_v + q_L$ is the total water specific humidity, and Q_{Tj} is the total water content turbulent flux.

When phase changes take place in the atmosphere, it is convenient to consider the liquid water potential temperature θ_L as a prognostic variable. The temperature θ_L can be expressed in a linearized version, defined by Betts (1973):

$$\Theta_L = \Theta - (L/C_p)\, q_L \tag{47}$$

where L is the latent heat of vaporization, C_p is the specific heat of dry air at constant pressure, and Θ is the potential temperature. The liquid water potential temperature and the total water specific humidity are conserved in moist adiabatic process (for no-drizzle case). The temperature θ_L reduces to the dry potential temperature in absence of liquid water. Based on this definition, the equation for the liquid water potential temperature can be obtained from (34c) and (45b) in the form:

$$\frac{\partial \bar{\Theta}_L}{\partial t} + \frac{\partial \bar{u}_j \bar{\Theta}_L}{\partial x_j} = -\frac{\partial H_{Lj}}{\partial x_j} + \bar{S} \tag{48}$$

As a result of the described modifications, the following system of equations can be obtained:

$$\frac{\partial \bar{u}_i}{\partial t} + \frac{d\bar{u}_i \bar{u}_j}{dx_j} = -\frac{\partial \pi}{\partial x_i} - 2\,\varepsilon_{ijk}\,\Omega_j(\bar{u}_k - G_k) + \frac{g}{\Theta_o}(\bar{\Theta}_v - \Theta_o)\delta_{i3} - \frac{\partial T_{ij}}{\partial x_j}$$

$$\frac{\partial \bar{\Theta}_L}{\partial t} + \frac{\partial \bar{u}_j \bar{\Theta}_L}{\partial x_j} = -\frac{\partial H_{Lj}}{\partial x_j} + \bar{S}$$

$$\frac{\partial \bar{q}_T}{\partial t} + \frac{\partial \bar{u}_j \bar{q}_T}{\partial x_j} = -\frac{\partial Q_{Tj}}{\partial x_j} \tag{49}$$

$$\frac{\partial E}{\partial t} + \frac{\partial \bar{u}_j E}{\partial x_j} = -T_{ij}\,\bar{S}_{ij} + \beta\, H_v - \frac{\partial \Pi_j}{\partial x_j} - \varepsilon$$

$$\frac{\partial \bar{u}_j}{\partial x_j} = 0$$

where $H_v = \overline{u_3\Theta_v} - \overline{u_3}\,\overline{\Theta_v} = -k_h \frac{\partial \overline{\Theta_v}}{\partial x_3}$, $H_{Lj} = -k_h \frac{\partial \overline{\Theta_L}}{\partial x_j}$, $Q_{Tj} = -k_h \frac{\partial \overline{q_T}}{\partial x_j}$, and in addition (33), (40), (41) also apply.

The subgrid buoyancy term in the TKE equation has to be evaluated in terms of the new model variables Θ_L and q_T. For this purpose we have to consider two cases, unsaturated and saturated.

In the unsaturated case, when $q_L = 0$, $q_v = q_T$, $\Theta_L = \Theta$. Based on the definition of the virtual temperature (44), we have (e.g., Cuijpers and Duynkerke,1993):

$$\overline{w'\theta_v'} = (1 + 0.61\, q_T)\,\overline{w'\theta_L'} + 0.61\,\Theta\,\overline{w'q_T'} \tag{50}$$

where the ensemble averaging notation (32) is applied for simplicity, and the new (meteorological) notation is being used: $u_1 = u$, $u_2 = v$, and $u_3 = w$.

In the saturated case, $q_T = q_s + q_L$, $q_v = q_s$, so:

$$\overline{w'\theta_v'} = (1 + 1.61\, q_s - q_T)\,\overline{w'\theta'} + \Theta\,(1.61\,\overline{w'q_s'} - \overline{w'q_T'}) \tag{51}$$

where q_s is the saturation specific humidity. The flux of $\overline{w'q_s'}$ can be evaluated as:

$$\overline{w'q_s'} = \overline{w'\frac{dq_s}{dT}\,\theta'} = 0.622\,\frac{L}{R_d T}\,q_s\,\frac{\overline{w'\theta'}}{\Theta} \tag{52}$$

where the Clausius-Clayperon equation: $\frac{dq_s}{dT} = 0.622\,\frac{L}{R_d T}\,q_s$ was used. Taking into consideration (47), and $q_T = q_s + q_L$, we have:

$$\overline{w'\theta'} = \overline{w'\theta_L'} + \frac{\Theta}{T}\overline{w'q_L'} = \overline{w'\theta_L'} + \frac{\Theta}{T}\frac{L}{C_p}(\overline{w'q_L'} - \overline{w'q_s'}) \tag{53}$$

Inserting (52) and (53) into (51), we obtain:

$$\overline{w'\theta_v'} = \frac{1 - q_T + 1.61 q_s\left(1 + 0.622\frac{L}{R_d T}\right)}{1 + 0.622\frac{L}{R_d T}\frac{L}{C_p T}q_s}\overline{w'\theta_L'} + \Theta\overline{w'q_T'}\left\{\frac{L}{C_p T}\frac{1 - q_T + 1.61\ q_s\left(1 + \frac{0.622\ L}{R_d T}\right)}{1 + 0.622\ \frac{L}{R_d T}\frac{L}{C_p T}q_s} - 1\right\} \tag{54}$$

For the calculation of the subgrid-scale buoyancy terms $\beta\overline{w\theta'_v}$ [Equations (50), or (54)], as a function of the liquid water potential temperature flux $\beta\overline{w\theta'_L}$, and the total water specific humidity flux $\beta\overline{wq'_L}$, it has to be determined whether the grid box is saturated or unsaturated. This is usually done by applying the procedure, described in Sommeria and Deardorff (1977). In the procedure it is assumed that the grid box is unsaturated, as long as the total water specific humidity q_T is below its saturation value, while it is fully saturated, when q_T exceeds it.

The source term *S*, on the right hand side of the temperature equations, includes divergences (*d/dz*) of the longwave upwelling and downwelling radiation fluxes ($F^{\downarrow}, F^{\uparrow}$), and also of the shortwave upwelling and downwelling fluxes ($S^{\downarrow}, S^{\uparrow}$). Radiative cooling/warming, expressed by these fluxes, can significantly influence turbulence, when clouds or fog are present in the ABL.

Typical distribution of the radiative fluxes in the stratus-topped boundary layer is shown in Figure 2. Longwave cooling at the cloud top exists due to the different radiative properties of water vapor and water. Water vapor cannot emit longwave radiation, while water droplets emit as black-body emitters at all longwave frequencies. This leads to a sharp change in the downward flux across the cloud top. The downward longwave flux $F^{\downarrow}$, above the cloud, is smaller than the flux in the cloud layer. On the other hand, the upward flux $F^{\uparrow}$ remains quite uniform with height, with only a slight change at the cloud base, due to the slight difference in temperature.

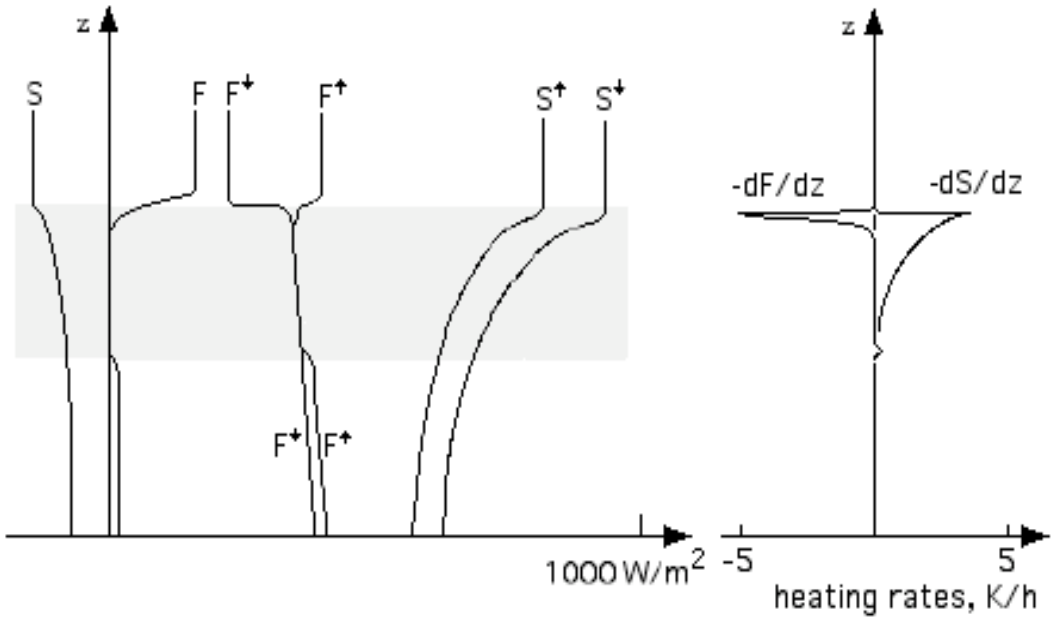

Figure 2. Typical distribution of radiative fluxes in the stratus topped ABL: longwave and shortwave fluxes (upwelling and downwelling fluxes are marked by arrows), net fluxes F and S, and the corresponding heating/cooling rates. The cloud layer is shaded.

The net flux $F = F^{\downarrow} - F^{\uparrow}$ sharply increases with height at the cloud top. The resulting flux divergence leads to a strong cooling (about several K/hour) over a very thin layer (of about 50 m) at the cloud top (a typical clear-air longwave radiation cooling is about 1-2 K/day). Note that the net solar flux $S = S^{\downarrow} - S^{\uparrow}$ inside the cloud is more uniformly distributed. The shortwave heating is smaller than the longwave cooling, and is distributed over a thicker layer within a cloud.

Radiation can be modeled in different ways. In the simplest approach, radiation is parameterized as the sum of two components: a clear sky radiative cooling component, typically taken to be –2 K/day everywhere below the inversion, and a cloud-associated "Beer's law". In the latter, long-wavelength radiative cooling is assumed to be proportional to the liquid-water content and exponentially attenuated. The resulting radiative flux F is (i.e., Moeng, 2000):

$$F(x, y, z) = F_i \exp\left[-\rho_o K_a \int_z^{\infty} q_L(x, y, Z)dZ\right] \tag{55}$$

where F_i is the longwave radiation flux above the cloud, ρ_o is the reference density, K_a is the longwave absorption coefficient, and q_L is the local liquid water mixing ratio. In a more complex approach, the method of Toon et al (1989), or the SBDART model (Santa Barbara DISTORT Atmospheric Radiative Transfer, Ricchiazzi et al, 1998) can be applied.

2.5 Numerical Scheme

Typically, for discretisation of the LES governing equations, a staggered grid (Arakawa's grid C) is used. In this arrangement, the velocity components are defined on the sides of a rectangular grid volume, while scalars, i.e. the pressure, temperature, specific humidity, subgrid TKE, and exchange coefficients are defined in the center. The vertical velocity is defined at the bottom, and at the top of the grid volume, and the components of the stress tensor T as shown in Figure 3.

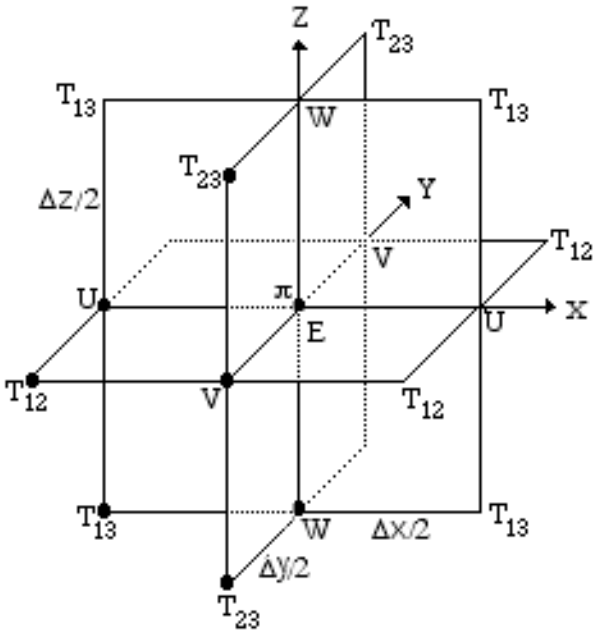

Figure 3. A view of a grid cell centered at a grid point (i, j, k). The variables with indices (i, j, k) are indicated by darkened circles. Note that the velocity components are defined on the sides of a rectangular grid volume, while scalars (i.e. pressure, subgrid TKE, temperature, the specific humidity, and the exchange coefficients) are defined in the center.

The governing differential equations are transformed into finite difference ones, with the advection terms written in flux form. The monotone scheme developed by Beets and Koren (1996) is often applied. The diffusion terms are expressed by using a second-order, spatial central difference scheme. The Coriolis terms are averaged over four points in order to center them at the respective point under consideration. Although this presents no problems, it does mean that total kinetic energy may not be conserved quite as accurately as in the absence of these terms (Deardorff, 1973).

In time-dependent numerical simulations, it is necessary to start with the initial conditions being as realistic as possible, especially for mean wind and temperature structures. Random initial perturbations of substantial amplitude have to be superimposed upon the mean fields of temperature and vertical velocity.

Time-advancement is often executed by using the fourth-order Runge-Kutta method, which is stable and accurate. It can be explained, noting that each LES prognostic equation can be written in the form:

$$\frac{\partial \Phi}{\partial t} = F \tag{56}$$

where Φ is any prognostic variable (i.e., u, v, w, Θ, q, and E). During each time step, the 3-stage numerical scheme is applied for each equation:

$$\begin{aligned} \Phi^{(1)} &= \Phi^{(m)} + \Delta t_1 \, (C_{11} \; F^{(m)} + C_{21} \, F^{(m-1)}) \\ \Phi^{(2)} &= \Phi^{(1)} + \Delta t_2 \, (C_{12} \; F^{(1)} + C_{22} \, F^{(m)}) \\ \Phi^{(m+1)} &= \Phi^{(2)} + \Delta t_3 \, (C_{13} \; F^{(2)} + C_{23} \, F^{(1)}) \end{aligned} \tag{57}$$

where m, $m+1$ are moments of time. The coefficients in (57) are defined as follows: $C_{11} = 8/15$, $C_{12} = 5/12$, $C_{13} = 3/4$, $C_{21} = 0$, $C_2 = -17/60$, $C_{23} = -5/12$. At each stage the most current values of Φ are used in the functional evaluation. The time steps Δt_1, Δt_2, Δt_3 are calculated at each stage from the Courant-Friedrichs-Levy condition (1928):

$$n = \Delta t_i \max_j \left(|u_j| / \Delta x_j \right) \tag{58}$$

where n is a Courant-Friedrichs-Levy number, assumed to be 0.20, and i = 1, 2, 3. The total time step is $\Delta t = \Delta t_1 + \Delta t_2 + \Delta t_3$.

The Courant-Friedrichs-Levy condition can be alleviated by allowing the coordinate system to translate downstream with the approximate speed U_i of the average flow. Consequently, translating variables can be introduced: $x_{i(g)} = x_i - U_i \, t$, $u_{i(g)} = u_i - U_i$. In such a Galilean transformation, it must be remembered that the translation speed needs to be taken into account when formulating the lower boundary condition on the stress and the heat flux (with $u_i = u_{i(g)} + U_i$), and also with respect to the Coriolis terms, which are transformed as: $f \, (u_i - G_i) = f \, (u_{i(g)} + U_i - G_i)$, where G_i is the component of the geostrophic wind, and f is the Coriolis parameter.

At the lower boundary, the vertical velocity w is set to equal zero. It is also assumed that $\partial E / \partial z = 0$ for the TKE. For horizontal velocities one resorts to the Monin-Obuhkov similarity. This is because profiles near the surface are strongly curved. This curvature cannot be resolved within the first grid cell. This means that a relation is specified between the surface stress and the horizontal velocity in the first grid cell. Furthermore, it is assumed that the velocity and stress are parallel. Surface similarity is then used to obtain the surface temperature T, from the temperature calculated in the center of the first grid cell.

With respect to the upper boundary conditions, it is assumed: $\partial u/\partial z = \partial v/\partial z = w = T_{13} = T_{23} = \partial E/\partial z = H_3 = 0$. The temperature gradient at the top of the calculation domain is set equal to the gradient Γ, which is prescribed in the initial conditions as the temperature gradient above the boundary layer. The horizontal boundary conditions are assumed to be periodic (Figure 4).

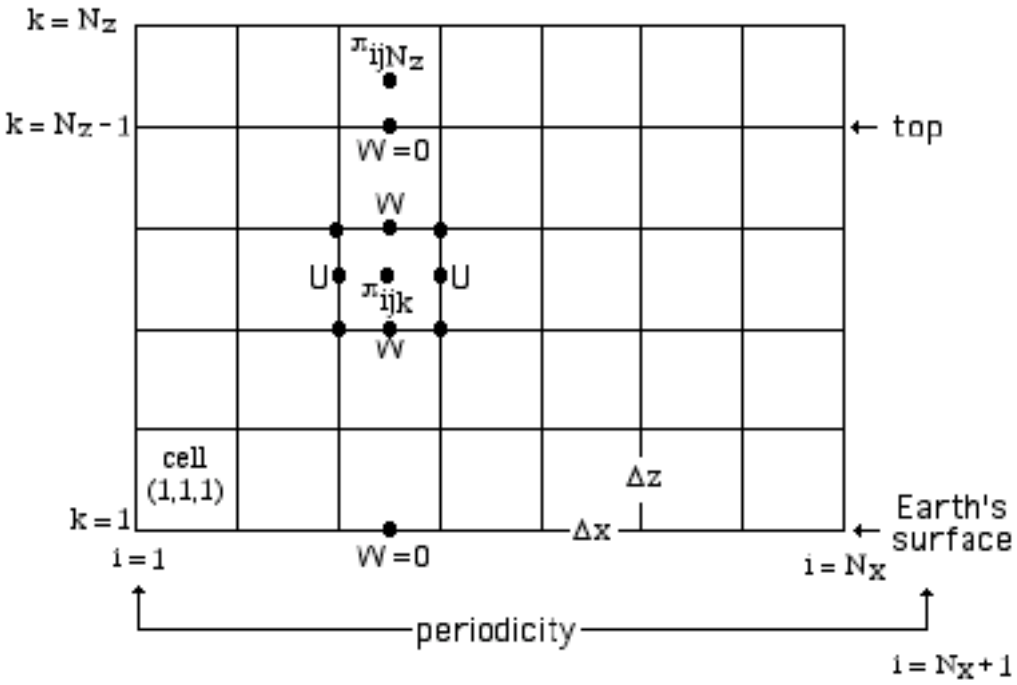

Figure 4. The side view of the mesh. At the lower boundary (the earth's surface), and at the level k=Nz-1 (top level of the model), the vertical velocity w is set to zero. Values in cells located above the top level are calculated based on boundary conditions.

To avoid reflecting gravity waves from the top of the domain, a damping layer is used. The role of the damping layer is to dissipate gravity waves before they can reflect back into the boundary layer. This is accomplished by adding a relaxation term in the form $r(\Phi - \Phi_o)$ to the equations of motion in the upper part of the domain, where Φ is a prognostic parameter, and Φ_o is its value near the top of the domain. The relaxation term dampens fluctuations at time scales larger than a prescribed relaxation time scale $\tau = 1/r$. The relaxation parameter is a function of height:

$$r(z) = r_o \{1 - \cos [\pi (z - z_b)/(z_T - z_b)]\}/2 \qquad (59)$$

where r_o is a given relaxation constant (order of 0.01 s^{-1}), z_T and z_b indicate the top of the computational domain and the bottom of the damping layer respectively.

Often there is need to consider a large-scale vertical motion, referred to as subsidence W. Subsidence can be included by adding source terms representing the downward advection (e.g., $-W\,\partial\Theta/\partial z$). These terms are relatively small and should be included only in the thermodynamic equations for temperature and humidity (and other scalars), where they can be important in maintaining long-term balances. In the boundary layer, the subsidence velocity can be assumed to be given by $W = -D\,z$, where D is the large-scale divergence. Above the ABL, can be set to $W = -D\,z_i$.

To find pressure, one might consider Equation (56), written only for velocity components, u, v, w. The functions F should be expressed in a form, in which the pressure terms are singled out:

$$\begin{aligned} F_u &= f_u - \partial\pi/\partial x \\ F_v &= f_v - \partial\pi/\partial y \\ F_w &= f_w - \partial\pi/\partial z \end{aligned} \tag{60}$$

Based on (57),(60), we will obtain for the first partial time step:

$$\begin{aligned} u^{(1)} &= D_u^{(m)} - C_{11}\,\Delta t_1\,\partial\pi/\partial x \\ v^{(1)} &= D_v^{(m)} - C_{11}\,\Delta t_1\,\partial\pi/\partial y \\ w^{(1)} &= D_w^{(m)} - C_{11}\,\Delta t_1\,\partial\pi/\partial z \end{aligned} \tag{61}$$

where

$$\begin{aligned} D_u^{(m)} &= u^{(m)} + \Delta t_1\,(C_{11}\,f_u^{(m)} + C_{21}\,F_u^{(m-1)}) \\ D_v^{(m)} &= v^{(m)} + \Delta t_1\,(C_{11}\,f_v^{(m)} + C_{21}\,F_v^{(m-1)}) \\ D_w^{(m)} &= w^{(m)} + \Delta t_1\,(C_{11}\,f_w^{(m)} + C_{21}\,F_w^{(m-1)}) \end{aligned} \tag{62}$$

Note that analogous expressions are obtained for the sequential partial time steps,

The continuity equation can be written in the finite differences form:

$$\delta_x u^{(1)} + \delta_y v^{(1)} + \delta_z w^{(1)} = 0 \tag{63}$$

where

$$\begin{aligned} \delta_x u^{(1)} &= (u^{(1)}{}_{i+1,j,k} - u^{(1)}{}_{i,j,k})/\Delta x \\ \delta_y v^{(1)} &= (v^{(1)}{}_{i,j+1,k} - v^{(1)}{}_{i,j,k})/\Delta y \end{aligned} \tag{64}$$

$$\delta_z w^{(1)} = (w^{(1)}_{i,j,k+1} - w^{(1)}_{i,j,k}) / \Delta z$$

and the indices, *i, j,* and *k*, refer to a cell number (see Figure 4). Substituting (61) into (63) yields the pressure equation:

$$\delta_{xx}\, \pi_{i,j,k} + \delta_{yy}\pi_{i,j,k} + \delta_{zz}\, \pi_{i,j,k} = G_{i,j,k} \tag{65}$$

where

$$\delta_{xx}\, \pi_{i,j,k} = (\pi_{i+1,j,k} - 2\, \pi_{i,j,k} + \pi_{i-1,j,k}) / \Delta x^2$$

$$\delta_{yy}\, \pi_{i,j,k} = (\pi_{i,j+1,k} - 2\, \pi_{i,j,k} + \pi_{i,j-1,k}) / \Delta y^2$$

$$\delta_{zz}\, \pi_{i,j,k} = (\pi_{i,j,k+1} - 2\, \pi_{i,j,k} + \pi_{i,j,k-1}) / \Delta z^2$$

$$G_{i,j,k} = [\delta_x D_u^{(m)} + \delta_y D_v^{(m)} + \delta_z D_w^{(m)}] / (C_{11}\, \Delta t_1)$$

for $i = 1,..., N_x$, $j = 1,..., N_y$, $k = 1,..., N_z-1$, and the operators δ_x, δ_y ,and δ_z are defined as in (64). Employing (61)-(64) and assuming the vertical velocity $w_{i,j,1} = w_{i,j,NZ-1} = 0$, yields the vertical boundary conditions for pressure:

$$\begin{aligned} (\pi_{i,j,2} - \pi_{i,j,1}) / \Delta z^2 &= R_{i,j,1} - L_1 \qquad \text{for } k = 1 \\ -(\pi_{i,j,Nz} - \pi_{i,j,Nz-1}) / \Delta z^2 &= R_{i,j,Nz-1} + L_{Nz-1} \qquad \text{for } k = Nz - 1 \end{aligned} \tag{66}$$

where

$$L_k = (\pi_{i+1,jk} - 2\, \pi_{i,j,k} + \pi_{i-1,j,k}) / \Delta x^2 + (\pi_{i,j+1,k} - 2\, \pi_{i,j,k} + \pi_{i,j-1,k}) / \Delta y^2$$

$$R_{i,j,1} = (\delta_x D_u^{(m)}{}_{i,j,1} + \delta_x D_v^{(m)}{}_{i,j,1} + D_w^{(m)}{}_{i,j,2}) / (C_{11}\, \Delta t_1)$$

$$R_{i,j,Nz-1} = (\delta_x D_u^{(m)}{}_{i,j,Nz-1} + \delta_x D_v^{(m)}{}_{i,j,Nz-1} - D_w^{(m)}{}_{i,j,Nz-1}) / (C_{11}\, \Delta t_1)$$

Because of the assumed periodic boundary conditions, we will express the variables in (65)-(66) in a spectral form:

$$\begin{aligned} \pi_{ijk} &= \sum_{m=0}^{N_x-1} \sum_{n=0}^{N_y-1} p\ (m,\ n,\ k)\ \exp\left[\ 2\Pi\ I\ \left(\ \frac{i\ m}{N_x} + \frac{j\ n}{N_y}\ \right)\ \right] \\ G_{ijk} &= \sum_{m=0}^{N_x-1} \sum_{n=0}^{N_y-1} g\ (m,\ n,\ k)\ \exp\left[\ 2\Pi\ I\ \left(\ \frac{i\ m}{N_x} + \frac{j\ n}{N_y}\ \right)\ \right] \end{aligned} \tag{67}$$

where $\Pi = 3.14...$, $I = \sqrt{-1}$. After the substitution of (67) into (65) we will have:

$$p(m,n,k+1) - [1 + S(m,n)]\, p(m,n,k) + p(m,n,k-1) = g(m,n,k)\, \Delta z^2 \qquad (68)$$

where $S(m,n) = 4\frac{\Delta z^2}{\Delta x^2} \sin^2(\frac{\Pi m}{N_x}) + 4\frac{\Delta z^2}{\Delta y^2} \sin^2(\frac{\Pi n}{N_y})$. Analogous equations for the boundary conditions can be obtained. The term *g(m,n,k)* can be calculated based on G_{ijk} using the fast Fourier transformation (FFT) subroutine.

Note that (68) constitutes a tri-diagonal system of algebraic equations, which can be solved by employing the factorization method. It is worth mentioning that the case $m = n = 0$ has to be treated separately, i.e., *p(0, 0, k)* has to be set to an arbitrary constant (e.g., zero), because the pressure is calculated with an accuracy to a constant. Based on *p(m, n, k)* the pressure π can be calculated by using the reverse FFT subroutine.

Finally, it should be mentioned that the solutions of the governing LES equations are obtained in a form of fields, which are variable in space and time. Therefore, LES results are usually presented as horizontally and time averaged parameters, defined as

$$< u_i > = \frac{1}{L_x\, L_y\, T} \int_0^{t_0+T} \int_0^{L_x} \int_0^{L_y} u_i(x, y, z, t)\, dx\, dy\, dt \qquad (69)$$

where L_x and L_y define the horizontal domain of a simulation, and T is the time averaging period. Consequently, any LES parameter can be expressed as a mean value and a fluctuation, e.g.:

$$\begin{aligned} u_i(x,y,z,t) &= <u_i>(z) + u_i'(x,y,z,t) \\ \Theta(x,y,z,t) &= <\Theta>(z) + \Theta'(x,y,z,t) \end{aligned} \qquad (70)$$

Note that any total flux

$$H_{total} = <\Theta' u_i'> + <H_i> \qquad (71)$$

consists of the resolvable flux $<\Theta' u_i'>$, which is derived from a LES simulation using (69)-(70), and a subgrid flux $<H_i>$, which is obtained by averaging of subgrid fluxes (modeled within a LES).

3 The ABL Simulations

Flow in the boundary layer over land is primarily controlled by the diurnal cycle of the earth's surface energy budget. During the day, a portion of the energy

gained at the earth's surface is transferred to the atmosphere as a sensible heat flux, and also used in the evaporation process. This transfer can generate vertical motions, called convection. At night, convection stops, and turbulence in the cloud-free ABL can only be generated by wind shear and radiative cooling.

The structure of the ABL is usually classified into four characteristic types: convective, neutral, stable, and cloud-topped. These four prototypes of the ABL have been intensively studied during the last several decades. The LES technique has been especially helpful in this respect. Examples of such simulations are presented below.

3.1 The Convective ABL

3.1.1 Free Convection

Free-convection refers to calm (no mean wind) conditions, controlled only by the strength of the surface heat flux. It is numerically the simplest to achieve, because the horizontal domain can be relatively small, while a simulation is relatively short. The boundary conditions during such simulations usually remain unchanged. Consequently, the obtained results are equivalent to the ABL around the solar noon, when all fluxes are approximately constant within a period of about two hours.

Forcing applied at two surfaces, limiting the convective atmospheric boundary layer, the underlying one, where convection is originated, and the upper one, where it is constrained, causes the convective ABL to have a multilayer structure. It consists of the surface layer near the earth's surface, the mixed layer above it, and the interfacial layer next to the free atmosphere (see Chapter 4 in volume I of this book series). The convective surface layer is characterized by a sharp decrease in the potential temperature with height. In the mixed layer, the temperature gradient decreases to zero. In the interfacial layer, there is a sharp increase in the potential temperature with height (as shown in Figure 7a).

Convection in the shearless mixed layer (its animation can be found at the web site: http://www.mmm.ucar.edu/asr96/sullivan1.html) is organized in a form of characteristic cell patterns, depicted in Figure 5. Regions of slowly sinking air are surrounded by the areas with updrafts (shaded areas in the figure). Downdrafts cover more than half the area of the horizontal plane over the bulk of the mixed layer depth. Such organization of convection is responsible non-Gaussian behavior of convective diffusion [Deardorff (1972), Willis and Deardorff (1976, 1978, 1981)]. For elevated sources the average plume centerline, defined as the mean maximum concentration, descends within a short distance from the source until it reaches the ground. In contrast, the average centerline from near surface releases ascends after a short downwind distance.

Experiments performed by Deardorff (1970) showed that the characteristic of turbulence in the mixed layer can be expressed in terms of similarity scales in the form:

$$
\begin{aligned}
w_* &= (\beta z_i H_o)^{1/3} && \text{for vertical velocity,} \\
\Theta_* &= H_o/w_* && \text{for temperature,} \\
q_* &= Q_o/w_* && \text{for a passive scalar,} \\
z_i & && \text{for height,} \\
\tau_* &= w_*/z_i && \text{for time,}
\end{aligned}
\tag{72}
$$

where H_o and Q_o are the surface (virtual) potential temperature and scalar fluxes (of water vapor, CO_2, O_3, etc), $\beta = g/T_o$ is the buoyancy parameter, and z_i is the depth of the mixed layer, traditionally defined as a level at which the heat flux H_o is the most negative.

Since there is only one height scale, one temperature scale, and one humidity scale in (72), dimensionless statistics of turbulence in the ABL are expected to be unique functions of a single non-dimensional parameter z/z_i. Observations show (e.g., Sorbjan, 1991), however, that in the upper portion of the mixed layer, a substantial scatter of dimensionless quantities exists, especially for statistics of scalars (temperature, humidity, concentration of passive scalars). This indicates that the set of scales (1) is incomplete.

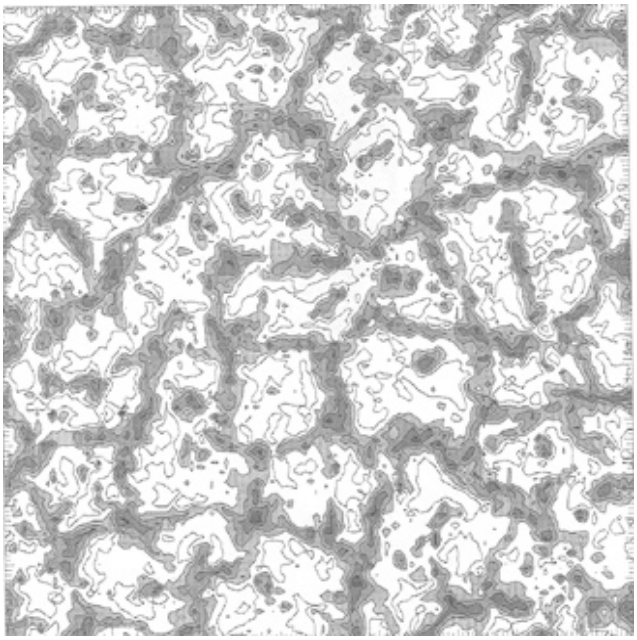

Figure 5. Horizontal cross-section of the LES generated vertical velocity field at $z/z_i = 0.3$ during free convection. Shaded areas indicate updrafts.

The described scatter can be related to a strong sensitivity of statistical moments at the top of the mixed layer to values of the potential temperature gradient γ_i in the interfacial layer (Sorbjan, 1996 a, b). For example, the (negative) ratio of the heat fluxes at the top and bottom of the mixed layer $(-H_i/H_o)$ increases when γ_i increases, and decreases when γ_i decreases to zero. This indicates that γ_i should be treated as an independent scaling parameter for temperature. Analogously, scalar gradients g_i at the top of the mixed layer should be treated as additional scaling parameters for other scalars.

The temperature gradient γ_i changes from case to case, due to advective transformations, and also during morning transitions from stable to convective conditions. Depending on the intensity of nocturnal cooling, γ_i in the capping inversion above the evolving morning mixed layer occurs in a broad range of values, from circa 0,001 K m^{-1} to 0.1 K m^{-1}. Also the scalar gradient g_i varies strongly, depending on the content of a scalar q in the mixed layer and in the free atmosphere.

The inclusion of scalar gradients, γ_i and g_i, as governing parameters introduces alternate similarity scales, valid in the interfacial layer (Sorbjan, 2004a):

$$
\begin{aligned}
S_w &= w_* && \text{for vertical velocity,} \\
S_\theta &= \gamma_i\, w_* / N_i && \text{for temperature,} \\
S_q &= g_i\, w_* / N_i && \text{for humidity (or other scalar),} \\
S_h &= w_* / N_i && \text{for height,} \\
S_t &= 1/ N_i && \text{for tim,}
\end{aligned}
\qquad (73)
$$

where $N_i = [\beta\gamma_i]^{0.5}$ is the Brunt-Väisäla frequency in the interfacial layer. Temperature scale S_θ is dependent on the surface heat flux (through w_*) and the temperature gradient γ_i. The passive scalar scale S_q depends on the surface heat flux, the temperature gradient γ_i, and also on the scalar gradient g_i.

To further discuss the free-convective case, let us consider the results of two LES (referred to as A and B), which employed a mesh of 64 x 64 x 60 grid points (Sorbjan, 2004b). The grid increments were $\Delta x = \Delta y = 40$ m, and $\Delta z = 30$ m. The initial mixed layer was 600 m deep, with a uniform potential temperature of 299 K. The interfacial layer was initially 150 m thick. In run A, the initial temperature gradient γ_i in the interfacial layer was equal to 0.01 K m^{-1}, while in run B, it was 0.1 K m^{-1}. In the free-atmosphere, the temperature gradient was assumed to be Γ = 0.003 K m^{-1}. The surface heat flux H_o was assumed equal to 0.075 K m s^{-1}. The simulation time was 26529.4 s in run A and 28459.1 s in run B (i.e., 5000 total time steps).

Figure 6 shows the time history of the mixed layer depth z_i (defined as the height, where the heat flux is most negative) and the surface temperature T_o. The curves representing T_o are alike during both simulations, showing a 3K-increase of the surface temperature. The curves representing z_i diverge in their steepness and smoothness. This indicates that the structure of turbulence at the bottom of the mixed layer in both runs is comparable (because the value of the surface heat flux in both runs is the same), and it differs at the top (because the values of γ_i in both runs are different).

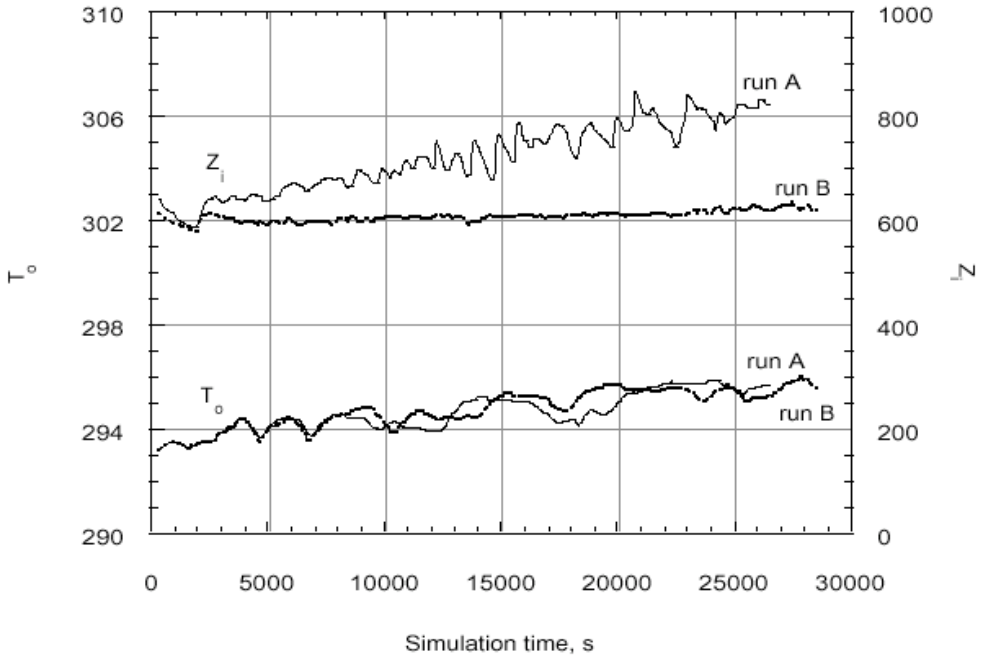

Figure 6. Time history of the averaged height of the mixed layer z_i, and the surface temperature T_o, obtained in free-convective runs A and B.

Figure 7 depicts profiles of the potential temperature Θ, its dimensionless flux, and variance. In run A, the dimensionless heat flux at the top of the mixed layer H_i/H_o = -0.15, while in Run B, it is about -0.3. There is a substantial difference in the values of the temperature variances $\sigma_{\theta i}^2/\Theta_*^2$ at the top of the mixed layer in both runs. In run A, the peak dimensionless variance is about 8, while in run B it is about 40.

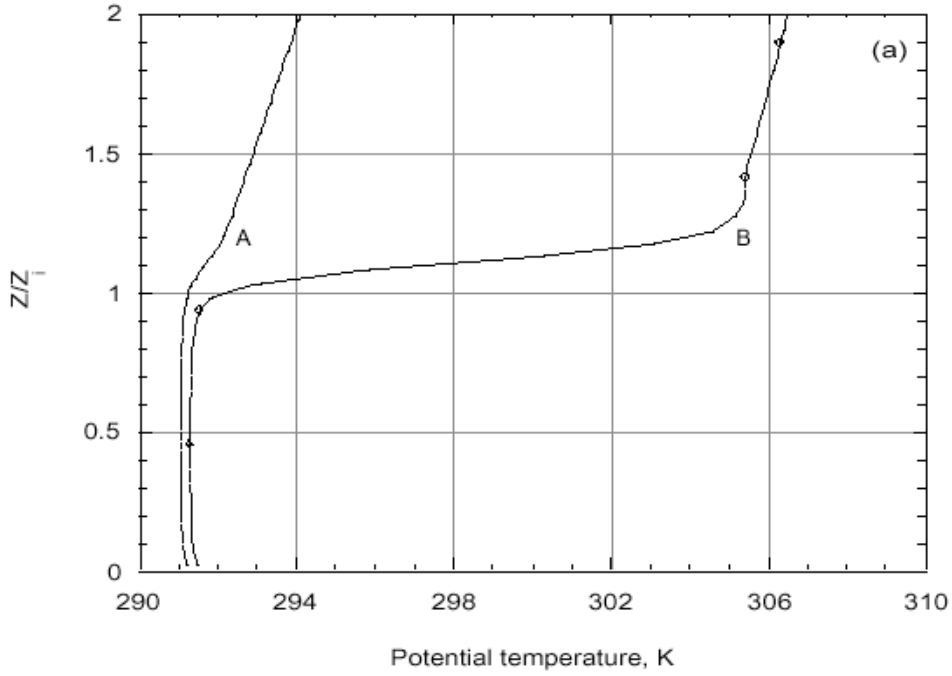
(a)
A
B
Z/Z_i
Potential temperature, K
2
1.5
1
0.5
0
290
294
298
302
306
310

(a)

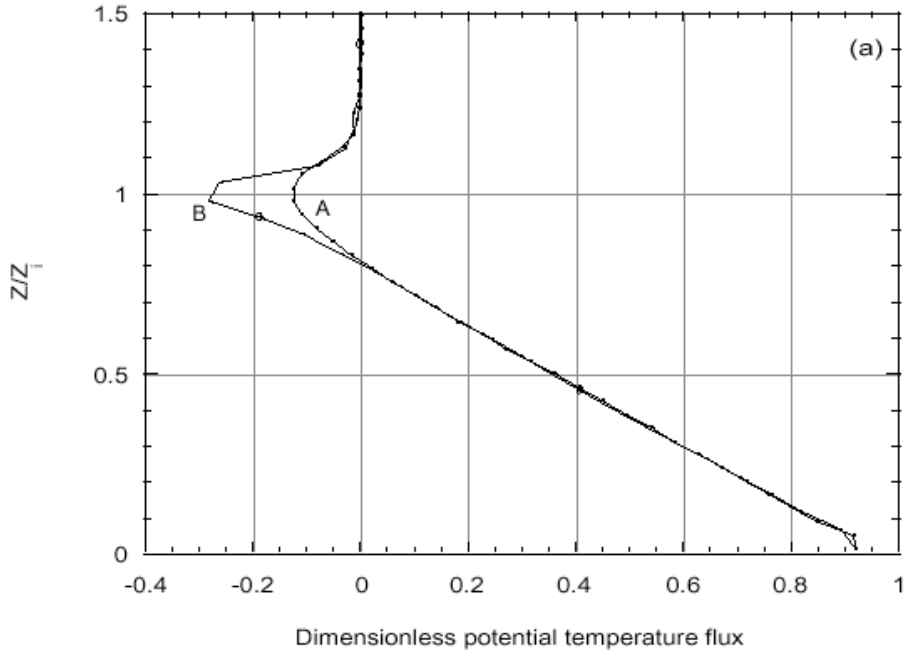
(a)
A
B
Z/Z_i
Dimensionless potential temperature flux
1.5
1
0.5
0
-0.4
-0.2
0
0.2
0.4
0.6
0.8
1

(b)

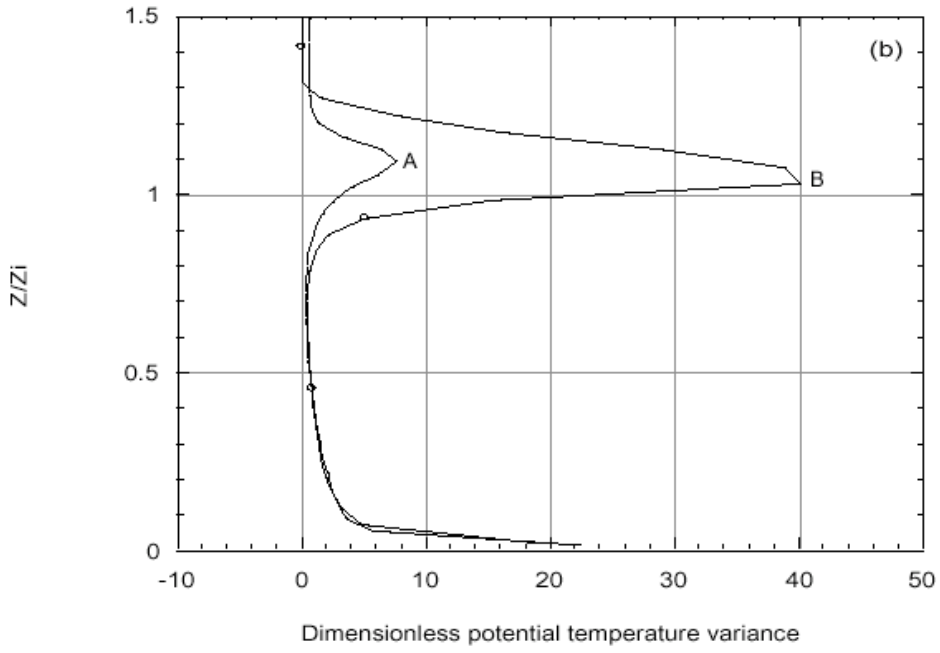

(c)

Figure 7. Vertical profiles of: (a) potential temperature, (b) its dimensionless flux, (c) its dimensionless variance in free-convective runs A and B. Diamonds are used to mark run B. The convective scaling (72) is applied.

Profiles of dimensionless velocity variances are shown in Figure 8. There are relatively small differences between profiles of the velocity variances σ_u^2/w_*^2 and σ_w^2/w_*^2 in runs A and B. The values of the horizontal velocity variances in the mixed layer increase slightly when γ_i increases, and the values of the vertical velocity variances decrease. For the purpose of the mixed layer parameterizations, the influence of γ_i on the velocity statistics could be neglected.

The characteristic (e.g., peak) values of the second moments at the top of the mixed layer can be related to the interfacial scales (2) in the following way (Sorbjan, 2004a, b):

$$H_i = -c_H S_w S_\theta$$

$$Q_i = -c_Q S_w S_q$$

$$\sigma_{\theta i}{}^2 = c_\theta S_\theta{}^2 \tag{74}$$

$$\sigma_{qi}{}^2 = c_q S_q{}^2$$

$$C_{\theta qi} = c_{\theta q} S_\theta S_q$$

where the index "i" refers to the interfacial layer, $C_{\theta q}$ is the temperature-humidity covariance, and the minus in the first two expressions is added in order to stress that the fluxes and gradients are inversely proportional. The parameters c_H, c_Θ, c_Θ, c_θ, and $c_{\theta q}$ are anticipated to be constant.

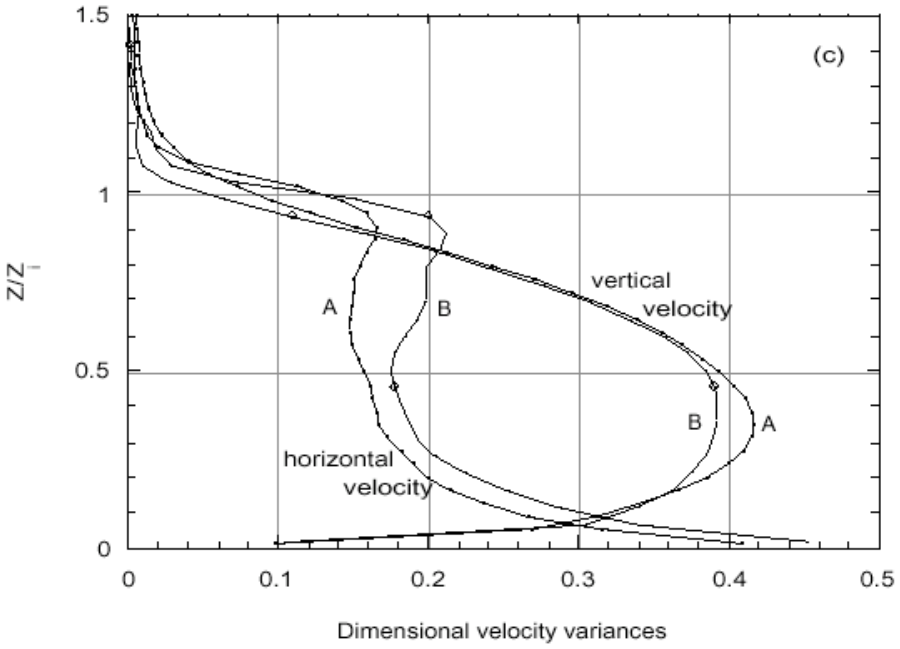

Figure 8. Vertical profiles of dimensionless horizontal σ_u^2/w_*^2 and vertical σ_w^2/w_*^2 velocity variances, obtained in runs A and B. Diamonds are used to mark run B.

The comparison of values given by Equation (74a) with the LES results is shown in Figure 9. In the Figure, the values obtained from Lilly's (1969) classical expression for the entrainment heat flux ($H_i = -\Delta\Theta\ dz_i/dt$, where $\Delta\Theta$ is the temperature jump at the top of the mixed layer) are also depicted. The expression was originally obtained for the stratocumulus-topped ABL, with a sharp temperature jump $\Delta\Theta$ in an infinitesimally thin interfacial layer. It has been commonly used in cloud-free conditions, even though the underlying assumptions regarding the infinitesemal depth of the interfacial layer are not valid in this case. The expression (74a) seems to be a better approximation of the obtained LES results for larger heat flux ratios, and therefore could be treated as an alternative to Lilly's equation for the cloud-free case.

Based on (74), statistical moments of scalars during free-convection can be expressed in terms of two semi-empirical similarity functions F_m and F_i of the dimensionless height z/z_i (Sorbjan, 2004 a, b):

$$M = S_m F_m (z/z_i) + S_i F_i (z/z_i) \tag{75}$$

where M is a statistical moment, S_m is a combination of the mixed layer scales (72), S_i is a combination of the interfacial scales (73), and F_m and F_i are arbitrary, best-fit functions of a dimensionless argument z/z_i.

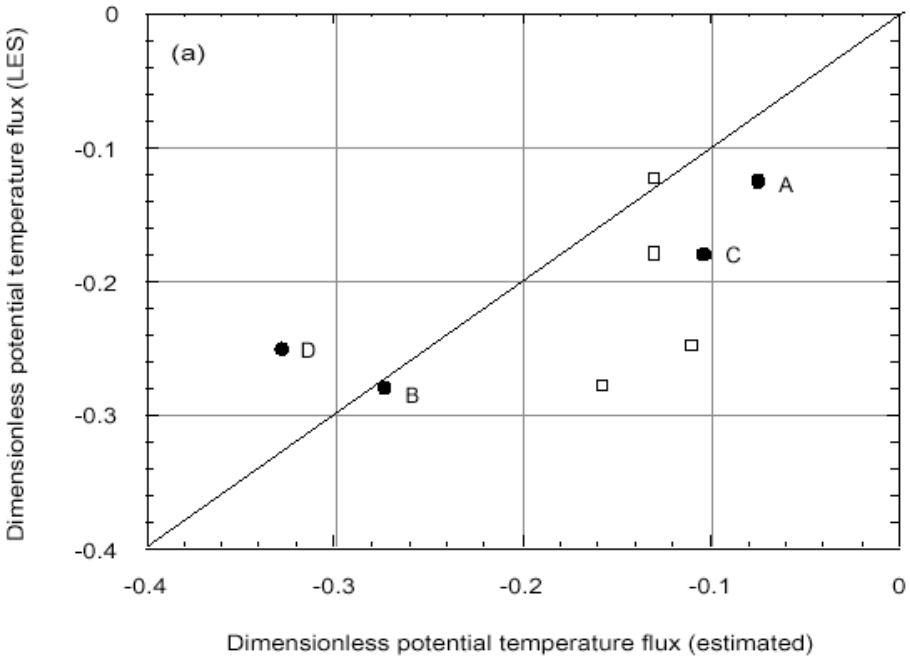

Figure 9. Comparison of the simulated (LES) and estimated from Equation 74a values of the temperature flux ratio H_i/H_o (dark circles). The squares indicate the values calculated based on Lilly's (1969) expression $H_i = \Delta\Theta\, dz_i/dt$.

For example, in the case of the heat flux and humidity fluxes, Equation 75 takes the following linear form in the mixed layer (for $z/z_i < 1$):

$$\begin{aligned} H &= w_*\Theta_* (1 - z/z_i) - c_H S_w S_\theta z/z_i \\ Q &= w_* q_* (1 - z/z_i) - c_Q S_w S_q z/z_i \end{aligned} \tag{76}$$

For the variances and covariances, the following expressions could be proposed:

$$\begin{aligned} \sigma_\theta^2 &= c_1 \ \Theta_*^{\,2} \frac{(1 - z/z_i)}{(z/z_i)^{2/3}} + c_\theta \ S_\theta^2 \frac{(z/z_i)^9}{(2.05 - z/z_i)^8} \\ \sigma_q^2 &= c_2 \ q_*^{\,2} \frac{(1 - z/z_i)^8}{(z/z_i)^{2/3}} + c_q \ S_q^2 \left[\frac{(z/z_i)^3}{(2.2 - z/z_i)^5} + c_s \right] \\ C_{\theta q} &= c_3 \ \Theta_* q_* \frac{(1 - z/z_i)}{(z/z_i)^{2/3}} + c_{\theta q} S_\theta S_q \frac{(z/z_i)^8}{(2.2 - z/z_i)^8} \end{aligned} \tag{77}$$

and also

$$\frac{d\Theta}{dz} = -\frac{\Theta_*}{z_i}\ \frac{(1-z/z_i)^4}{(z/z_i)^{4/3}} + \frac{S_\theta}{S_h}\frac{(z/z_i)^9}{(2.23-z/z_i)^9}$$

$$\frac{dq}{dz} = -\frac{q_*}{z_i}\ \frac{(1-z/z_i)^4}{(z/z_i)^{4/3}} + \frac{S_q}{S_h}\frac{(z/z_i)^9}{(2.23-z/z_i)^9} \tag{78}$$

where c_H , c_Θ , c_Θ, c_1, c_2, c_θ, $c_{\theta q}$ are empirical constants, and all the expressions are valid below the level, at which a moment has its peak (roughly, $z/z_i < 1.1$). For small z, Equation 77 coincides with the Monin-Obukhov similarity predictions.

3.1.3 Forced Convection

During forced convection, turbulence is controlled not only by the strength of the surface heat flux, but also by wind shear. The presence of a sufficiently strong wind breaks the free-convective cells (Figure 5) and replaces them with horizontal rolls**,** depicted in Figure 10. The forced-convection case is numerically more difficult to achieve because the horizontal domain needs to be larger (several times larger that z_i), while a simulation must be longer (in terms of time steps) than in the free-convective case.

Let us consider six LES runs of the forced convection case, with a mesh of 64 x 64 x 60 grid points, and the grid increments $\Delta x = \Delta y = 40$ m, and $\Delta z = 30$ m (Sorbjan, 2004c). All the runs have been obtained for three values of the geostrophic wind G, and for two values of the temperature gradient γ_i in the interfacial layer. The performed runs hereafter are referred to as W05, W10, W15, S05, S10, and S15, where the letter "W" indicates runs, for which the initial temperature inversion strength γ_i was relatively weak, and equal to 0.01 K m^{-1}. The letter "S" denotes runs with stronger temperature gradients in the interfacial layer, equal to 0.1 K m^{-1}. The numbers 05,10 and 15 express the assumed values of the geostrophic wind in m s^{-1}. The simulation time was 30460.3 s in run W05 and 14109.6 s in run W15 (10,000 total time steps).

Figures 11 a-b shows the resulting profiles of the potential temperature, and wind velocity components. Two families of temperature profiles are depicted in Figure 11 a, one with a small temperature jump in the interfacial layer (runs W05, W10 and W15), and the other with a large one (runs S05, S10 and S15). There are three families of u-component velocity (Figure 11 b) associated with the values of the geostrophic wind, 5,10 and 15 m s^{-1}.

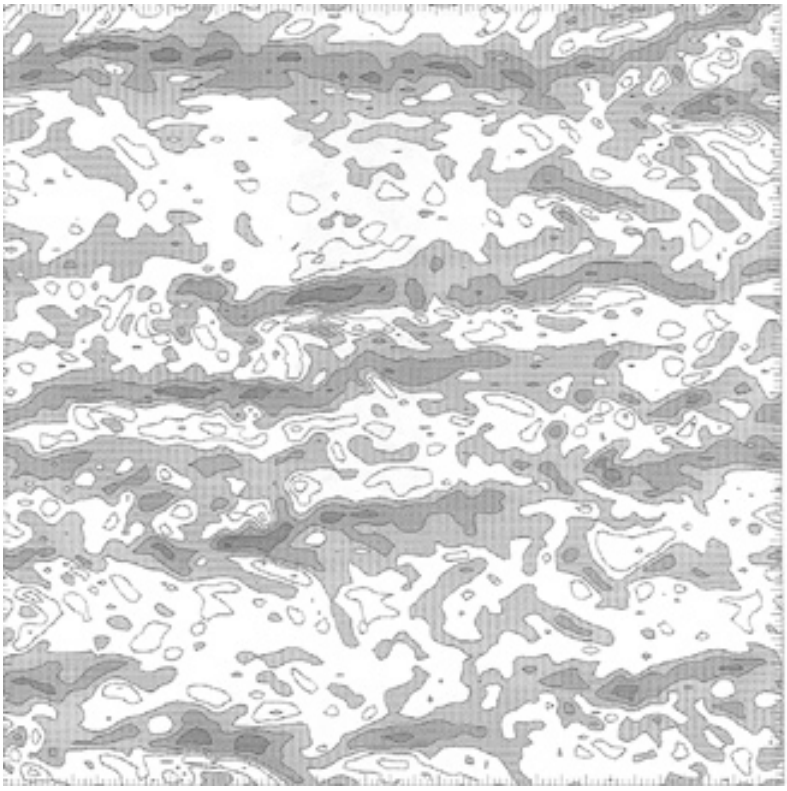

Figure 10. Horizontal cross-section of the LES generated vertical velocity field at $z/z_i = 0.3$ during forced convection. Shaded areas indicate updrafts.

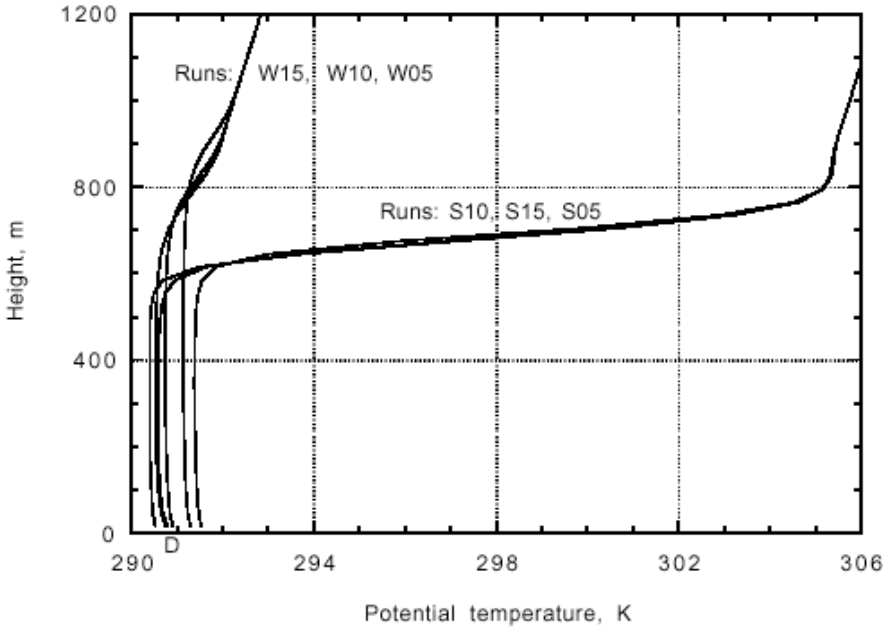

(a)

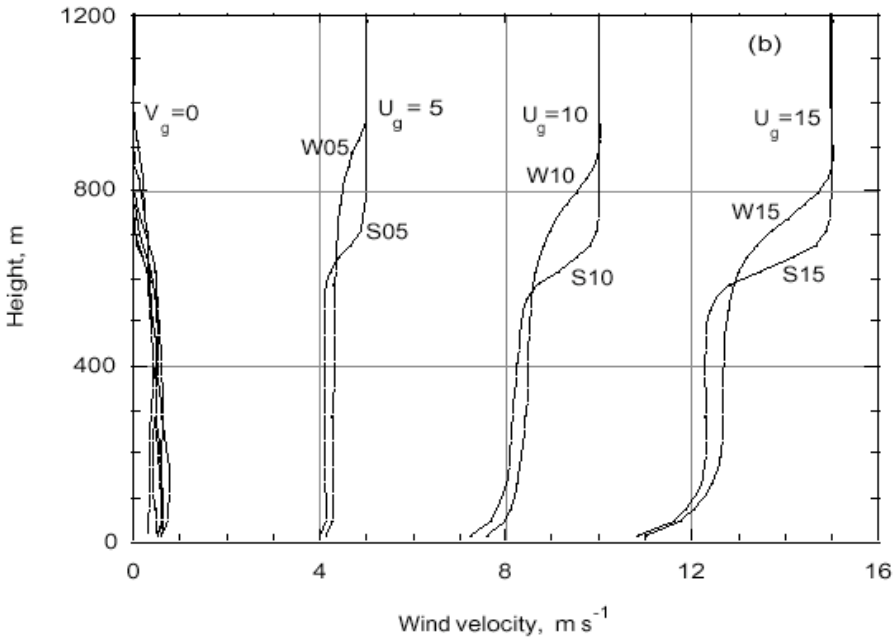

Figure 11. Vertical profiles of: (a) potential temperature, (b) wind velocity components during forced-convective LES runs W05, S05, W10,S10, W15 and S15.

In Figures 12 a-b, the second moments of the potential temperature are shown**.** Figure 3a indicates that the negative peak values of heat flux H_i increase with the strength of the capping inversion γ_i, and with the value of the geostrophic wind G. The same conclusion applies to the temperature variance $\sigma_{\theta i}^2$ in Figure 3b (note spurious consequences of a sharp temperature gradient in run S15). The dependence of $\sigma_{\theta i}^2$ on the temperature gradient γ_i is much stronger than on the geostrophic shear.

The second moments of the horizontal and vertical velocity are shown in Figures 13 a-b. The mixed layer values of the horizontal velocity variances σ_u^2/w_*^2 increase when the geostrophic wind increases and seem to be independent of γ_i The values of the vertical velocity variances σ_{wi}^2/w_*^2 at the top of the mixed layer increase when both γ_i and G increase (note spurious consequences of a sharp velocity gradients near the earth's surface).

When wind shear is present, Equation (75) is not valid, because statistics of turbulence at the top of the mixed layer are dependent not only on the temperature gradient γ_i, but also on velocity gradients $s_{xi} = du/dz|_i$ and $s_{yi} = dv/dz|_i$ in the interfacial layer, or equivalently on the interfacial Richardson number (Sorbjan, 2004 a, c):

$$\mathrm{Ri} = \frac{\beta\, \gamma_\mathrm{i}}{s_{\mathrm{x}\mathrm{i}}^{\,2} + s_{\mathrm{y}\mathrm{i}}^{\,2}} \tag{79}$$

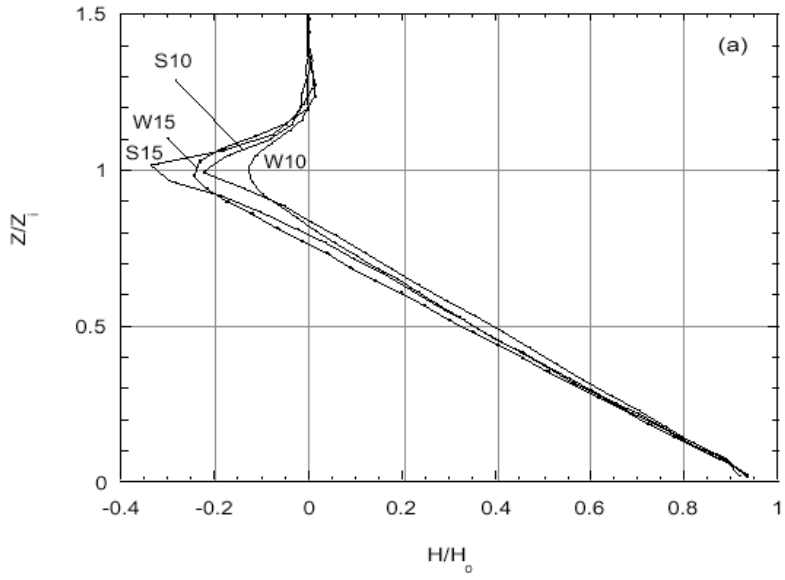

(a)

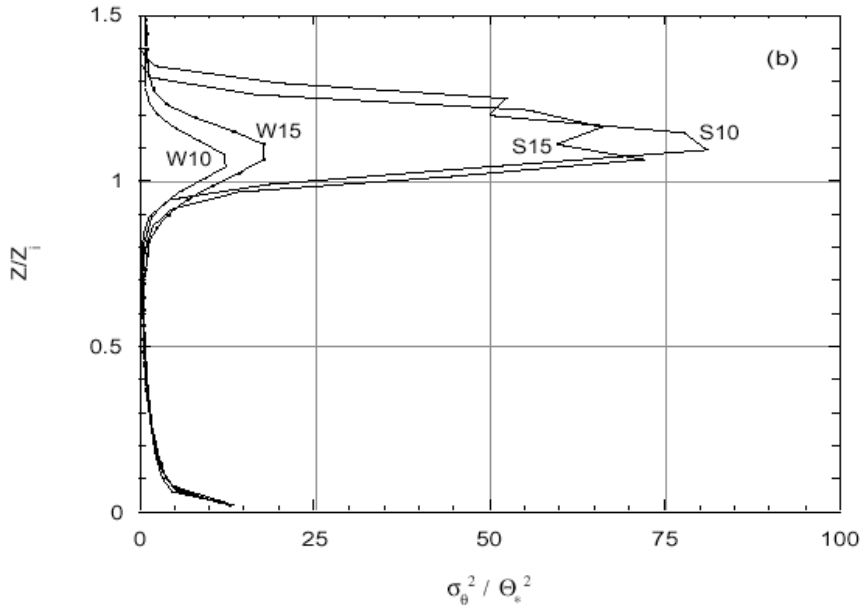

(b)

Figure 12. Vertical profiles of: (a) potential temperature flux H/H_0, (b) potential temperature variance $\sigma_\theta^2/\Theta_*^2$, obtained in runs W10, W15, S10, and S15.

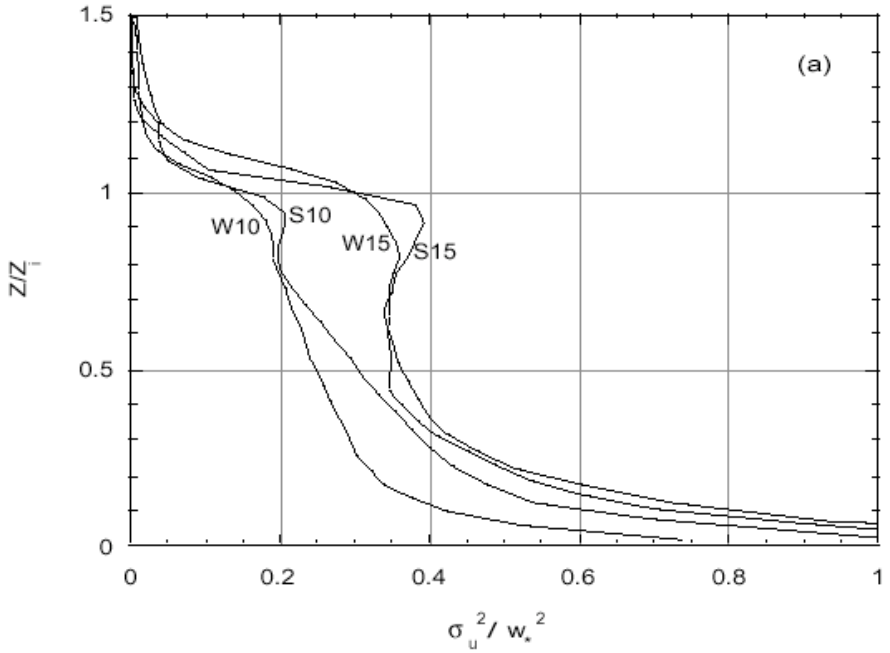

(a)

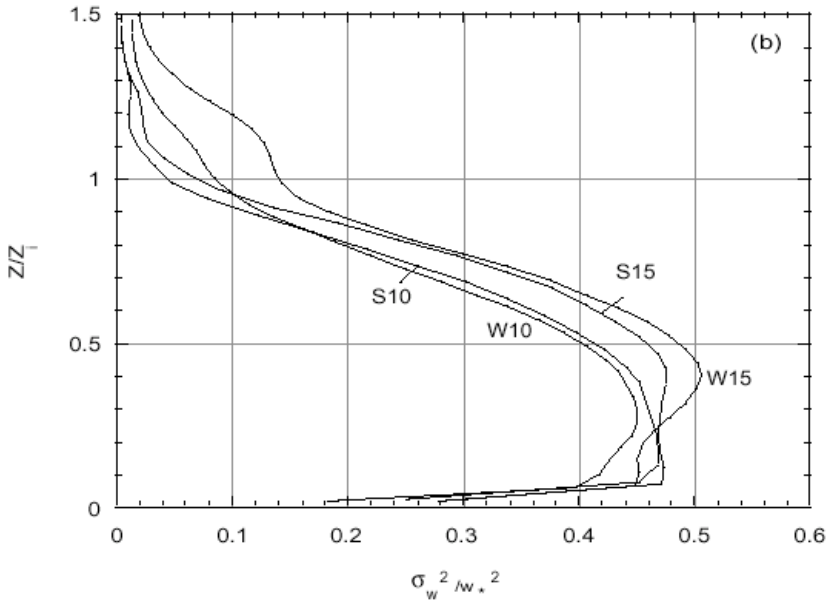

(b)

Figure 13. Vertical horizontal σ_u^2/w_*^2 and vertical σ_w^2/w_*^2 velocity variances, obtained in runs W10, W15, S10, and S15.

Characteristic values of statistical moments at the top of the mixed layer, scaled by the interfacial scales S, are not expected to be constant as in the free-convection case, but should be functions of the interfacial Richardson number (Sorbjan, 2004 a, c):

$$
\begin{aligned}
H_i / (S_w S_\theta) &= - c_H (1 + c_r / Ri) / (1 + 1 / Ri)^{1/2} \\
Q_i / (S_w S_q) &= - c_Q (1 + c_r / Ri) / (1 + 1 / Ri)^{1/2} \\
\sigma_{\theta i}^2 / S_\theta^2 &= c_\theta (1 + c_r / Ri) / (1 + 1 / Ri) \\
\sigma_{qi}^2 / S_q^2 &= c_q (1 + c_r / Ri) / (1 + 1 / Ri) \\
C_{\theta q i} / (S_\theta S_q) &= c_{\theta q} (1 + c_r / Ri) / (1 + 1 / Ri) \\
\sigma_{wi}^2 / S_w^2 &= c_w (1 + c_r / Ri)
\end{aligned}
\qquad (80)
$$

In analogy to (75), statistical moments in the sheared ABL (above the surface layer) can also be represented as a sum of two similarity functions F_m, F_i, and multiplied by similarity scales (1) and (2):

$$M = S_m F_m (z/z_i) + S_i F_i (z/z_i, 1/Ri) \qquad (81)$$

where the function F_i depends in this case on the dimensionless height z/z_i, and also on the interfacial Richardson number Ri. We will assume that $F_i (z/z_i, 1/Ri) = F_1(z/z_i) F_2(1/Ri)$, and $F_2(1/Ri) \to 1$, when $1/Ri \to 0$. As a result, (81) coincides with (75) in the shearless case. Eq. (81) is valid only above the surface layer, since the dependence on z/L is neglected, where $L = -u_*^3/(\kappa\beta H_o)$ is the Monin-Obukhov length, u_* is the friction velocity, and κ is the von Karman constant.

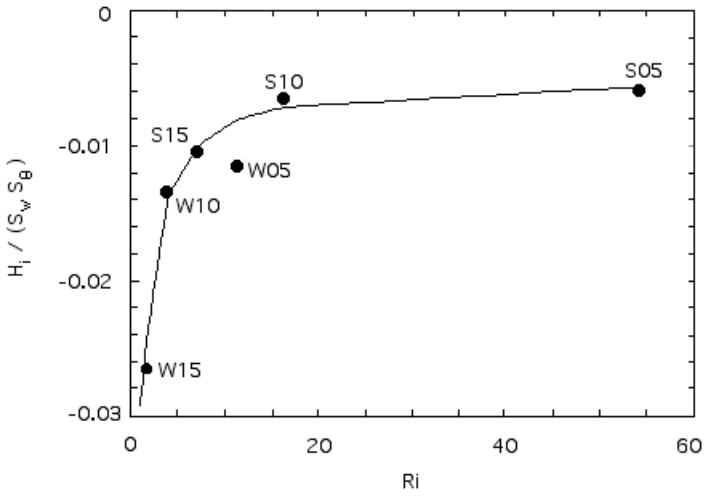

Figure 14. The dimensionless heat flux $H_i/(S_w S_\theta)$ obtained from the LES (dark circles) as a function of the interfacial dynamic Richardson number Ri. Equation 80a is represented by a curve. The LES run names are indicated next to each point.

Figure 14 shows values (points) of the dimensionless entrainment heat flux $H_i/(S_w S_\theta)$, obtained from the LES, as a function of the interfacial dynamic

Richardson number *Ri*. The run names are indicated next to each point. The curve and the points agree quite well. As expected, the negative values of the dimensionless entrainment heat flux increase, when *Ri* decreases, and decrease when *Ri* increases.

Figure 15 depicts the values of the dimensionless vertical velocity variance σ_{wi}^2/S_w^2 at the top of the mixed layer (points), obtained from the LES. In the figure, the estimated dimensionless peak variance, based on Equation 7d, is represented by a curve. The curve and the points agree quite well. The obtained results show that σ_{wi}^2/S_w^2 strongly increases when *Ri* decreases, and decreases when *Ri* increases.

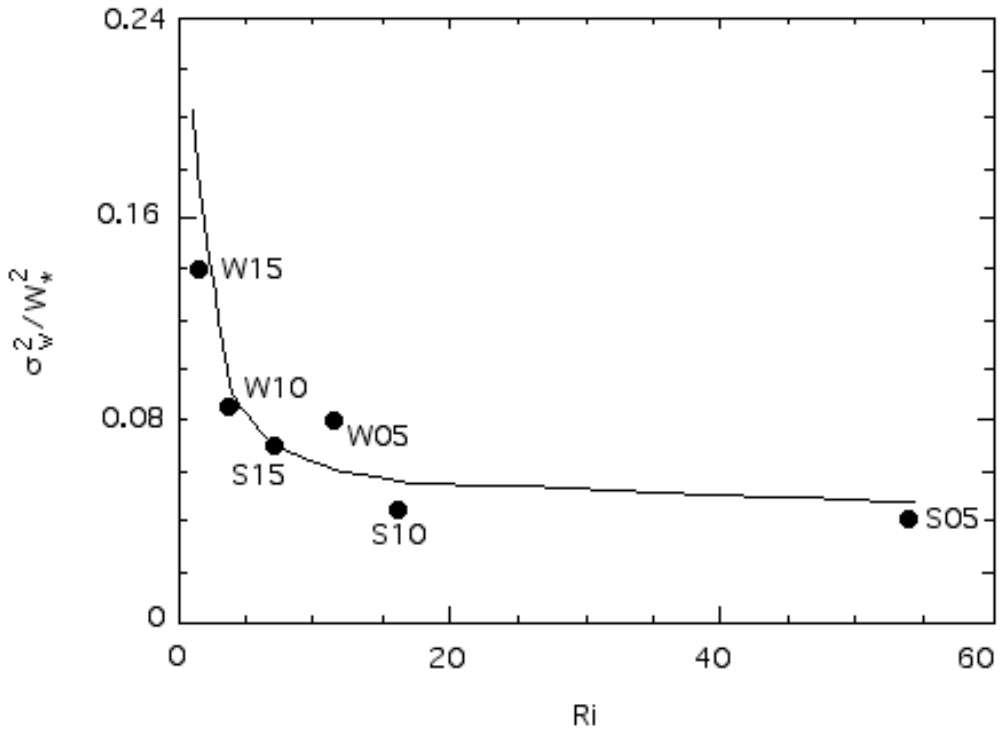

Figure 15. The dimensionless variance σ_{wi}^2/S_w^2 obtained from the LES model (dark circles) as a function of the interfacial dynamic Richardson number Ri. Equation 80a is represented by a curve. The LES run names are indicated next to each point.

Based on (80)-(81), the following expressions could be proposed Sorbjan (2004c):

$$H = w_* \Theta_* \ (1 - z/z_i) - c_H S_w S_\theta \ \frac{(1 + c_{rH}/Ri)}{(1 + 1/Ri)^{0.5}} \ z/z_i$$

$$Q = w_* q_* \ (1 - z/z_i) - c_Q S_w S_q \ \frac{(1 + c_{rQ}/Ri)}{(1 + 1/Ri)^{0.5}} \ z/z_i$$

$$\sigma_\theta^2 = c_1 \ \Theta_*^{\,2} \frac{(1 - z/z_i)}{(z/z_i)^{2/3}} + c_\theta S_\theta^2 \ \frac{(1 + c_r/Ri)}{(1 + 1/Ri)} \ \frac{(z/z_i)^9}{(2.05 - z/z_i)^8}$$

$$\sigma_q^2 = c_2 \; q_*^{\,2} \frac{(1-z/z_i)^8}{(z/z_i)^{2/3}} + c_q S_q^2 \; \frac{(1+c_r/Ri)}{(1+1/Ri)} \left[\frac{(z/z_i)^3}{(2.2-z/z_i)^5} + c_s \right] \quad (82)$$

$$C_{\theta q} = c_3 \; \Theta_* q_* \frac{(1-z/z_i)}{(z/z_i)^{2/3}} + c_{\theta q} S_\theta S_q \; \frac{(1+c_r/Ri)}{(1+1/Ri)} \; \frac{(z/z_i)^8}{(2.2-z/z_i)^8}$$

$$\sigma_w^{\,2} = 1.4\, c_3\, (1\text{-}z/z_i)^{4/3} (z/z_i)^{2/3} + c_w S_w^{\,2} (1+ c_r/Ri)\, (z/z_i)^{1/2}\, (1.1 - z/z_i)^{1/3}$$

and also:

$$\frac{d\Theta}{dz} = -\frac{\Theta_*}{z_i} \; \frac{(1-z/z_i)^4}{(z/z_i)^{4/3}} + \frac{S_\theta}{S_h} \frac{(z/z_i)^9}{(2.23-z/z_i)^9}$$

$$\frac{dq}{dz} = -\frac{q_*}{z_i} \; \frac{(1-z/z_i)^4}{(z/z_i)^{4/3}} + \frac{S_q}{S_h} \frac{(z/z_i)^9}{(2.23-z/z_i)^9} \quad (83)$$

The above expressions are valid for $S_\theta > 0$, below the level, at which a moment has its peak (roughly, $z/z_i < 1.1$). When $1/Ri \rightarrow 0$, the free-convection profiles (77)-(78) are obtained. The constants in (82) should be evaluated based on available atmospheric observations.

3.2 Neutral ABL

By definition, the neutral boundary layer is characterized by a constant with height potential temperature, and a zero turbulent heat flux. The neutral ABL is often referred to as the Ekman layer, after V.V. Ekman, who first solved (in 1905) simplified equations of the atmospheric motion for this case, governed by a balance of the Coriolis, pressure gradient, and friction forces.

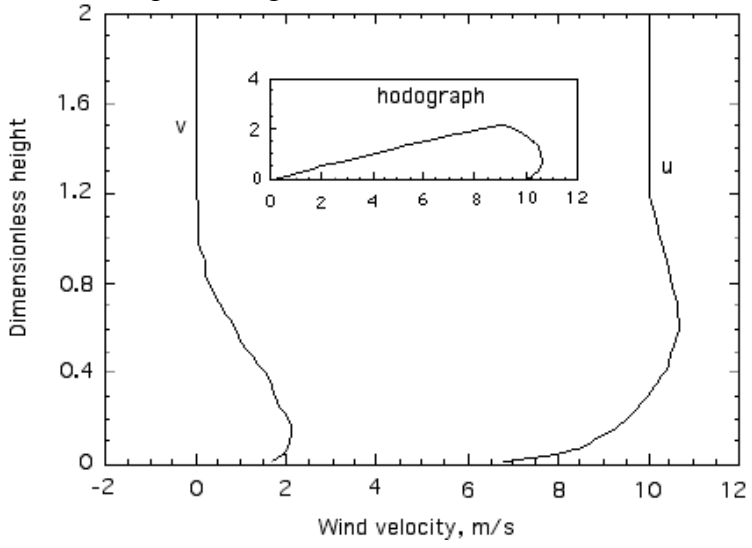

Figure 16. Vertical profiles of wind velocity components u and v from a simulation of a neutral ABL. The wind velocity hodograph is also shown.

In practice, the neutral boundary layer can exist only over marine surfaces, when the ocean surface, and the air flowing above it, have nearly the same temperature. Over land, the neutral ABL is practically absent (note that diurnal transitions do not produce a zero heat flux in the entire ABL, only in the surface layer, and only for a very brief period of time).

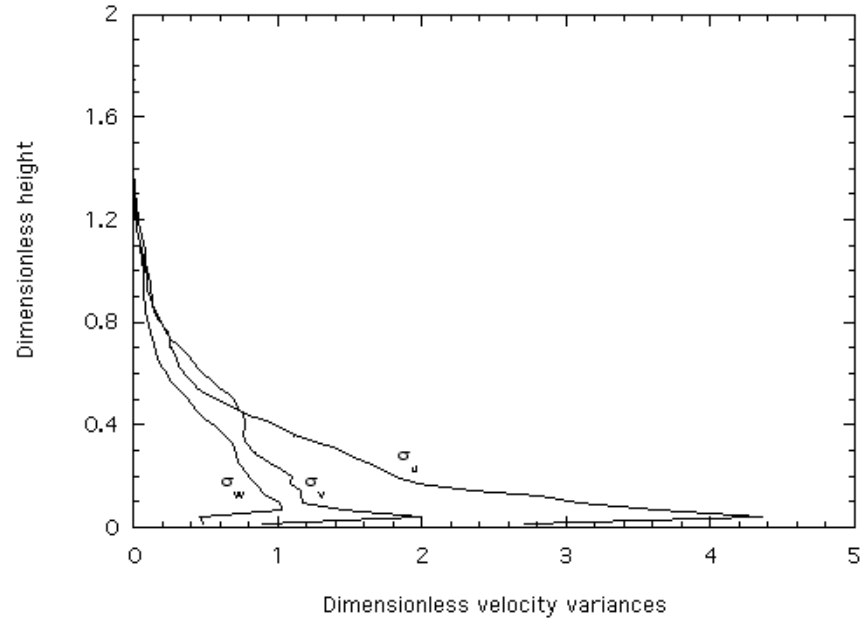

(a)

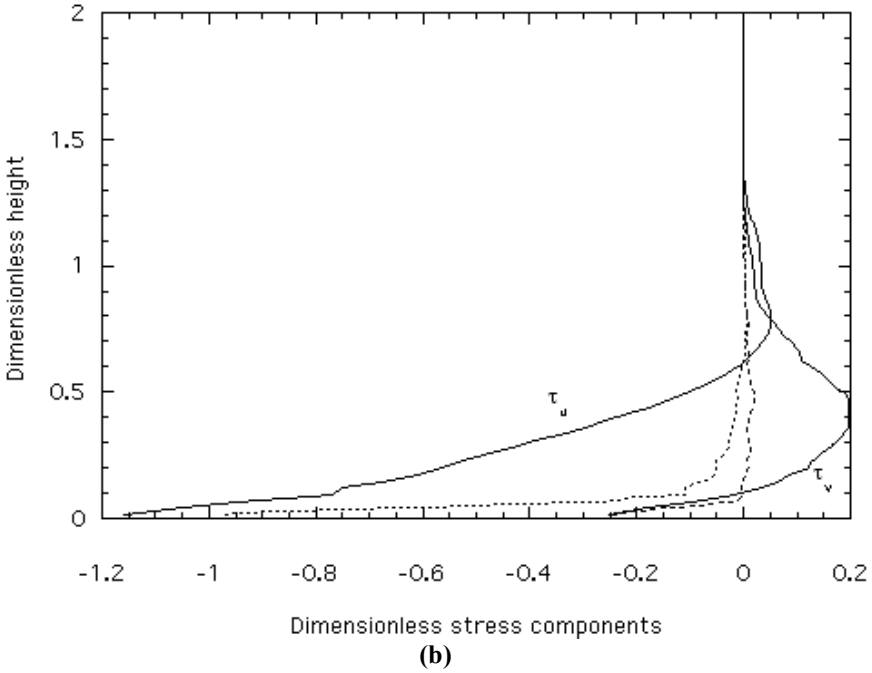

(b)

Figure 17. Vertical profiles from a simulation of a neutral ABL (a) Variances of three components of wind velocity, scaled by u_*^2, (b) components of stress vector (the subgrid fluxes marked by dotted lines).

The physics of the neutral case is not very complex. Turbulence is generated only by wind shear. There is no entrainment, unless the stable interfacial layer is assumed at the top. Numerically, the case requires a relatively long integration time to achieve steady conditions, but the horizontal domain does not need to be substantial. The case has not generated much interest and only a few simulations of the neutral ABL have been simulated (e.g., Mason and Thompson, 1987, Andren et al, 1994).

As an example of the neutral case, let us consider the results of a LES, with a mesh of 16 x 16 x 80 grid points, and the grid increments $\Delta x = \Delta y = 50$ m, and $\Delta z = 40$ m. The simulation was performed for 135,118.8 s (i.e., 25,000 time steps), with the geostrophic wind $G = 10$ m/s, the Coriolis parameter $f = 0.0001$ s^{-1}, and the roughness parameter $z_o = 0.01$ m. The potential temperature was assumed constant in the entire domain. Therefore, there was no entrainment generated by wind. The resulting friction velocity was $u_* = \sqrt{\tau_o / \rho} = 0.3708$ m s^{-1} (where τ_o is the surface stress, and ρ the air density. The Ekman height scale $L_E = \kappa\, u_*/f = 2832$ m (where κ is the von Karman constant). The results of the simulation are depicted in Figures 16 and 17. The vertical axes in the figures are scaled by L_E.

Figure 16 shows the vertical profiles of the wind components, as well as the resulting wind hodograph. The cross-isobar angle of about 30° is obtained. The velocity variances, depicted in Figure 17a, decrease with height. Figure 17b presents the total and subgrid contributions to the stress vector components.

3.3 Stable ABL

The stable ABL is usually observed at night over land, or over cold marine surfaces, when the heat flux is negative, and turbulence is generated mainly by wind shear. The stable case is difficult to simulate, because the grid spacing must be small (a few meters), and the simulation time long. Stronger cooling rates at the surface require a higher grid resolution. If a grid spacing is too coarse, a simulation can produce a spurious laminarization of the flow. There have been only a few reported stable ABL simulations (e.g., Mason and Derbyshire, 1990, Brown et al., 1994, Andren, 1996, Galmarini et al., 1998, Kosovich and Curry, 2000, Saiki et al, 2000, Beare et al, 2004, Beare and MacVean, 2004).

In stable conditions, turbulence is local and suppressed by stratification effects. Based on this premise, Nieuwstadt (1984) introduced the local similarity scaling in this case:

$$U_*(z) = \left[\tau(z)/\rho\right]^{1/2} \qquad \text{for velocity}$$

$$\vartheta_*(z) = -\frac{H(z)}{U_*(z)} \qquad \text{for temperature} \qquad (84)$$

$$\Lambda_*(z) = -\frac{U_*^2(z)}{\kappa\,\beta\,\vartheta_*(z)} \qquad \text{for height}$$

where $H(z)$, and $\tau(z)/\rho$ are turbulent fluxes of heat and momentum. The above scales are analogous to the Monin-Obukhov scaling in the surface layer. As in the surface layer, it could be expected that statistical moments non-dimensionalized by local scales are constant (e.g., Sorbjan, 1986).

For z/h < 1 it can be assumed that $\tau/\rho(z) = u_*^2(1 - z/h)^{\alpha 1}$, and $H(z) = H_o\,(1 - z/h)^{\alpha 2}$, where h is the depth of the stable layer, u_* is the friction velocity, H_o is the surface value of the heat flux, and α_1 , α_2 are empirical parameters, which are case (radiative conditions) dependent. Once they are determined, all turbulent statistics of the flow may be predicted, assuming their proportionality to the local scales. For example, during the 1973 Minnesota experiment, it was found that $\alpha_1 = 2$ and $\alpha_2 = 3$ (Sorbjan, 1986). Nieuwstadt (1984) found $\alpha_1 = 3/2$ and $\alpha_2 = 1$ based on data collected from the Cobauw tower. Note that $\alpha_2 = 1$ indicates quazi-stationary conditions with uniformly constant cooling of the ABL.

As an example of a stable ABL simulation, let us consider a run with a mesh of 64 x 64 x 64 points and with grid increments $\Delta x = \Delta y = \Delta z = 6$ m. The initial potential temperature was equal to 265 K in the first 100-m layer, and decreases by 1K/100 m above it. The surface cooling, assumed as 0.25K/h, was applied for 9 hours. The geostrophic wind was G = 8 m/s, the Coriolis parameter f = 1.39 x 10^{-4} s^{-1}, and the roughness parameter $z_o = 0.1$ m. The resulting friction velocity is $u_* = 0.29$ m/s. The described setup is similar to the case, considered by Beare et al. (2004). The LES results, obtained after 1-hour averaging, are presented in Figures 18-21.

Figure 18 displays the profile of the potential temperature. During the simulation, the surface temperature decreases by about 2 degrees. This cooling rate decreases with height, and is nil at the level of about 250 m. As expected, the temperature profile has a negative curvature, except near the underlying surface and at the top the boundary layer.

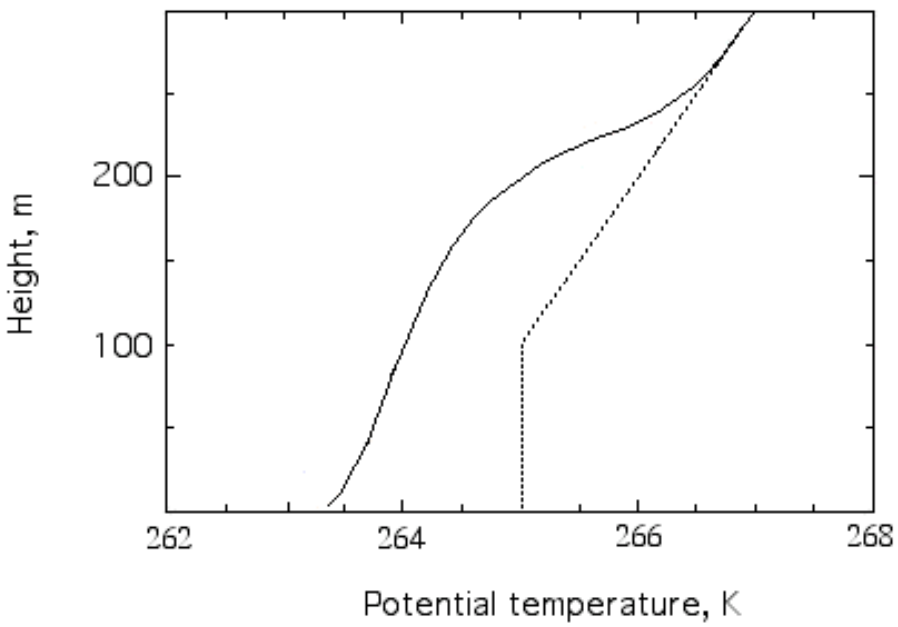

Figure 18. The initial (dotted line) and final profiles of the potential temperature obtained from a LES of a stable ABL.

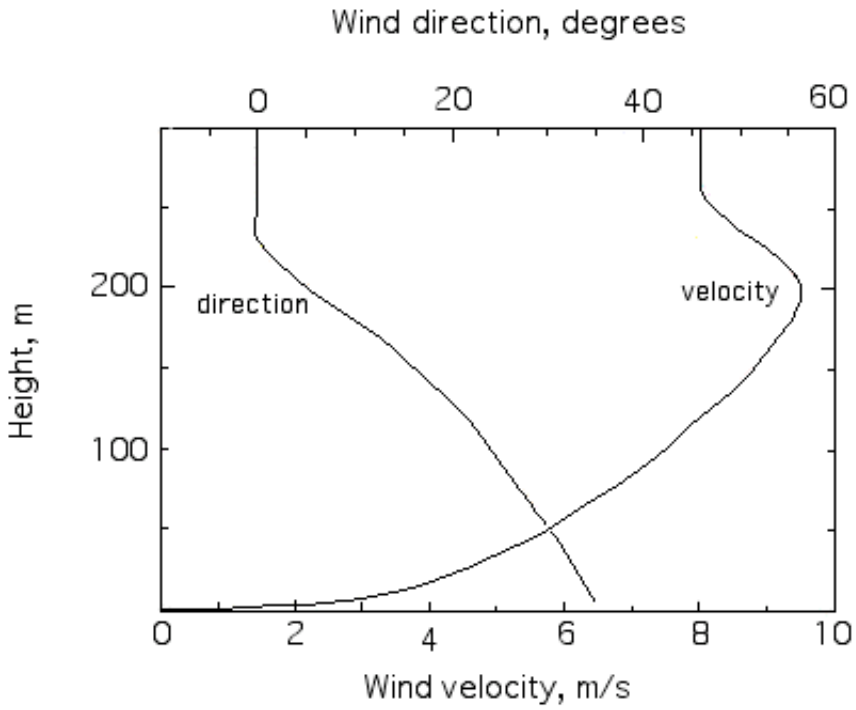

Figure 19. Vertical profiles of wind velocity and direction obtained from a LES simulation of a stable ABL.

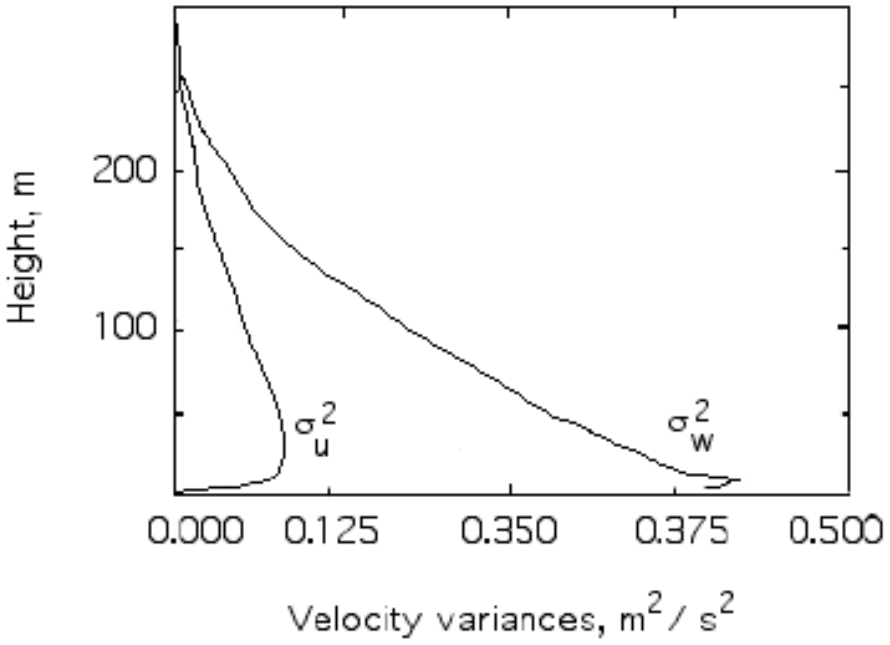

Figure 20. Vertical profiles of the velocity variances obtained from a simulation of a stable ABL.

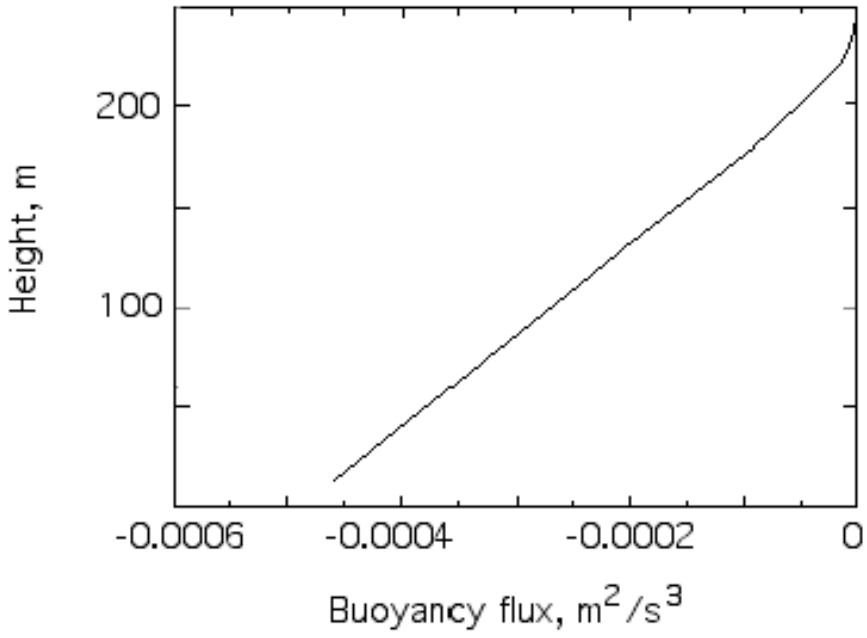

(a)

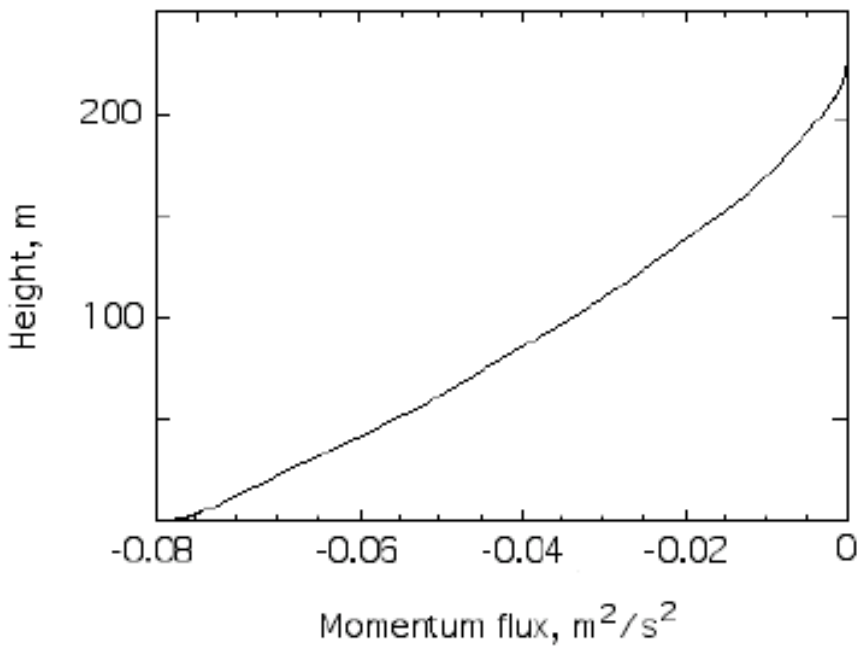

(b)

Figure 21. Vertical profiles of buoyancy and momentum fluxes obtained from a simulation of a stable ABL

The convex (i.e., $\partial^2\Theta/\partial z^2 < 0$) curvature is caused by turbulent cooling ($\partial\Theta/\partial t < 0$). Note that turbulent warming (morning transition) causes the potential temperature curvature near the surface to be positive (concave, since $\partial\Theta/\partial t$ and $\partial^2\Theta/\partial z^2 > 0$). Any departure from such profiles can be an indication of radiative and/or advective cooling or warming, or of a lack of continuous turbulence.

Vertical profiles of the wind velocity and the wind direction are shown in Figure 19. A super-geostrophic wind of about 9.5 m/s is present near the top of the ABL. It can be identified as "low-level jet-stream" – a typical phenomenon in stable conditions. The cross-isobar angle is about 40°.

The velocity variances are depicted in Figure 20. They decrease with height and arrive at zero values at about z = 250 m. A nearly linear profile of the heat flux in Figure 21a indicates that quazi-stationary conditions have been reached, with uniformly constant cooling of the ABL. The stress in Figure 21b can be described by $\alpha_1 = 3/2$.

3.4 Cloud-Topped ABL

Cloudiness is the most characteristic feature of the Earth, when viewed from space. Satellite photographs often show intriguing cloudy patterns, which can be qualified as hexagonal cells with vertical axes, opened (no clouds in the center of each cell, only at the edges), or closed (clouds in the center of each cell, openings

at the edges), with diameters from a few to tens of kilometers (Figure 22), and also opened or closed horizontal roll vortices, with horizontal axes (Figure 1). Agee (1987) identified six types of the ABL events, which occur over both oceanic and continental surfaces. The specified types include "cold-air out-breaks", controlled by surface heating and moistening, "cloud-topped boundary layers", driven by radiative cooling and warming, as well as "continental circulations", affected by surface sensible and latent heat fluxes. The boundary layer clouds include stratus, stratocumulus, and shallow cumulus. By definition, their lifting condensation level is below the top of the mixed layer.

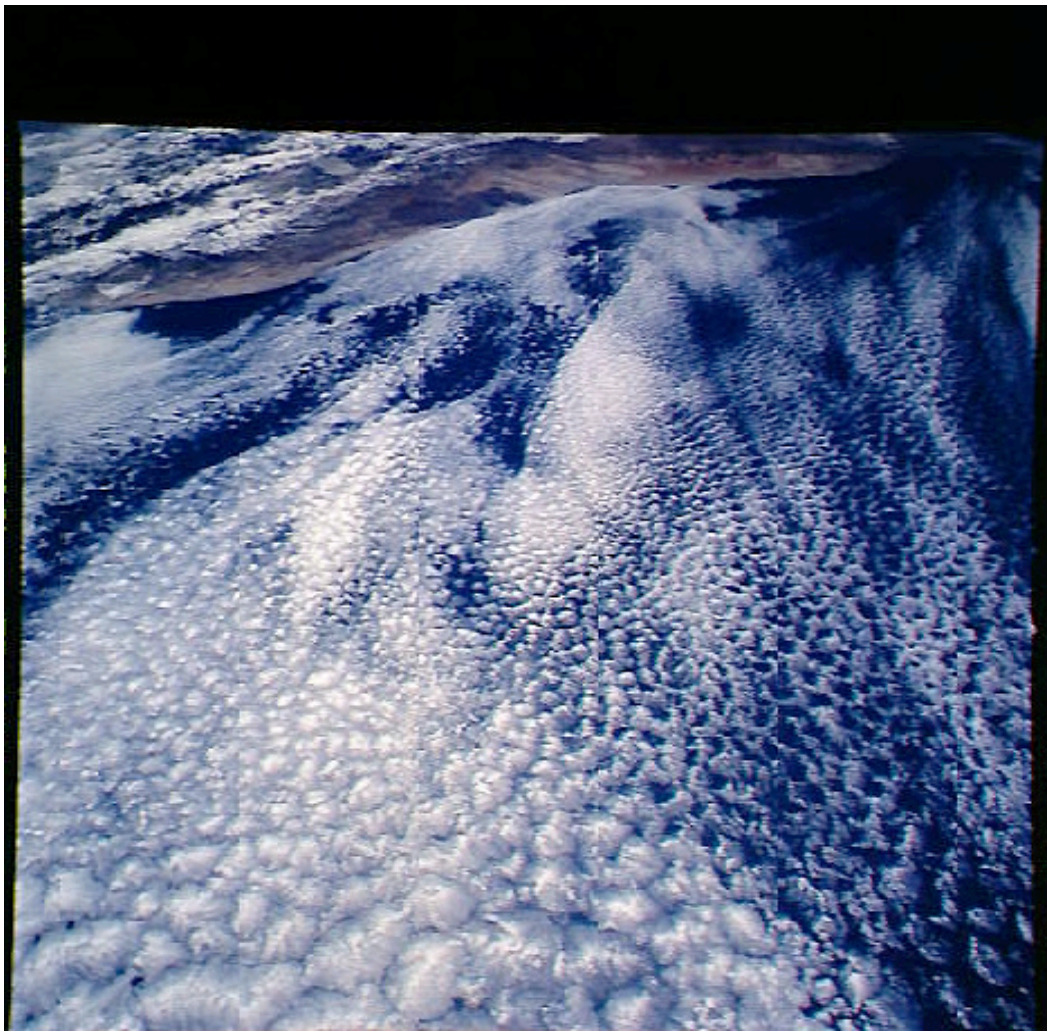

Figure 22. Convective cells with vertical axes: opened (no clouds in the center of each cell, only at the edges), and closed (clouds in the center of each cell, openings at the edges), viewed from a space shuttle (NASA).

Stratus and stratocumulus can collectively be called "stratiform clouds". They have some common microphysical characteristics, and formation mechanisms. A

favorable condition for their occurrence is a large-scale subsidence. Due to radiative and evaporative cooling, the depth of the capping interfacial layer is very thin, and the temperature jump in this layer is quite large**.** Fractional cloudiness of stratus and stratocumulus clouds is about 100%. The stratiform clouds form over both, continental and marine locations.

Cumulus clouds are formed by the local ascent of humid buoyant air parcels. They are frequently referred to as fair-weather cumulus, cumulus humilis, or non-precipitating cumulus clouds, and occur over all regions of lands, and ice-free global ocean, with high frequency in the tropics. Their fractional cloudiness reaches up to about 30%. Cumulus convection intensifies the vertical transport of heat, moisture, and momentum, and deepens the ABL. Cumuli clouds are important in the venting of air pollutants.

Examples of large-eddy simulations with stratiform and cumuliform clouds are presented below.

3.4.1 Stratiform-Clouds Topped ABL

Stratus and stratocumulus clouds have a strong impact on the dynamics of the ABL. Their presence introduces additional buoyancy sources and sinks, which are absent in the previously discussed convection cases. As a result, the cloud-topped ABL is more difficult to simulate than its cloud-free counterpart.

Physical processes in a cloud-topped boundary layer are schematically depicted in Figure 23. The sketch in the figure reminds a medieval clock, whose mechanism is propelled by a gravity force (such a 13th century clock is still operational in a cathedral church in Gdansk, Poland). The operation of the cloud-topped ABL is "somewhat" similar.

The main factor which drives downward motion and turbulence within the stratiform-topped ABL is longwave radiatiative cooling at the cloud top. Turbulence generates entrainment. Entrainment brings warm inversion air into the cloud. The warm air mixes with radiatively cooled cloud air. The mixed air is less heavy, which reduces the efficiency of radiative cooling in driving turbulence. Weaker turbulence reduces entrainment (negative feedback).

On the other hand, entrainment brings warm and dry air, which causes the mixed air to be unsaturated. The resulting evaporative cooling enhances turbulence and produces stronger entrainment (positive feedback). The evaporative cooling may lead to an instability process, in which parcels cool even more, sink, and break up a solid cloud deck.

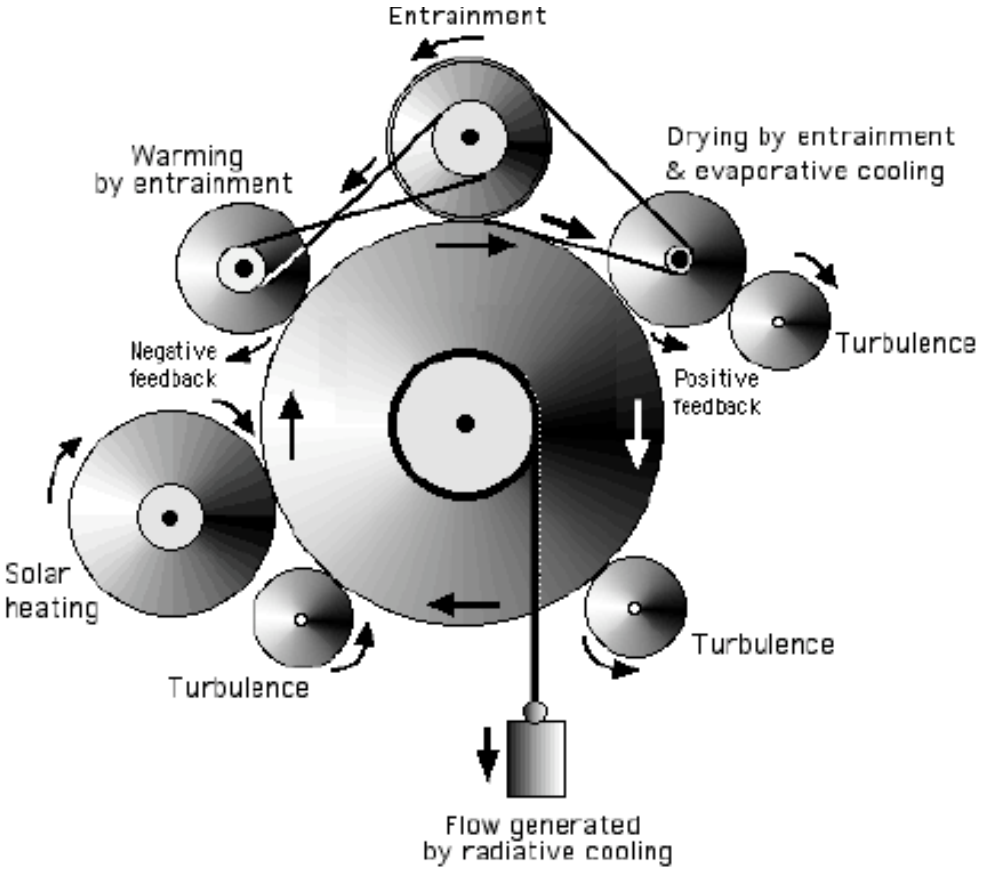

Figure 23. Schematic of turbulence generation within a stratocumuli cloud.

Influence of solar radiation comes from the solar absorption inside the cloud layer. Solar heating is more uniformly distributed through the layer (see Figure 2). Near the cloud top, the solar heating can offset radiative cooling in generating turbulence. Inside the cloud, the solar heating can "burn" it. Together, these two effects can control a diurnal cycle of marine stratocumulus clouds, even though the ocean surface temperature remains the same. Thus, the clouds thin (or disappear) in the daytime, and thicken at night.

When the whole cloud layer is warmed by solar heating, the cloud layer may become warmer than the subcloud layer. The resulting formation of a thin stably stratified layer at the cloud base can "decouple" the cloud layer from the underlying surface, and cutoff the moisture supply from the surface into the cloud layer. In addition, cooling introduced by the evaporation of drizzle can cool the sub-cloud layer, and consequently further stabilize the interface between the cloud and its sub-cloud layer. This leads to a rapid thinning of the cloud layer during the daytime, and also has an important influence on the radiative balance at the Earth's surface.

A multilayer structure of the cloud-topped ABL causes universal scaling not to exist for this case. However, the use of some form of mixed layer scaling can be at least partly successful (e.g., Nichols, 1989). The mixed layer scales are of the form:

$$W_* = (\beta B_v z_c)^{1/3} \qquad \text{for vertical velocity}$$

$$T_{v*} = \frac{B_v}{W_*} \qquad \text{for temperature} \qquad (85)$$

$$q_{T*} = \frac{Q_T}{W_*} \qquad \text{for total water specific humidity}$$

where $B_v = 2.5 / z_c \int_0^{z_c} H_v(z)\, dz$, Q_T is the total water specific humidity flux at the earth's surface z_c is the top of the cloud layer, and β is the buoyancy parameter. Note that the above scales coincide with (72) in the cloud-free case (when $H_i/H_o = -0.2$ is assumed).

In order to further discuss the cloud-topped case, let us consider the results of a LES, with a mesh of 32 x 32 x 60 grid points, and the grid increments $\Delta x = \Delta y =$ 60 m, and $\Delta z = 30$ m (a quite coarse resolution!). The simulation was performed for 15,136.7 s (i.e., 1200 total time steps) in shearless conditions. The initial mixed layer was 700 m deep, with a uniform potential temperature of 280 K. The interfacial layer was initially 100 m deep. The initial temperature gradient γ_i in the interfacial layer was equal to 0.06 K m^{-1}. In the free-atmosphere, the temperature gradient was $\Gamma = 0.004$ K m^{-1}. The surface turbulent heat flux H_o was assumed to be nil. The surface humidity flux Q_o was 0.00001. The results of the simulation are presented in Figures 24-29.

Figure 24a shows the vertical profiles of the liquid water potential temperature Θ_L and the virtual potential temperature Θ_v. The specific humidity profiles, q_v, q_L, and q_T, are depicted in Figure 24b. The liquid water potential temperature Θ_L, and the total specific humidity q_T are conserved in a moist adiabatic process. Therefore, these quantities are well-mixed within the ABL. The virtual potential temperature Θ_v is not well mixed. The initial profiles of temperature and humidity are also shown in the figures. The liquid water potential temperature slightly decreases with time, as a result of radiative cooling. The total mixing ratio slightly decreases with time due to the growth of the mixed layer.

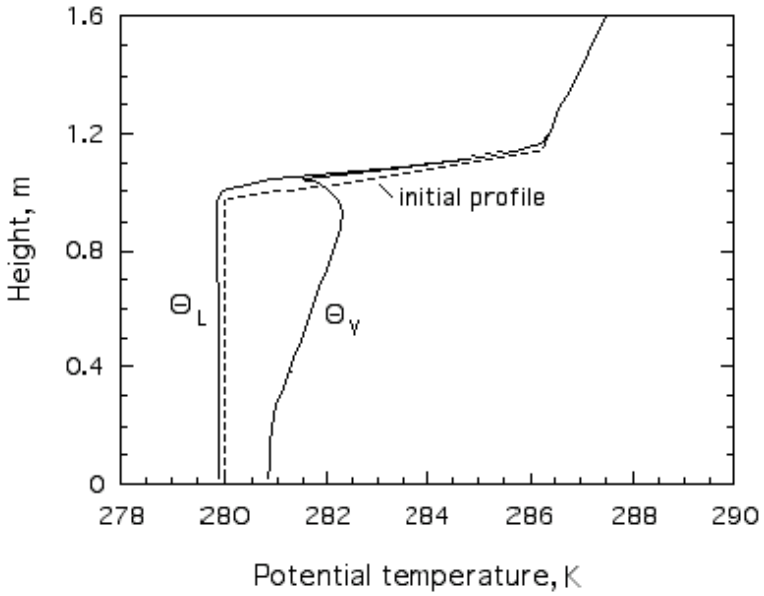

(a)

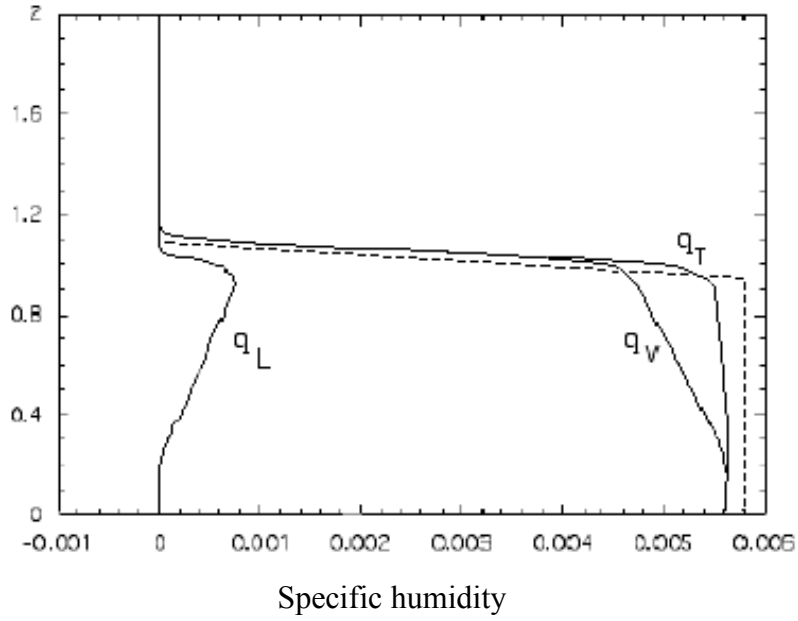

(b)

Figure 24. Vertical profiles of: (a) liquid water potential temperature Θ_L, virtual potential temperature Θ_V, (b) specific humidity q_v, liquid water specific humidity q_L, and total water specific humidity q_T, obtained in a simulation of a stratocumulus-topped ABL. Initial temperature and humidity profiles are marked by dotted lines.

The vertical profiles of the liquid water potential temperature flux H_L, the radiative flux F, and their sum $R = H_L + F$ are depicted in Figure 25. Note that integrating the equation for the horizontally averaged liquid water potential temperature $\partial\Theta_L/\partial t = -\partial R/\partial z$, yields:

$$R(z) = R(0) - \int_0^z \frac{\partial Q_L}{\partial t} dz \tag{86}$$

As mentioned above, $\partial\Theta_L/\partial t = const < 0$ in the initial mixed layer. As a result, the flux R in Figure 25 is approximately a linear and increasing function of height. Near the top of the mixed layer, $\partial\Theta_L/\partial t < 0$, and R increases non-linearly, until it reaches its value R_i at the top of the cloud layer. The resulting turbulent heat flux H_L is the difference between the total flux R and the radiative flux F. In the lower part of the mixed layer, $F = 0$, and $H_L = R$. At the top of the cloud layer, H_L rapidly decreases with height, and reaches its negative minimum.

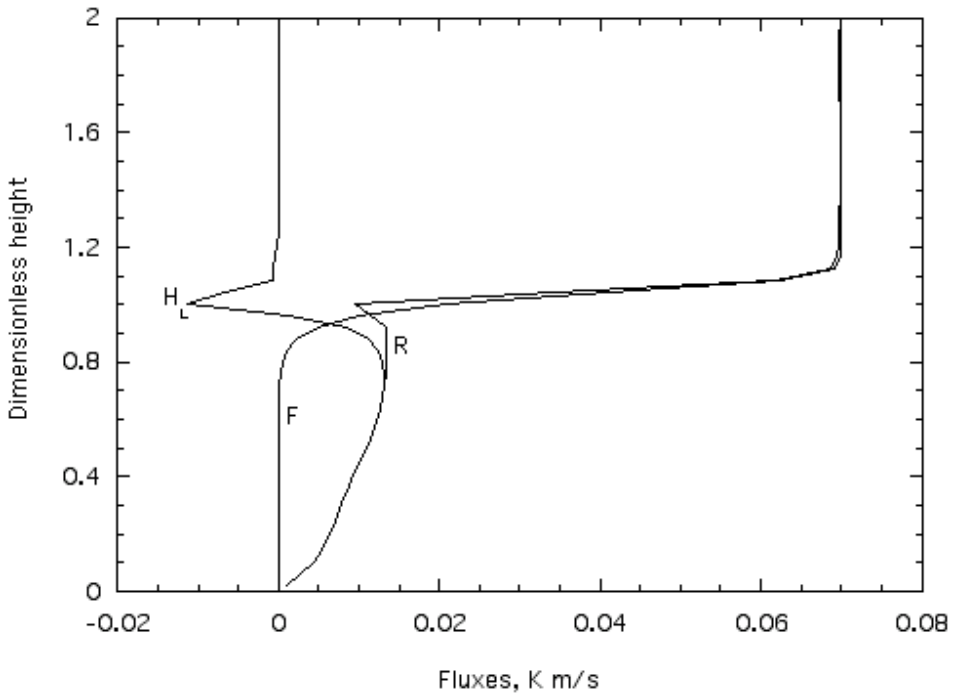

Figure 25. Liquid water potential temperature flux H_L, net radiative flux F, and their sum $R = H_L + F$, obtained in a simulation of a stratocumulus-topped ABL.

Analogous arguments can be applied to the total water specific humidity flux in Figure 26. Its equation: $\partial q_T/\partial t = -\partial Q_T/\partial z$ indicates that because $\partial q_T/\partial t < 0$, then the turbulent flux $Q(z)$ is an increasing function of height in the mixed layer. Above the mixed layer, $\partial q_T/\partial t > 0$, and the turbulent flux Q(z) decreases to zero.

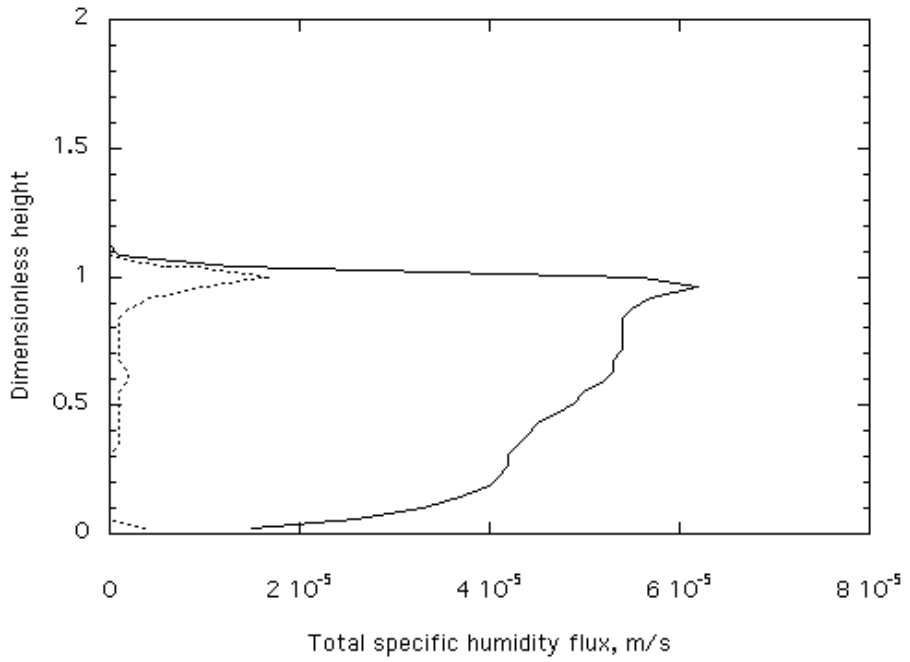

Figure 26. Total water specific humidity flux, obtained in a simulation of a stratocumulus-topped ABL. The subgrid flux is indicated by the dotted line.

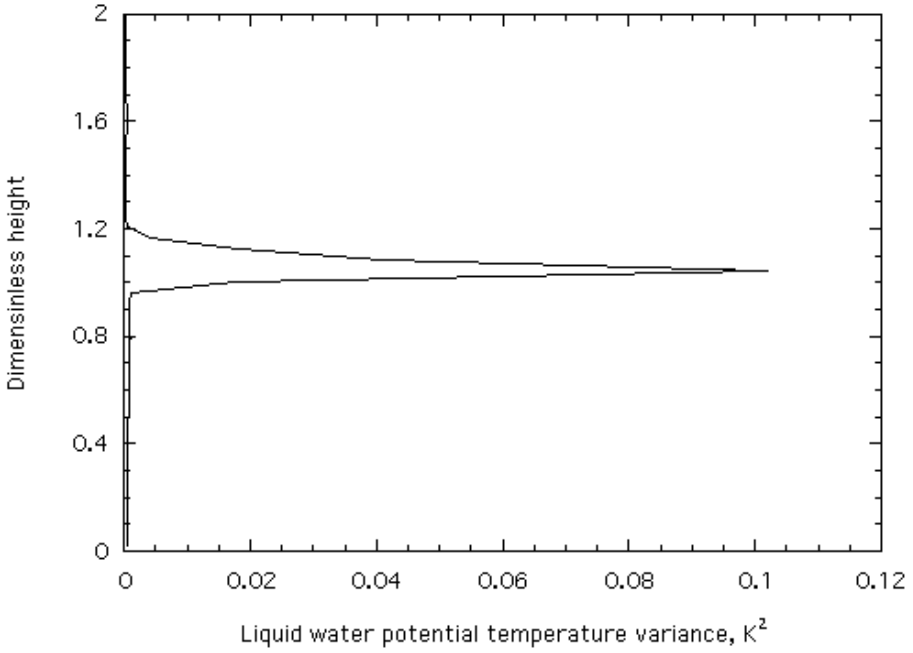

Figure 27. Variance of the liquid water potential temperature from LES of a stratocumulus-topped ABL.

The vertical profile of the liquid water potential temperature variance $\sigma_{\theta L}{}^2$ is shown in Figure 27. The variance is nearly zero in the mixed layer and in the free

atmosphere. At the top of the cloud layer the variances has a sharp peak. The total water specific humidity variance σ_{qT}^2 (not shown) has a very similar profile.

Profiles of the velocity variances are presented in Figure 28. Their vertical distribution is somewhat similar to the free-convective case in Figure 8, even though the mechanisms triggering convection in both cases are different. As mentioned before, in the free-convection case, convection is generated by the heating of the underlying surface, while in the cloud-capped case, it is generated by radiative cooling. The horizontal variances σ_u^2 and σ_v^2 in Figure 28 sharply decrease with height in the surface layer, and are nearly constant in the mixed layer. The vertical velocity variance σ_w^2 has a maximum in the mixed layer. The maximum is located higher than in the clear-sky case in Figure 8.

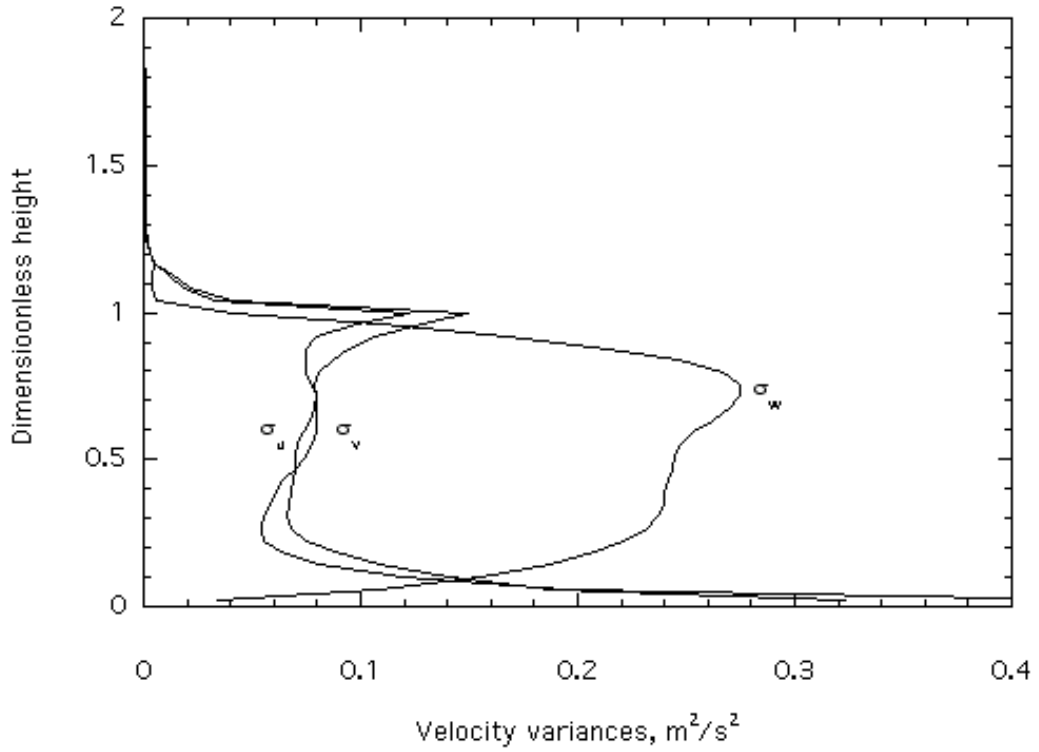

Figure 28. Vertical profiles of the velocity variances from a simulation of a stratocumulus-topped ABL.

The vertical velocity skewness S_w is shown in Figure 29. The values of S_w are negative near the surface, and positive in the cloud layer. The negative skewness below the cloud base is due to stronger narrow downdrafts surrounded by larger areas of weaker updrafts. On the other hand, a positive skewness in the cloud layer indicates stronger narrow updrafts surrounded by larger areas of weaker downdrafts. It also implies that downdrafts cover more than half the area of the horizontal plane.

Further analysis indicates that in the lower part of the cloud layer and in the sub-cloud layer, the liquid water potential temperature Θ_L in updrafts is slightly higher than in the vicinity. On the other hand, Θ_L in downdrafts is slightly lower. This picture is different at the top of the cloud layer, where turbulence generates entrainment. Entrainment brings warm and dry inversion air into the cloud. This air mixes with radiatively cooled cloud air. As a result, Θ_L in the sinking air is slightly higher than its vicinity, and the rising air is slightly lower.

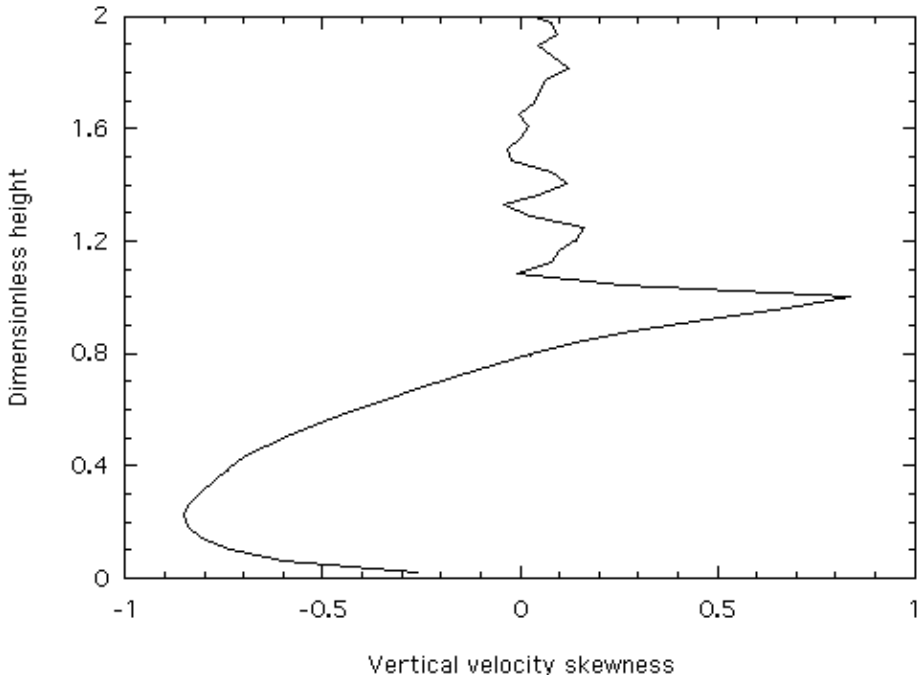

Figure 29. The vertical velocity skewness from a simulation of a stratocumulus-topped ABL.

3.4.2 Cumulus-Topped ABL

The structure of the cumulus-capped convective boundary layer is controlled by various processes, including subsidence, latent heat, radiative cooling, temperature advection, and surface warming. Due to subsidence warm and dry air is being brought down in the free atmosphere. By entrainment of this air, the ABL gets warmer and drier. Advective cooling and moistening intensifies this process. The drying causes evaporation and upward flux of moisture from the surface. The latent heat, released during the formation of clouds, enhances the buoyancy of updrafts and the production of turbulence in clouds. Presence of clouds modifies the radiatiative fluxes.

The cumulus convection often takes on the form of open cells and rolls. The cell patterns are clearly visible in Figure 1. The roll structures can be seen in Figure 30 as cloud streets. As mentioned in Section 3.1, wind shear is the main factor

responsible for the appearance of these coherent structures in convective conditions. Animations of the cumulus-topped ABL can be found at the web site: http://www.knmi.nl/~siebesma/gcss/animations/3D.html.

Let us consider the results of two cumulus simulations. The first simulation was performed under windless conditions, and hereafter will be referred to as F – free convection. The second one characterizes convection with the presence of wind, and hereafter will be referred to as S – sheared convection. In both simulations, a mesh of 32 x 32 x 75 grid points was employed. The grid increments were $\Delta x = \Delta y = 50$ m, $\Delta z = 40$ m in the first run, and $\Delta x = \Delta y = 100$ m, $\Delta z = 40$ m in the second one.

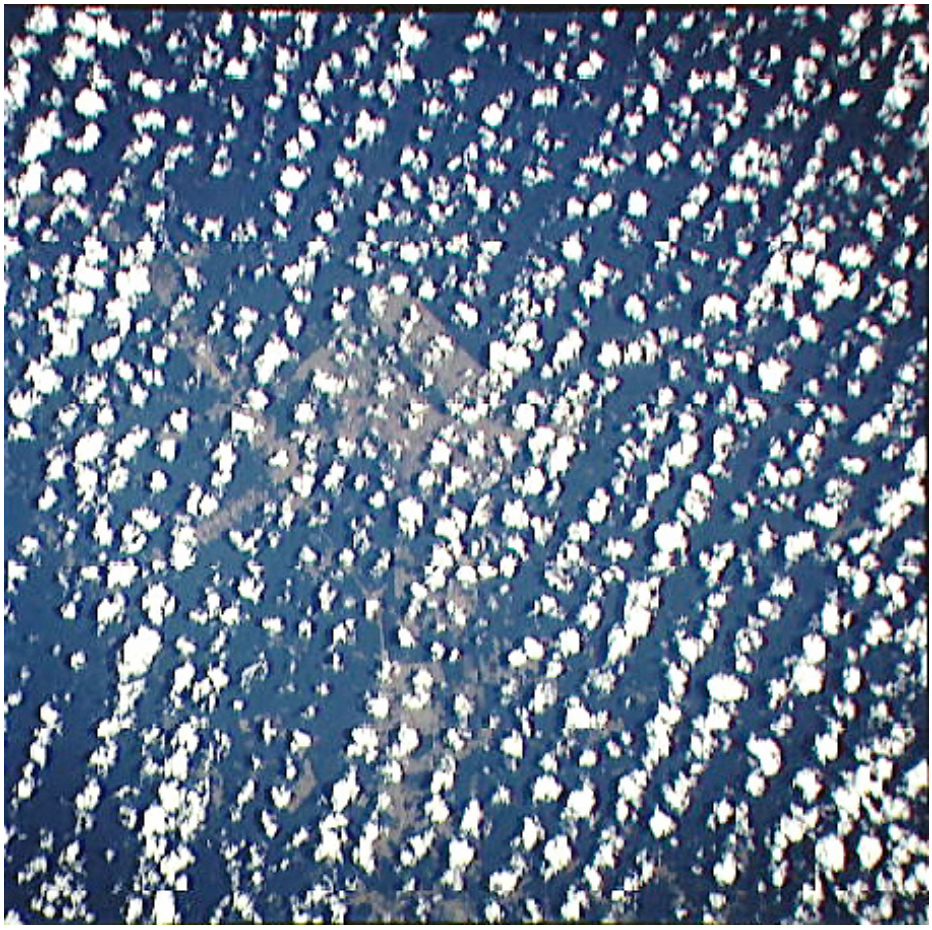

Figure 30. Convective rolls marked by cumulus clouds (NASA).

The initial mixed layer was 520 m deep, with a uniform potential temperature of 298.5 K. Initially, no clouds were present. Therefore, the initial liquid water potential temperature and the potential temperature were equal. Above the mixed layer, the temperature gradient was 3.85 K/km up to 1480 m, then 11.15 K/km up to 2000 m, and 3.65 K/km above. Initially, the specific humidity at the surface

was 0.017. It decreased with height to 0.0163 at the level of 520 m, again to 0.0107 at 1480 m, then went further down to 0.0042 at 2000 m. Finally, it decreased to zero at the top of the vertical domain.

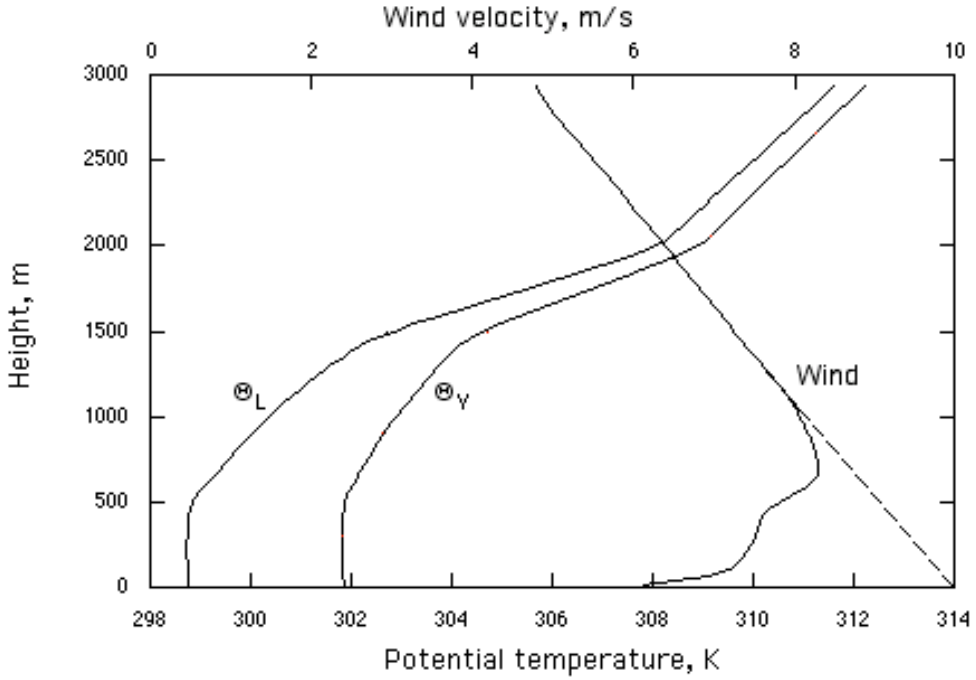

Figure 31. Vertical profiles of the liquid water potential temperature Θ_L, the virtual potential temperature Θ_v, and the wind velocity (in run S), obtained from large-eddy simulations of shearless and sheared cumulus convection. Note that the same temperature profiles were obtained in both simulations. The geostrophic wind is marked by a dotted line.

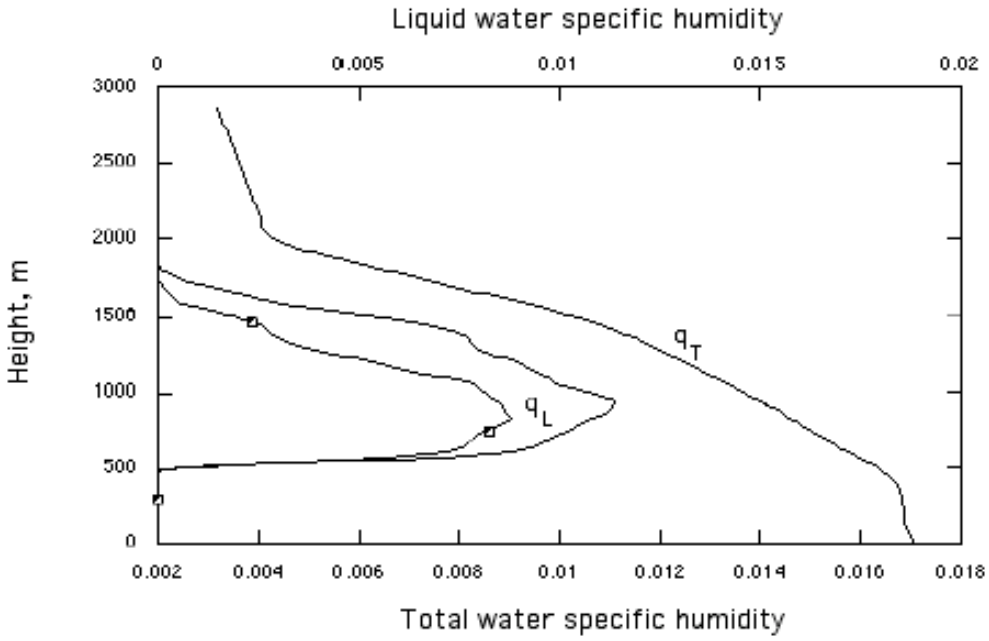

Figure 32. Vertical profiles of the total water specific humidity q_T (the same in both runs), the liquid water specific humidity q_L, obtained from large-eddy simulations of shearless and sheared (marked by squares) cumulus convection.

The LES was initialized assuming the surface heat flux H_o equal to 0.008 K m s^{-1}, and the humidity flux Q_o = 0.000052. In run S, the geostrophic wind was -10 m/s at the surface, and its u-component increased linearly with height by a rate of 0.0018 s^{-1} (negative shear case, Sorbjan 2004 a). The roughness parameter was z_o = 0.012 m, the Coriolis parameter f = 0.0000376 s^{-1}. The absorber at the top of the domain was 10 grid points deep, and the relaxation constant r_o = 0.01 s^{-1}.

A large-scale subsidence (applied to q_T, Θ_L, u, and v) was assumed to decrease linearly with height from zero at the surface to -0.0065 m/s at z =1500 m, and then linearly decrease to zero at 2100 m. The prescribed radiative cooling was -2.315 x10^{-5} K/s below 1500 m, and then it decreased linearly to zero at z = 2500 m, and remained zero above. The advective drying of q_T was -1.2 x10^{-8} s^{-1} in the first 300 m above the surface, it decreased to zero at 500 m, and stayed nil above. The simulation time was 21,608 s in run F, and 22,591 s in run S (i.e., 3000 total time steps). Statistics were obtained during the last 1000 time steps. The described setup is similar to the BOMEX case, considered by Siebesma et al (2002).

The resulting profiles of temperature in both cases, and wind velocity in run S, are shown in Figure 31. The simulation conditions were defined in such a way that the radiative cooling approximately balanced the vertical gradient of the heat flux. As a result, the potential temperature does not change much during both simulations. The virtual potential temperature in the mixed layer is larger then the potential temperature, due to the presence of water vapor. There is clearly a two-layer structure of convection in both presented cases. The lower layer (mixed layer) is governed by the surface heat flux generated convection. The temperature and wind velocity profiles in the mixed layer are similar to those described in Section 3.1. The mixed layer values are nearly constant with height, and sharply increase above 500 m.

Vertical profiles of the total water specific humidity q_T, and the liquid water specific humidity q_L are shown in Figure 32. The initial conditions were defined in such a way that the advective drying approximately balanced the moistening by the surface flux. Consequently, the total water specific humidity changes little during the simulations. The cloud layer is defined by the liquid water specific humidity, and is confined approximately between 500 m and 1750 m. The total water specific humidity q_T is nearly constant with height in the mixed layer, and sharply decreases above 500 m.

Profiles of the buoyancy flux βH_v, and the liquid water potential temperature flux H_L are depicted in Figures 33a, b. The buoyancy flux in Figures 33a decreases linearly up to the cloud base, where it reaches a negative peak of about 20% of the

surface flux. This indicates that the entrainment processes in the subcloud mixed layer are similar to those described in Section 3.1. In the cloud layer, there is a positive buoyancy flux due to positive buoyant updrafts in the cloud layer.

The liquid water potential temperature flux H_L in Figure 33b linearly decreases to a minimum value in the cloud layer. Above this level, H_L rapidly decreases to zero.

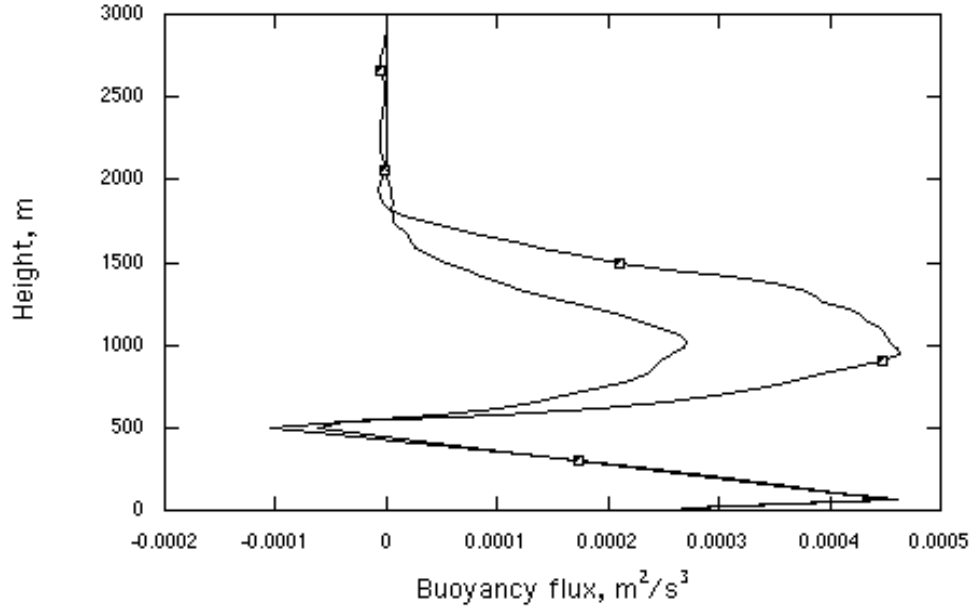

(a)

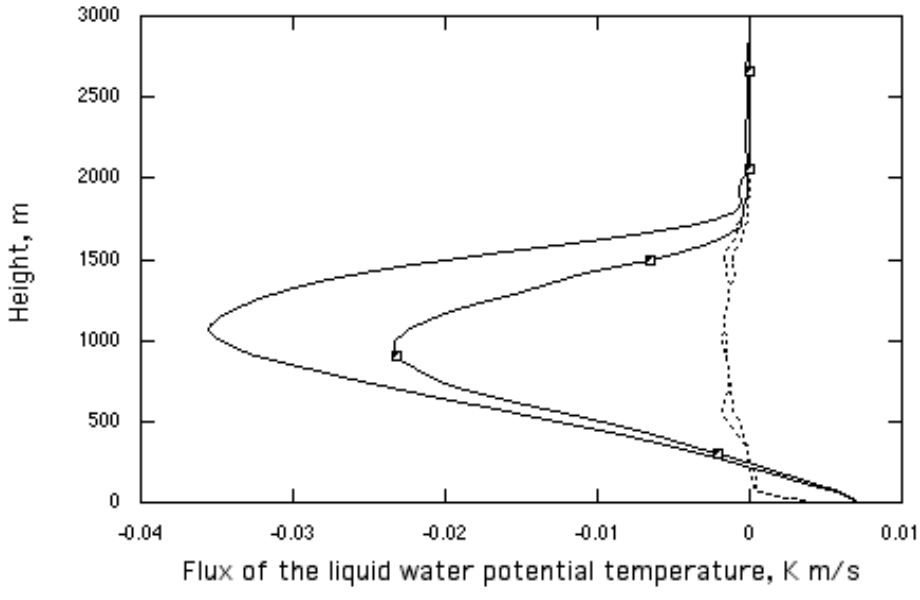

(b)

Figure 33. Vertical profiles of: (a) the buoyancy flux, and (b) the flux of the liquid water potential temperature, obtained from large-eddy simulations

of shearless and sheared (marked by squares) cumulus convection. Subgrid fluxes are indicated by dotted lines.

In order to understand this behavior, it is useful to inspect Equation (54), together with Figure 34 (which shows the total water specific humidity flux Q_T). Consequently, it can be concluded that in the cloud layer, the flux H_L is dominated by a negative flux Q_T. The total water specific humidity flux Q_T in Figure 34 is nearly constant with height in the mixed layer in run F. It slightly decreases with height in run S. This is due to the fact that the total water specific humidity is nearly constant in time. The total water specific humidity fluxes Q_T reach their peaks in the cloud layer, and decrease to zero at its top.

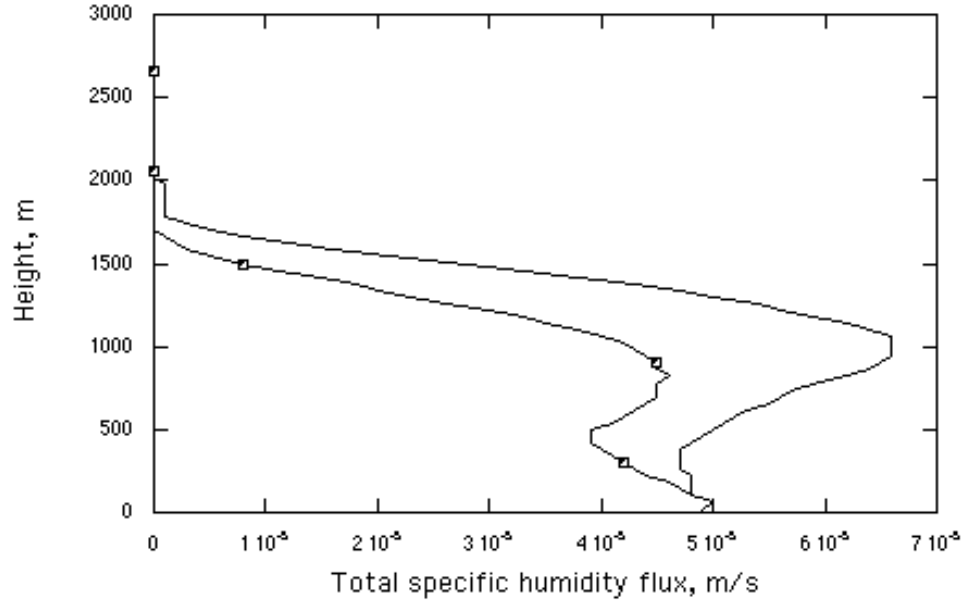

Figure 34. A vertical profile of the total water specific humidity flux obtained from large-eddy simulations of shearless and sheared (marked by squares) cumulus convection

Further analysis indicates that the temperature excesses Θ'_L in updrafts (not shown) are positive in the lower half of the subcloud mixed layer, and negative above. In downdrafts, the temperature excesses Θ'_L are negative in the lower half of the subcloud mixed layer, and positive above. As a result, the flux of the liquid water potential temperature in Figure 33b is negative above 250 m level.

The vertical velocities in updrafts are positive and relatively larger, while the vertical velocities in downdrafts are negative and relatively smaller. Consequently, the area covered by updrafts must be smaller than the area covered by downdraft. The resulting vertical velocity skewness (not shown) is positive. It increases from zero at the earth's surface to about 2.5-3 in the cloud layer, and decreases to zero above it.

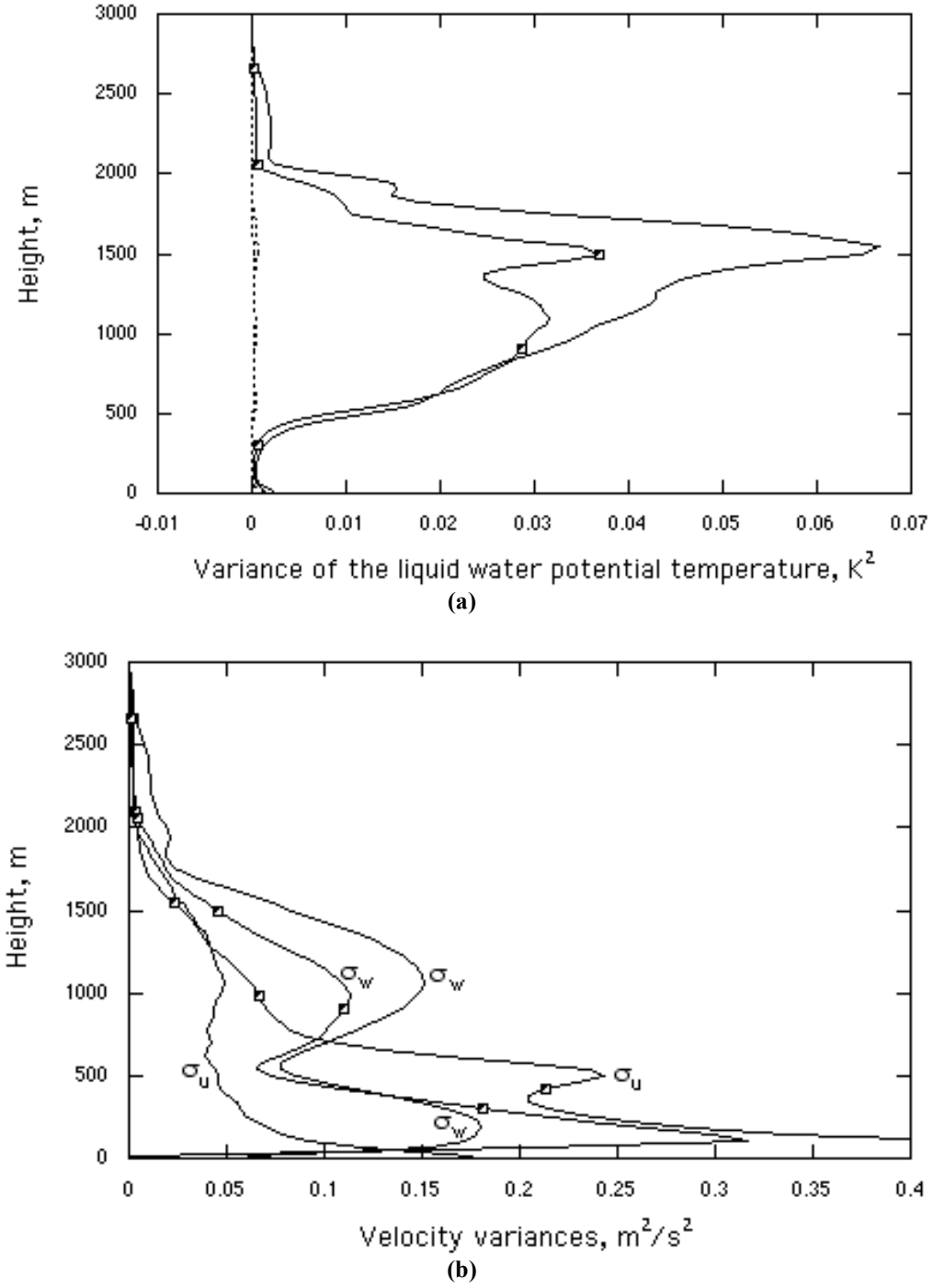

Figure 35. Vertical profiles of: (a) the variance of the liquid water potential temperature, (the subgrid contributions are marked by dotted lines), and (b) the wind velocity variances, obtained from large-eddy simulations of shearless and sheared (marked by squares) cumulus convection.

Variances of the liquid water potential temperature $\sigma_{\theta L}^2$ and the wind velocity components σ_u^2, σ_v^2, σ_w^2 are presented in Figure 35. The figure indicates a two-

layer structure of the cloud-topped ABL in both runs. In the subcloud mixed layer, the temperature and velocity variances are very similar to their counterparts in the cloud-free convective mixed layer, described in Section 3.1. The temperature variance sharply increases with height at the top of the 500-m mixed layer. It continues increasing above the mixed layer, and has a peak near the top of the cloud layer. The vertical velocity σ_w^2 has one peak in the mixed layer (like in the cloud-free case), and a second peak in the cloud layer.

4 Final Remarks

The test large-eddy simulations, presented in this Chapter, were performed for the sake of demonstration of the LES technique, using some arbitrarily governing parameters. For this reason they have not been compared with available atmospheric observations. Comparison of LES with atmospheric data constitutes an independent subject, which is out of the scope of this Chapter. To obtain more information on this issue, the reader is referred to the following sources: Schumann and Moeng (1991), Nieuwstadt et al (1992), Cuijpers and Duynkerke (1993), Shen and Moeng (1993), Khairoutdinov and Kogan (1999), Kosovic and Curry (1999), and Neggers et al. (2002).

As demonstrated above, the main benefit of using the LES approach is in its ability to generate various flow regimes, test theories, evaluate, refine, and develop parameterizations of the ABL. Within LES it is quite easy to isolate a particular physical process of interest to study its structure, dynamics, and impact on the ABL. Large-eddy simulations allow to visualize the 3D spatial and temporal evolution of turbulence. All these advantages have led to several important breakthroughs, which have changed views on the ABL turbulence and diffusion. In this respect, one could mention about the development of convective scaling, discovery of the mixed-layer entrainment processes, analysis of cloud-topped convection, and understanding of convective diffusion.

Inter-comparisons initiated in the early 1990s, have provided confidence that LES is generally a useful source of information on the ABL. Such inter-comparisons included cellular, shearless convection [Nieuwstadt et al. (1992)], stratocumulus convection based on FIRE case of July 7, 1987 [Moeng, et al., 1996, Bechtold et al., 1996], smoke-topped convection [Bretherton et al, 1999], the drizzling stratocumulus convection, based on ASTEX (Lagrangian-1) case [Duynkerke (1997)], cumulus sheared convection, based on ATEX data [Stevens et al., (2001), and on BOMEX data [Siebesma et al (2003)], the cumulus diurnal transition [Brown et al, 2002, ARM data], and a stable boundary layer [Beare et al, 2004].

In spite of increasing reliance on LES as a research tool, there is still considerable uncertainty concerning the fidelity of large-eddy simulations. Several LES studies have shown substantial variations in predictions of some important statistics. For example, in the smoke cloud case, entrainment rates differed by up to a factor of

two (Bretherton, et al. 1999). In simulations of trade-wind cumuli, the stratiform cloud fraction and the variance of total-water mixing ration were found to be highly sensitive to the choice of numerics, resolution, and subgrid parameterization (Stevens et al., 2001).

The present Chapter was focused on atmospheric turbulence, and omitted a discussion of diffusion simulations. Readers interested in this specific topic are referred to the papers of: Nieuwstadt and de Valk (1987), Haren and Nieuwstadt (1989), Schumann (1989), Mason (1992b), Sykes and Henn (1992), Nieuwstadt and Meeder (1997), Weil et al (1997), and Nieuwstadt (1998).

Acknowledgements

Some of the results presented in this Chapter were obtained during research supported by the National Science Foundation, grant no. ATM-0400590.

References

Acevedo, O. and D.R. Fitzjarrald, 1999. Observational and numerical study of turbulence during early evening transition. 13th Symposium on Boundary Layers and Turbulence, 10-15 January, 1999, Dallas, Texas.

Acevedo, O. and D.R. Fitzjarrald, 2001. The early evening surface-layer transition: temporal and spatial variability. *J. Atmos. Sci.,* 58: 2650-2667.

Agee, E.M., 1987. Mesoscale cellular convection over the oceans. *Dyn. Atmosp. and Oceans.,* 10: 317-341.

Albrecht, B.A., C.S. Bretherton, D. Johnson, W. H. Scubert, and S. Frish, 1995. The Atlantic stratocumulus transition experiment, ASTEX, *Bull. Amer. Meteorol. Soc.,* 76, 6: 889-904.

Albrecht, B.A., D.A. Randal, S. Nichols, 1988. Observations of marine stratocumulus clouds during FIRE, *Bull. Amer. Meteorol. Soc.*, 69, 6: 618 - 626.

Andren, A., 1996. The structure of stably stratified atmospheric boundary layers: a large-eddy simulation study. *Q. J. Roy. Met. Soc.*, 121: 961- 985.

Andren, A., A .Brown, J. Graf, P. J. Mason, C-H. Moeng, F. T. M. Nieuwstadt, and U. Schumann, 1994. Large-eddy simulation of a neutrally-stratified boundary layer: a comparison of four computer codes. *Q.J.R. Meteorol. Soc*, 120: 1457-1484.

Augstein, E., H. Riehl, F. Ostapoff, V. Wagner, 1973. Mass and energy transport in an undisturbed Atlantic trade-wind flow. *Mon. Weath. Rev*., 101, 2: 101-111.

Ball, F.K., 1960. Control of the inversion height by surface heating. *Quart. J. Roy. Meteor. Soc*., 86: 483-494.

Bardina, J., J. H. Ferziger, W. C. Reynolds, 1980. Improved subgrid scale models for large eddy simulations. *AIAA Paper* 80-1357.

Beare, R. J., and 16 co-authors, 2004. An intercomparison of large-eddy simulations of the stable boundary layer. Submitted to *Boundary-Layer Meteorology*.

Beare, R. J., and M.K.Macvean, 2004. Resolution sensitivity and scaling of large-eddy simulations of the stable boundary layer. *Boundary-Layer Meteorology, 112, 257-281*.

Bechtold, P., S. K. Krueger, W. S. Lewellen, E. van Meijgaard, C. H. Moeng, D. A. Randall, A. van Ulden, and S. Wang., 1996. Modeling a Stratucumulus-topped PBL: Intercomparison among different one-dimensional codes and with large eddy simulation. *Bull. Amer. Meteorol. Soc.,* 77. 9: 2033-2042.

Beets, C and B. Koren 1996. Large-eddy simulation with accurate implicit subgrid-scale diffusion. Dept. of Numerical Matematics Rep. NM-R9601. Stichting Mathematisch Centrum, Utrecht, Netherlands, 24 pp.

Betts, A.K., 1973. Non-precipitating cumulus convection and its parameterization. *Quart. J. Roy. Meteor. Soc.*, 99: 178-196.

Bretherton, C. S., M. K. MacVean, P. Bechtold, A. Chlond, W.R. Cotton, J. Cuxart, H. Cuijpers, M. Khairoutdinov, B. Kosovic, D. Lewellen, C.H. Moeng, B. Stevens, R. I. Sykes, and M. C. Wyant, 1999. An intercomparison of radiatively-driven entrainment and turbulence in a smoke cloud, as simulated by different numerical models. *Q. J. R. Meteor.Soc*.125: 391-423.

Brost R. A. and J. C. Wyngaard, 1984a. Marine stratocumulus layers: Part I. *J. Atmos. Sci*., 39: 800-817.

Brost R. A. and J. C. Wyngaard, 1984b. Marine stratocumulus layers: Part II. *J. Atmos. Sci*., 39: 818-836.

Brown, A., S.H. Derbyshire, and P.J. Mason, 1994. Large-eddy simulation of the stable atmospheric boundary layers with a revised stochastic subgrid model. *Q.J. Roy. Met. Soc.*, 120: 1485-1512.

Brown, A., R. T. Cederwall, A. Chlond, P. G. Duynkerke, J. C. Golaz, M. Khairoutdinov, D. C. Lewellen, A. P. Lock, M. K. McVean, C.-H. Moeng, R. A. Neggers, A. P. Siebesma, and B. Stevens, 2002. Large-eddy simulation of diurnal cycle of shallow convection over land. *Q.J.R. Meteorol. Soc,* 128: 1075-1093.

Brümmer, B. S., S. Bakan, and H. Hinzpeter, 1985. KONTUR: Observations of clouds streets and open cellular structures. *Dyn. Atmos. Oceans*, 9: 281-294.

Cedeval, R. and R. L. Street, 1999. Turbulence modification in the evolving stable boundary layer: a large eddy simulation. *13th Symp. on Boundary Layers and Turbulence*, Dallas Texas, AMS January, 1999.

Chlond A. and G. Muller , 1997. Very large-eddy modelling of convective structures during cold-air outbreaks. *Colloquium on Clear and Cloudy boundary Layers*, Amsterdam, 26-29 August, 1997.

Cuijpers J. W. M., and P. G. Duynkerke, 1993. Large-eddy simulation of trade wind cumulus clouds. *J. Atmos. Sci.*, 50: 3894-3908.

Curry, J. A., P. Hobbs, M. King, D. Randall, P. Minnis, et al., 2000. FIRE Arctic Cloud Experiment. *Bull. Amer. Meteorol. Soc*., 81: 5 -29.

Deardorff, J. W., 1970. Preliminary results from numerical integration of the unstable planetary boundary layers. *J. Atmos. Sci.,* 27: 1209-1211.

Deardorff, J. W., 1972. Numerical integration of neutral and unstable planetary boundary layers. J. Atmos. Sci., 29: 91-115.

Deardorff, J. W., 1973. Three-dimensional numerical modeling of the planetary boundary layers. In *Workshop on Micrometeorology*, D. A. Haugen, Ed., Amer. Meteor. Soc., 271-311.

Deardorff, J. W., 1974a. Three-dimensional numerical study of the height and mean structure of a heated planetary boundary layer. *Bound.-Layer Meteor*., 7: 81-106.

Deardorff, J. W., 1974b. Three-dimensional numerical study of turbulence in an entraining mixed layer. *Bound.-Layer Meteor*., 7: 199-226.

Deardorff, J. W., 1976. On the entrainment rate of a stratocumulus-topped mixed layer. *Quart. J. Roy. Meteor Soc*., 102: 563-582.

Deardorff, J. W., 1980. Stratus-capped mixed layers derived from a three-dimensional model. *Bound.- Layer Meteor*., 18: 495-527.

Duynkerke, P. G., P. J. Jonker, A. Chlond, M. C. Van Zanten, J. Cuxart, P. Clark, E. Sanchez, G. Martin, G. Lenderink, J. Teixeira, 1997. Intercomparison of three- and one-dimensional model simulations and aircraft observations of stratocumulus. *Bound. Layer Meteorol*., 92: 453-487.

Galmarini, S, C. Beeds, P. G. Duynkerke, and J. V.-G. de Arellano, 1998. Stable nocturnal boundary layers: a comparison of one-dimensional and large-eddy simulation models. *Bound. Layer Meteorol*., 88: 181-210.

Germano, M. U., Piomell, P. Moin, 1992. A dynamic subgrid-scale eddy diffusivity model. *Phys. Fluids* A3 (7): 1760-1765.

Glendening, J. W., 1996. Linear eddy features under strong shear conditions. *J. Atmos. Sci*., 53: 3430-3449.

Haren, L. van and F. T. M. Nieuwstadt, 1989. The behaviour of passive and buoyant plumes in a convective boundary layer, as simulated with large-eddy simulation model. *J. Applied Meteor.,* 28: 818-832.

Henn D. S. and R. I. Sykes 1992. Large-eddy simulation of dispersion in the convective boundary layer. *Atmos. Envir,* 26A: 3145-3159.

Holland J. Z. and E. M., Rasmusson, 1973. Measurements of the atmospheric mass, energy, and momentum budgets over 500-kilometer square of tropical ocean. *Month. Weath. Rev*.,101,1: 44-55.

Jian, H. and W. R. Cotton, 2000. Large-eddy simulation of shallow cumulus convection during BOMEX: sensitivity to microphysics and radiation. *J. Atmos. Sci*., 57: 582-594.

Mason P. J. and D. J. Thompson, 1987. Large-eddy simulation of the neutral-static-stability planetary boundary layer. Q.J.R. Meteorol. Soc, 113: 413-443.

Mason P. J. and S.H. Derbyshire, 1990. Large-eddy simulation of the stably-stratified atmospheric boundary layer. *Bound.-Layer Meteor*. 53: 117-162.

Mayor, S. D., P. R. Spalart, G. J. Tripoli, 2002. Application of a perturbation recycling method in the large-eddy simulation of a mesoscale convective internal boundary layer. *J. Atmos. Sci.*, 59: 2385-2395.

Khairoutdinov, M. and J. Kogan, 1999. A large eddy simulation model with explicit microphysics: validation against aircraft observations of a stratocumulus-topped boundary layer. *J. Atmos. Sci.,* 56: 2115-2131.

Kim, S.-W., S.-U. Park, and C.-H. Moeng, 2003. Entrainment processes in the convective boundary layer with varying wind shear. *Bound.-layer. Meteor*, 108: 221-245.

Kogan, Y. L., M. P. Khairoudtdinov, D. K. Lilly, Z. N. Kogan, Q. Liu, 1995. Modeling of stratocumulus cloud layers in a large eddy simulation model with explicit microphysics. *J. Atmos. Sci,* 52: 2923-2940.

Kosovic, B and J. Curry, 1999. Large-eddy simulation of a quasi-steady stably-stratified atmospheric boundary layer. *13th Symp. on Boundary Layers and Turbulence*. Dallas, Texas, AMS.

Kristovich**,** D., G. Yang, J. Verline, P. J. Sousonis, P. Mourad, D. Lenschow, R. M. Rauber, M. K. Ramamurthy, B. F. Jewett, K. Beard, E. Cutrim, P. J. DeMott, E. W. Eloranta, M. R. Hjemfeld, S M. Kreidenweis, J. Martin, J. Moore, H. T. Ochs, D. C. Rogers, J. Scala, G. Tripoli, J. Young., 2000. The lake-induced convection experiment and the snowband dynamics project. *Bull. Amer. Meteorol. Soc.*, 127: 519-542.

LeMone, M. A. and R. L., Grossman, 1999. Evolution of potential temperature and moisture during the morning: CASES-97. *13th Symp. on Boundary Layers and Turbulence*, Dallas Texas, January, 1999, AMS.

LeMone, M. A. R, Grossman, R. T. McMillen, K. Liou, S. C. Ou, S. McKeen, W. Angevine, K. Ikeda, and F. Chen: Cases-97, 2002. Late-morning warming and moistening of the convective boundary layer over Walnut River watershed. *Bound.-layer. Meteor*, 104: 1-52.

Leonard, A, 1974. On energy cascade in large eddy simulations of turbulent fluid flows. *Adv. in Geophysics*, 18A: 237-248.

Lewellen, D. C., and W. S. Lewellen, 1996. Influence of Bowen ratio on boundary layer cloud structure. *J. Atmos. Sci.*, 53: 175-187.

Lilly, D. K., 1967. The representation of small-scale turbulence in numerical simulation experiments. In: *Proc. IBM Sci. Comp. Symp. on Envir. Sci*. Nov., 14-16, 1966. T. J. Watson Res. Center. Yorktown Hills, N.Y., IBM Form 320-1951, pp 195-210.

Lilly, D. K., 1968. Models of Cloud-Topped Mixed Layers under Strong Inversion. *Quart. J. Roy. Meteor. Soc.,* 94: 292-309.

Lilly, D.K., 1992. A proposed modification of the Germano subgrid-scale closure method. Phys. Fluids A. 633-635.

Mason, P. J., and D. J. Thompson, 1987. Large-eddy simulations of the neutral-static-stability planetary boundary layer. *Quarterly J. Royal Meteorology Society*. Vol. 113, p. 413-444.

Mason, P. J., 1989. Large-eddy simulation of the convective atmospheric boundary layer. *J. Atmos. Sci.,* 46: 1492-1516.

Mason P. J., and S. H. Derbyshire, 1990. Large-eddy simulation of the stably-stratified atmospheric boundary layer. *Boundary-Layer Meteorology*, 53: 17-162.

Mason, P.J., 1992a. Large-eddy simulation of dispersion in convective boundary layer with wind shear“. *Atmospheric Environment*, **26**, 9, 151-1571.

Mason P. J., 1992b. Large-eddy simulation of dispersion from an elevated point source in the convective boundary layer. *Atmos. Envir.,* 26A: 1561-1572.

Mason, P. J., 1994. Large-eddy simulation: A critical review of the technique. *Quart. J. Roy. Meteor. Soc.*, 120, 1-26.

Moeng, C.-H. 1984. A large-eddy simulation for the study of planetary boundary layer turbulence. *J. Atmos. Sci.* 41: 2052-2062.

Moeng, C.-H., 1986. Large-eddy simulation of a stratus-topped boundary Part I: Structure and budgets. *J. Atmos. Sci*., 43: 2886-2900.

Moeng C.-H. and U. Schumann, 1991. Composite structure of plumes in stratus-topped boundary layers. *J. Atmos. Sci.*, 48: 2280-2291.

Moeng, C. H. and P. P. Sullivan, 1994. 'A Comparison of Shear and Buoyancy Driven Planetary Boundary Layer Flows'. *J. Atmos. Sci.,* 51: 999-1022.

Moeng, C.-H., W. R. Cotton, C. Bretherton, A. Chlond, M. Khairoutidinov, S. Krueger, W. S. Lewellen, M. K. MacVean, J. R. M. Pasquier, H. A. Rand, A. P. Siebesma, B. Sievers, and R. I. Sykes, 1996. Simulation of a stratocumulus-topped planetary boundary layer: Intercomparison among Different numerical codes. *Bull. Amer. Meteor. Soc*., **77**: 261-278.

Moeng, C.-H., 2000. Entrainment rate, cloud fraction, and liquid water path of PBL stratocumulus clouds. *J. Atmos. Sci.*, 57: 3627-3643.

Neggers, R. A., P. G. Dunkerke, and S. M. Rodts, 2002. Shallow cumulus convection: a validation of large-eddy simulation against aircraft and Landsat observations. *15th Symp. on Boundary Layers and Turbulence*. July, Wageningen, The Netherlands, AMS.

Nichols, S.,1989. The structure of radiatively driven convection in stratocumulus. *Quart. J. Roy. Met. Soc*., 115: 487-511.

Nieuwstadt, F. T. M, 1984. The turbulent structure of the stable, nocturnal boundary layer. *J. Atmos. Sci.*, 44: 2202-2216.

Nieuwstadt, F. T. M. and R. A. Brost, 1986. The decay of convective turbulence. *J. Atmos. Sci.,* 43: 532-546.

Nieuwstadt, F. T .M. and J. P. J. M. de Valk, 1989. A Large-eddy simulation and non-buoyant plume dispersion in the atmospheric boundary layer. *Atmos. Env*., 21, 12: 2573-2587.

Nieuwstadt, F. T. M., 1990. Direct and large-eddy simulation of free convection. *Proc. 9th Interna. Heat Transfer Conference*, Jerusalem 19-24 August 1990. Amer. Soc. Mech. Eng., Vol 1: 37-47.

Nieuwstadt, F. T. M., P. J. Mason, C. H. Moeng, and U. Schumann, 1992. Large-eddy simulation of convective boundary-layer: A comparison of four computer codes. *Turbulent Shear Flows 8*, (Durst H. et al., Eds), Springer-Verlag, 343-367.

Nieuwstadt, F. T. M. and J.P. Meeder, 1997: Large-eddy simulation of air pollution dispersion: a review. *New Tools in Turbulence Modeling. Les Houches School*, May 21-31 1996, (Eds.: O. Metais and J.O. Ferziger), Springler-Berlin, 265-279.

Nieuwstadt, F. T. M., 1998. Review of Diffusion processes in the convective boundary layer. In: *Buoyant convection in Geophysical flows*, E.J. Plae (ed.): 371-399.

Paulos, G. S., W. Blumen, D. C. Fritts, J. K. Lundquist, J. Sun, S. P. Burns, C. Nappo, R. Banta, R. Newsome, J. Cuxart, E. Terradwllas, B. Basley, and M. Jensen, 2002. Cases-99: A comprehensive investigation of the stable nocturnal boundary layer, *Bull. Amer. Meteorol. Soc.*,, April, 576-581.

Ricchazzi, P, S. Yang, C. Gautier, and D. Sowle, 1998. A research and teaching software tool for plane-parallel radiative transfer in the earth's atmosphere. *Bull. Amer. Meteorol. Soc.,*, 79, 10: 2101-2114.

Saiki, E. M., C. H. Moeng and P. P. Sullivan, 1999. Large-eddy simulation of the stably stratified planetary boundary layer. *13th Symp. on Boundary Layers and Turbulence*. Dallas, Texas, AMS.

Schemm, C. E., and F. B. Lipps, 1976. Some results from a simplified three-dimensional numerical model of atmospheric turbulence. *J. Atmos. Sci.*, 33: 1021-1041.

Shen, S. and C.-H. Moeng, 1993. Comparison of a computer-simulated stratus-topped boundary layer with aircraft observations. *Bound.-layer. Meteor*, 65: 29-53.

Schmidt, H. and Schumann, U. 1989. Coherent structures of the convective boundary layer derived from large-eddy simulations. *J. Fluid Mech*. 200: 511-562.

Schröter, M. and S. Raasch, 2002. Broadening of convective cells during cold air outbreaks: a high resolution study using a parallelized LES model. *15th Symp. on Boundary Layers and Turbulence*. July, Wageningen, The Netherlands, AMS.

Schumann, U, 1989. Large-eddy simulation of turbulent diffusion with chemical reactions in the convective boundary layer. *Atmos. Envir*. 23: 1713-1727.

Schumann, U. and Moeng C.-H. 1991. Plume fluxes in clear and cloudy convective boundary layers. *J. Atmos. Sci.* 48: 2280-2291.

Siebesma, A. P., C. Bretherton, A. Brown , A. Chlond, J. Cuxart, P. Duynkerke, H. Jiang, M. Khairoutdinov, D. Lewellen, C. H. Moeng, E. Sanchez, B. Stevens, D. E. Stevens, 2003. A large-eddy simulation intercomparison study of shallow cumulus convection. *J. Atmos. Sci*. J. Atmos. Sci, 60: 1201-1219.

Sommeria, G., 1976. Three-dimensional simulation of turbulent processes in an undisturbed trade wind boundary layer. *J. Atmos. Sci.*, 33: 216-241.

Sommeria, G., and J. W. Deardorff, 1977. subgrid-scale condensation in models of nonprecipitating clouds. *J. Atmos. Sci.*, 34: 344-355.

Sorbjan, Z., 1986. On similarity in the atmospheric boundary layer. *Bound.-Layer Meteor*., 34: 377-397.

Sorbjan, Z, 1989. *Structure of the atmospheric boundary layer*. Prentice Hall, 316 pp.

Sorbjan, Z, 1991. Evaluation of local similarity functions in the convective boundary layer. *J. Appl. Meteor*., 30: 1565-1583.

Sorbjan, Z.**,** 1995. Toward evaluation of heat fluxes in the convective boundary layer. *J. Appl. Meteor*., 34: 1092-1098

Sorbjan, Z., 1996a. Numerical study of penetrative and "solid-lid" non-penetrative convective boundary layers. *J. Atmos. Sci.*, 53: 101-112.

Sorbjan, Z., 1996b. Effects caused by varying strength of the capping inversion based on a large-eddy simulation of the shear-free convective boundary layer. *J. Atmos. Sci.*, 53: 2015-2024.

Sorbjan, Z., 1997. Decay of convective turbulence revisited. *Bound.-Layer Meteor*., 82: 501-515.

Sorbjan, Z. and M. Uliasz, 1999. Large-eddy simulation of atmospheric dispersion in the nocturnal cloud-topped atmospheric boundary layer. *13th Symp. on Boundary Layers and Turbulence*, Dallas Texas, January, 1999.

Sorbjan Z., 2001. An evaluation of local similarity on the top of the mixed layer based on large-eddy simulations. *Boundary-Layer Meteorology*, 101: 183-207.

Sorbjan Z., 2004a. Large-eddy simulation of the baroclinic boundary layer. *Boundary-Layer Meteorology*, 112: 57-80.

Sorbjan Z., 2004b. Statistics of scalar fields in the atmospheric boundary layer based on large-eddy simulations. Part 1: Free convection. Accepted to *Boundary-Layer Meteorology*.

Sorbjan Z., 2004c. Statistics of scalar fields in the atmospheric boundary layer based on large-eddy simulations. Part 2: Forced convection. Submitted to *Boundary-Layer Meteorology*.

Stevens, B., W. Cotton, G. Feingold, C, and H. Moeng, 1998. Large eddy simulations of strongly precipitating, shallow, stratocumulus-topped boundary layers. *J. Atmos. Sci.*, 55: 3616-3638.

Stevens, B., C. H. Moeng, and P. P. Sullivan, 1999. Large-eddy simulations of radiatively driven convection: sensitivities to the representation of small scales. *J. Atmos. Sci.*, 56: 3963-3984.

Stevens, B. A. S. Ackerman, B. A. Albrecht, A. R. Brown, A. Chlond, J. Cuxart, P. G. Duynkerke, D. C. Lewellen, M. K. MacVean, R. A. Neggers, E. Sanchez, A. P. Siebesma, and D. E. Stevens, 2001. Simulation of trade wind cumuli under a strong inversion. *J. Atmos. Sci.,* 58: 1870-1891.

Sykes R. I., and D.S. Henn, 1988. A large-eddy simulation of turbulent sheared convection. *J. Atmos. Env.,* 26A: 3145-3159.

Sykes R. I., and D.S. Henn, 1992. A large-eddy simulation of dispersion in the convective boundary layer. *J. Atmos. Sci.,* 46: 1106-1118.

Toon, O. B., C. P. McKay, T. P. Ackerman, and K. Santhanam, 1989. Rapid calculations of radiative heating rates and photodissociation rates in inhomogeneous multiple-scattering atmospheres. *J. Geophys. Res. Atmos.,* 94, (D13): 16287-16301.

Webster P. J., and R. Lucas, 1992. Toga COARE: the coupled ocean-atmosphere response experiment. *Bull. Amer. Meteorol. Soc.,*, 73, 9: 1377-1416.

Weil, J. C., P. P Sullivan and C.-H. Moeng, 1997. Lagrangian modeling of dispersion in the convective boundary layer using LES velocity fields. Preprint Vol. *12 Symp. on Boundary layers and Turbulence*, Vancouver, Canada, 108-109.

White, A. B., R. J. Zamora, K. J. Olszyna, C. A. Russell, B. D. Templeman, J. W. Bao, 2000. Observations and numerical study of the morning transition: a case study from SOS-99. *13th Symp. on Boundary Layers and Turbulence*. Dallas, Texas, AMS.

Willis, G. E. and J. W. Deardorff, 1976. A laboratory study of dispersion from an elevated source in a convective mixed layer. *Atmos. Environ*., 12: 1305-1313.

Willis, G. E. and J. W. Deardorff, 1978. A laboratory study of diffusion into a convective planetary boundary layer. *Quart. J. R. Meteorol. Soc*., 105: 109-117.

Willis, G. E. and J. W. Deardorff, 1981. A laboratory study of dispersion from a source in the middle of the convective mixed layer. *Atmos. Environ.*, 12: 1305-1313.

Wyngaard, J. C., and R. A. Brost, 1984. Top-down and bottom-up diffusion of a scalar in the convective boundary layer. *J. Atmos. Sci.,* 41: 102-112.